DESIGN AND IMPLEMENTATION OF A FLUID-MECHANICAL DYNAMIC
AFTERLOAD FOR USE IN AN ISOLATED HEART APPARATUS

Randal T. Cole

A dissertation submitted to the faculty of the University of North Carolina at Chapel Hill in partial fulfillment of the requirements for the degree of Doctor of Philosophy in the Department of Biomedical Engineering.

Chapel Hill
2006

Approved by
Advisor: Carol L. Lucas
Advisor: Timothy A. Johnson
Reader: Wayne E. Cascio
Reader: Richard L. Goldberg
Reader: Stephen R. Quint

ABSTRACT

RANDAL T. COLE: Design and Implementation of a Fluid-Mechanical Dynamic Afterload
for Use in an Isolated Heart Apparatus
(Under the direction of Carol L. Lucas and Timothy A. Johnson)

An isolated heart attached to a fluid-mechanical impedance (afterload) provides a method

for study of myocardial processes and pressure and flow mechanics within the heart.

Afterloads currently available allow various impedance parameter settings, but they are not

automatically or dynamically controlled. A dynamically controlled afterload was constructed

and its suitability tested for implementation with an isolated heart apparatus.

Initial work was in development of a cardiovascular model to reveal trends for aortic

pressure changes with afterload parameter adjustments. The LabVIEW^{TM} model enables

simulations with open-loop windkessel-type impedances and simulations with a closed-loop

circulatory model. Cataloged trends were used to guide the dynamic afterload controls, and

the open-loop impedances provided methods for modeling the fluid-mechanical system.

Following this work, a systems analysis tool was developed in LabVIEW^{TM} and Matlab®

to enable characterization of the fluid-mechanical afterload. The program contains time-

domain and spectral analyses that incorporate equal variance algorithms for the correlation

analyses and averaging methods for noise reduction in the spectral analyses for stationary

signals. Auto- and cross-spectral analyses were used to generate system impedance spectra

from dynamic afterload simulations.

The culmination of this project was construction of a fluid-mechanical dynamic afterload.

The dynamic nature of the afterload involves controlled, automatic adjustment of mechanical

resistance, compliance and volume elements. These adjustments in afterload cause input

pulsatile pressure to match the mean and range of a reference pressure. Simulations were

performed with a pulsatile pressure pump for ten reference pressures with physiologically

realistic mean and range values. The dynamic afterload constrained input pressures to within

$\pm$ 5% of the reference values and typically settled to the targeted values in 45 – 50 cycles.

Impedance spectra from the simulations provided consistent and physiologically realistic

estimates of afterload parameters fitted to a four-element windkessel-type impedance.

Effects of changing impedance on the mean, range and stroke volume followed anticipated

trends. These tests demonstrate that the dynamic afterload exhibits the qualities necessary

for implementation with an isolated heart apparatus. Furthermore, this system will enable

studies both of transient behavior in the isolated heart with changing afterload and of

controlled pressure characteristics from a changing input pressure source.

ACKNOWLEDGEMENTS

To properly acknowledge those who have helped me along the way in my academic career I must start with those I love the most, my wife Jennifer and our children Anthony and Alina. They have been a major source of inspiration for the time and effort expended in reaching this goal. Though I have had to work many long nights and spend much time in study, I hope they understand that this work is dedicated to them.

To my extended family I must also say "thank you." Without their support, both in time and finances, I could never have made it. Their love did not go unnoticed and it will not go unrewarded.

Dr. Tim Johnson has been an invaluable mentor and friend through the course of my research. Without his guidance and encouragement, this project would never have been finished. He has seen me through good years and bad years, and he has always been patient and understanding. For this I am very grateful.

The hospitality and friendliness of Dr. Carol Lucas was a large part of what drew me to the University of North Carolina – Chapel Hill. Her willingness to contribute to my work and the kindness she has shown me constitute a wonderful part of my experiences at UNC.

In the latter stages of my graduate work, Dr. Stephen Quint provided much needed guidance on an academic and personal level. His friendship and willingness to participate in my academic career are much appreciated.

TABLE OF CONTENTS

Page

viii

LIST OF TABLES

LIST OF FIGURES

CHAPTER I

INTRODUCTION

Brief History of Cardiovascular Modeling and the Isolated Working Heart Model

In the second century AD, Galenos of Pergamon, being influenced by Erasistratos, proposed a blood transporting system in which the heart received at least part of the circulating blood. However, it was not until 1628 that William Harvey put forth the heart as the central pump of a closed circulatory system.[1,2] Nearly one hundred years later, Stephen Hales observed the fire engines of his day, which employed a chamber of air to cushion the bolus input of water and produce a steady outflow.[2] Hales likened this air cushion to the effect of the arterial system in producing steady flow at the tissue level from the pulsating heart pump. In addition, Hales pioneered the concept of peripheral resistance in tiny blood vessels.[3] Many years passed with Hales work going largely untapped; nevertheless, the middle to latter part of the nineteenth century saw an emergence of education for the middle class in Germany and other parts of Europe. An emphasis on research, teaching and patient care was prominent in Germany and many medical universities in the United States and Canada were later transformed according to this model.[4]

Groups of young and energetic scientists in Europe and America were working in numerous areas, including physiology, and a partial list of contemporaries provides insight into the significance of the advances that were soon to come. Among the scientists of that era were Adolf Fick, Otto Frank, Ernest Starling, Willem Einthoven, W. Conrad Röntgen,

and Louis Pasteur.[4] Cardiovascular research was a major area of interest, as the heart's function was still poorly understood. The ability to isolate and maintain a beating heart outside the body was an important first step to better understanding the heart's function. While working in Carl Ludwig's Leipzig Physiological Institute, Elias Cyon developed a method for isolating the frog heart. Future modifications of this model, made by Ludwig, enabled studies that showed such important phenomena as the absolute refractory period, the all-or-none-law and the atrial origin of cardiac automaticity.[5] The frog's heart was an ideal candidate for isolation due to its simple physiology (lack of coronary circulation and only a single ventricle) and its exchange of gases by diffusion. Additional steps would be needed to isolate a mammalian heart. Henry Newell Martin, who worked at Johns Hopkins, initiated this process in the 1880's with his heart-lung preparation of feline and canine hearts. This preparation maintained only the coronary circulation as the systemic load, but allowed independent alteration of preload and afterload for the left ventricle.[5] Oscar Langendorff, in 1895, introduced a version of this isolated heart setup by which he could perfuse the heart and keep it alive for several hours. Langendorff's system enabled more precise control over retrograde perfusion pressure and an enhanced kymograph for improved recording of ventricular shortening during contraction. Langendorff's ability to arrest and restart the heart gave him opportunity to elucidate the roles of vagus stimulation, temperature, electrical stimulation and the coronary circulation in regulating heart rate and viability.[5] His method for maintaining the isolated heart was to perfuse, in retrograde fashion, the coronary circulation that feeds the myocardium. This was accomplished by tying the aorta to a pressured tube containing the nutrient media. When the media is injected, the aortic valve closes, and the media has nowhere to go except through the coronary circulation.
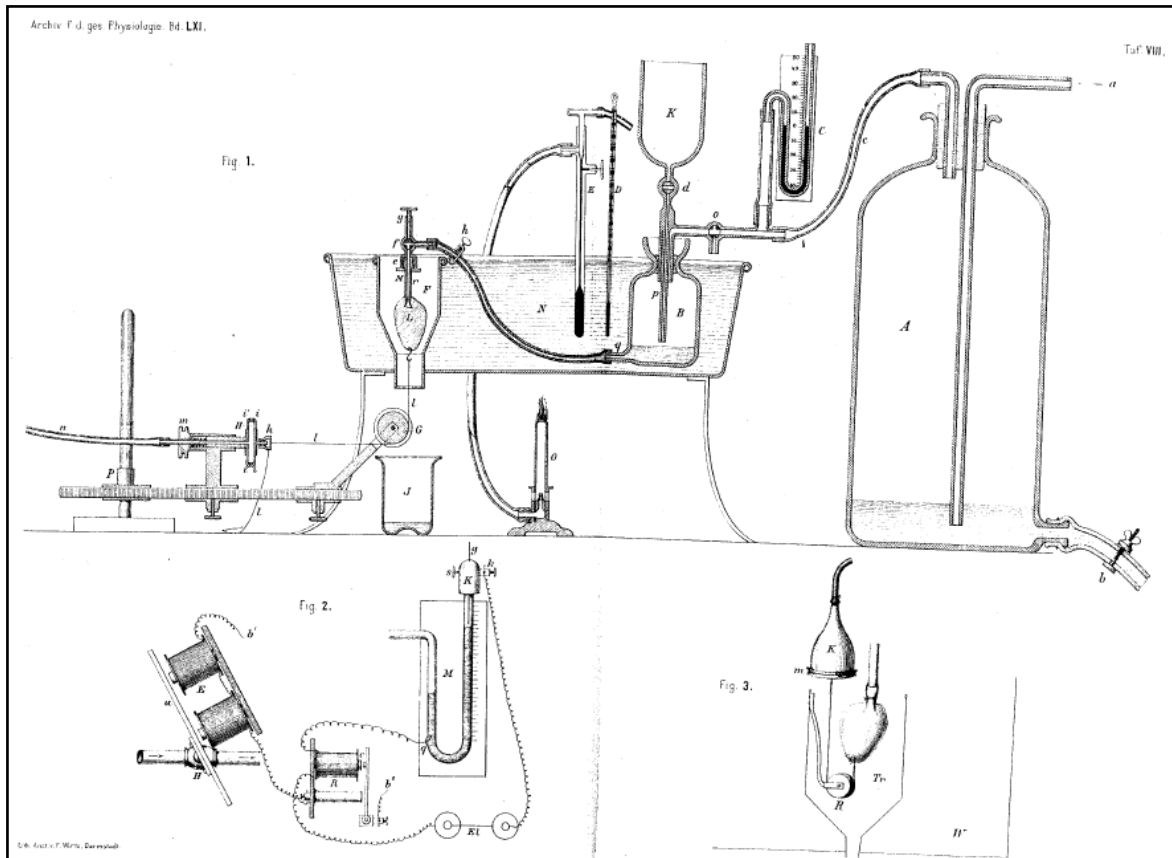
Figure 1.1 Langendorff's 1895 Isolated Heart Setup. From Langendorff.[6] With kind permission of Springer Science and Business Media.

Several of Langendorff's original observations are as follows: blood leaving the heart is deoxygenated and dark, coronary perfusion enables stable cyclic contractile functioning of the heart, vagus stimulation slows the heart, a decrease in temperature slows the heart, fibrillation can be caused by electrical stimulation, lack of coronary blood flow results in loss of myocardial contraction, subsequent restoration of coronary blood flow results in a return of cardiac contraction.[4] The isolated heart setup has numerous experimental advantages; however, it excludes several important factors, such as the effects of preload and afterload on the ability of the ventricle to contract (contractility), and a measure of the heart's ability to perform work. Other scientists would soon recognize the importance of these factors in cardiac function.

In the late nineteenth and early twentieth century, German physiologist Otto Frank expanded the neglected work of Stephen Hale. When Hale's writings were translated from English to German, the air cushion Hale used to describe the buffering within the fire engines became an air kettle or *windkessel*. Frank developed this buffering effect into the Windkessel theory.[2] In its simplest form, the Windkessel theory considers the impedance of the systemic circulation (afterload) against which the heart pumps to be comprised of a lumped compliance element (cushion of air) and a lumped resistance.[3] Frank's research with the isolated frog heart enabled him to recognize that the amount of ventricular filling and the downstream load against which the ventricle pumps both affect the contractility of the ventricle. Ernest Starling later expanded this view in a statement of the Frank-Starling law of the heart, which says, "within physiological limits, the larger the volume of the heart, the greater are the energy of its contraction and the amount of chemical change at each contraction." [1] The energy expended by the heart during each contraction is the work performed by the heart, and this heart work was further characterized in terms of stroke volume and cardiac output by Guyton and others in the mid twentieth century.[1]

Both the cardiovascular model based on the Windkessel theory and the isolated mammalian heart system were employed by scientists in the early and mid 1900's to greatly enhance the understanding of cardiovascular phenomena. During this time, Frank realized what later became a major criticism of the Windkessel theory of cardiac afterload, namely, its inability to rationally account for wave propagation and reflection.[2] In the 1950's and 60's, Taylor and McDonald modified the arterial model according to transmission line theory and demonstrated the ability to analyze the impedance of the afterload in the frequency domain. These models began to account for such phenomena as input frequency, fluid inertance,

variable viscosity, wave attenuation and reflection sites.[3] In a similar manner, researchers

also recognized the shortcomings of the isolated heart system. The understanding of

chemical and physiological influences on ventricular work elucidated the need for a working

heart model to perform certain types of studies. In a working heart setup, the blood, or

nutrient media is actually cycled through the atrium and ventricle, as opposed to the empty

ventricle of the Langendorff method. The heart performs work by ejecting the blood volume

against the afterload (opposing pressure) presented at the aortic valve. One of the earliest

references of a working heart model is from Schreiber *et al.*[7] as they studied the potassium

exchange mechanism in the heart. Schreiber understood that the ventricular load affected

this exchange mechanism; thus, a working version of the isolated heart was developed for

their study. Neely and Morgan *et al.*[8] were also constructing their own version of an isolated

working heart to study oxygen consumption. Their apparatus was simple but elegant (see

Figure 1.2), and modifications of this device are still employed today.
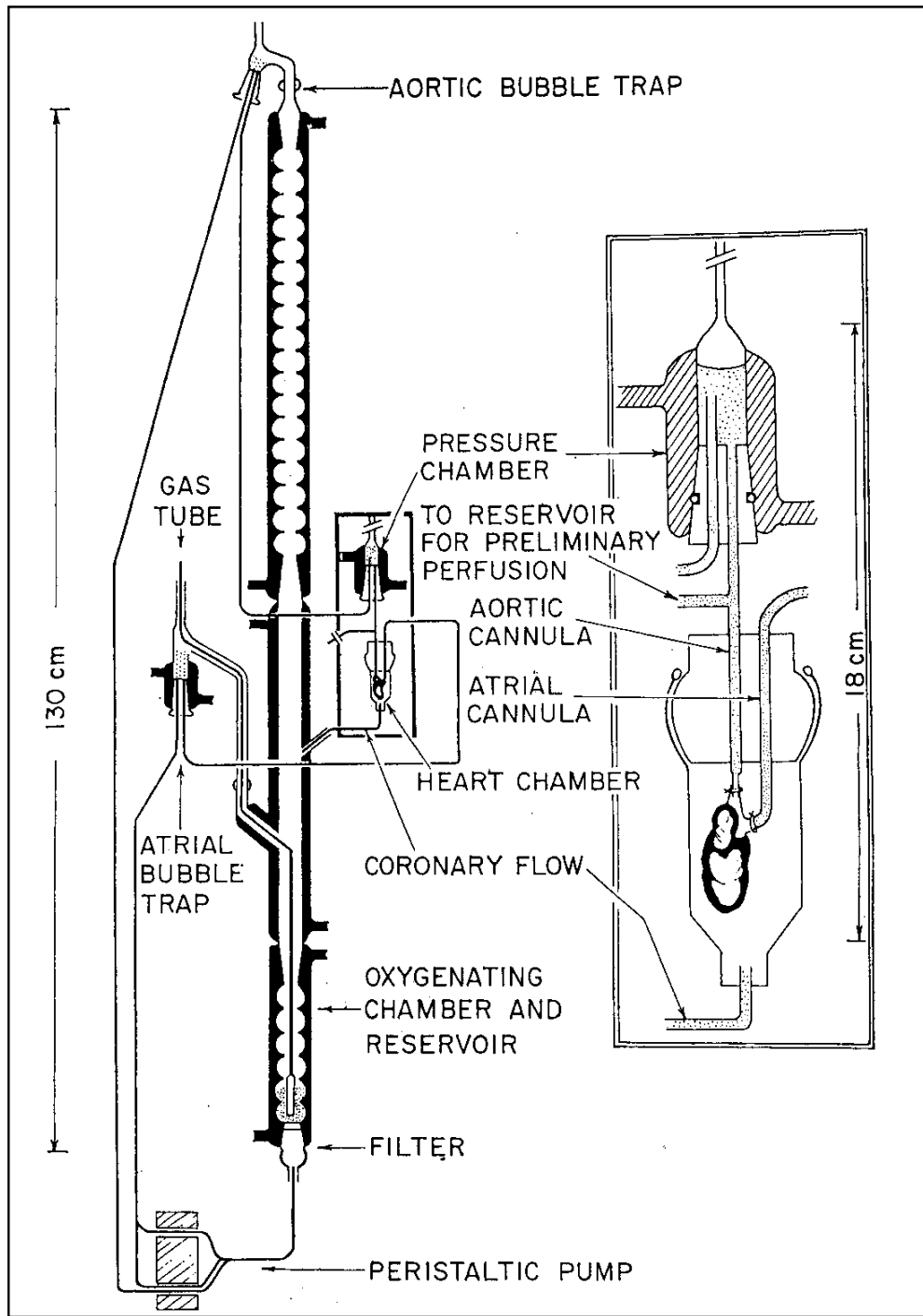
Figure 1.2 Isolated Working Heart Setup. From Neely and Morgan *et al.* [8] Used with permission from The American Physiological Society.

Several groups were making improvements on both the isolated heart system and the *in vitro* vascular models, and these advancements would continue at a faster pace over the next several decades.

With the advent of the analog computer in the 1960's, repetitive solutions to large sets of differential equations became feasible. This allowed scientists such as Noordergraaf and Rideout [9, 10] to model cardiovascular dynamics more completely. Frequency analysis of vascular impedance provided a method for testing additional afterload components in electrical and hydrodynamic models. Soon, these analog computer models led to mechanical afterloads (Westerhof *et al.*[11]) that enabled control of the main resistance and compliance elements. These mechanical loads, when coupled with a working heart, permitted manipulation of afterload in such a manner that realistic aortic pressure (AOP) and aortic flow (AOF) were produced. With continuing advancement in computer technology (integrated circuits and the digital computer) research groups such as Suga and Sagawa *et al*. [12-15] and Westerhof *et al.*[16] were able to expand control of the working heart and mechanical afterload system. The effects of afterload manipulations on the end-systolic pressure-volume relationship (ESPVR) of the ventricle and AOP/AOF were interrogated. Furthermore, digital computer models were increasing in complexity, and these models allowed rapid simulations with a wide variety of heart and systemic and pulmonary vascular parameters.[17, 18]

Current Computer and Working Heart Models

From the early 1990's to present, computing power and control systems using microcontrollers and virtual control circuits have greatly advanced. Products of these innovations were computer models incorporating neural feedback, mechanical flow

simulators, mechanical ventricles, more sophisticated afterloads, enhanced data collection and control methods, and combinations of the above. Computer modelers, such as Ursino,[19, 20] Olansen,[21] Chung,[22] and Davis and Gore,[23] developed models that allow manipulation of extensive parameters related to ventricular function, coronary circulation, systemic load and neural feedback. In 1991, Holdsworth et al.[24] published an article describing their positive displacement pump for simulation of physiological flow. A need for controlled pumps to simulate physiologic input led to the development of mechanical ventricles.[25-28] Coupling these substitute ventricles with mechanized afterloads provided more extensive experimental platforms for valve testing and flow description.[29-32] One such model is shown in Figure 1.3 from Gao et al.

Figure 1.3 Mechanical Afterload with Mechanical Ventricle. From Gao et al.[32] With kind permission of Springer Science and Business Media.

8

Working heart models are available commercially from ADInstruments and Radnoti Glass Technology Inc., http://www.adinstruments.com/applications/ and QuantaMetrics http://quantametrics.com/ and Harvard Apparatus http://www.harvardapparatus.com/. In addition, a porcine adaptation of the working heart setup was developed by Chinchoy et al.[33] http://www.visibleheart.com/background.html. Each of these experimental systems enables researchers to have a real-time view of ventricular behavior under a variety of afterload conditions.

Inspiration for My Current Work

Mechanical afterloads constructed by researchers such as Neely and Westerhof [8, 11] can be readily constructed but have few if any dynamic qualities for automatic adjustment of afterload parameters. Fisher et al. [34] demonstrated dynamic resistance control using a three-element windkessel-type afterload based on the work of Westerhof et al. [11] Though this control was used to maintain a desired mean pressure, the control did not extend to the compliance element. Current, commercially available working heart laboratory models also have their advantages and disadvantages. The working swine heart model introduced by Chinchoy et al.[33] is applicable for a working heart setup with both ventricles active, but this apparatus does not enable rapid, computer-controlled adjustment of afterload parameters. The working heart apparatus from ADInstruments and Radnoti Glass Technology Inc. provides methods for measurement of numerous parameters, such as AOP, AOF, resistance, compliance, and ECG. However, this device does not allow computer controlled afterload adjustments. QuantaMetrics' version of the working heart, which draws on a previous version by Neely et al.[8], allows afterload adjustments; however, their manipulations are not

computer controlled or dynamic. The working heart setup by Harvard Apparatus provides more individual control of afterload parameters, but this control is not implemented in a dynamic fashion. For researchers with a Langendorff apparatus already in place, a simple, attachable automatically adjustable afterload is desirable to transform the Langendorff non-working heart into a working heart mode. This afterload would ideally be controlled by widely available hardware and software, providing means for data collection and offline analysis.

Other considerations for a computer controlled afterload stem from numerous studies showing that arterial impedance changes alter the AOP and AOF waveforms, and these alterations are characteristic of certain physiological and pathophysiological conditions. Elzinga and Westerhof [35] demonstrated that isolated changes in resistance and compliance elements have a direct affect on the shape of the AOP and AOF waveforms. Milnor [36] noted that, not only is the arterial impedance spectrum altered by changes in afterload, but the characteristics of the coupled left ventricle also affect the final AOP and AOF waveforms. Modifications in ESPVR with afterload, heart rate and contractility changes have been published in a number of articles by Suga, Sagawa *et al*.[14, 37-39] Afterload parameter values and trends are available for several physiological conditions, including normal state, [40, 41] heart failure, [42, 43] exercise, [44] hypertension, [43] and many others. These studies suggest that a given physical state can typically be characterized by directional arterial impedance changes. Such changes will alter the AOP and AOF waveforms in a manner that is dependent on the properties of the coupled ventricle, including heart rate and contractility. A computer-controlled afterload must be able to adjust impedance values to match at least the major characteristics of various physiological and pathophysiological states. In most published

studies where physiological changes with afterload are investigated, impedance values are typically applied in fractional steps of some standard resistance or compliance value, for example ¼, ½, or 1 ½ times the standard. These adjustments reveal AOP, AOF and ventricular behavioral trends with varying afterload; however, the manipulations are crude and not representative of the continuous changes going on within the body. An afterload, designed to adjust dynamically (beat-to-beat), would provide a way to investigate transients of physiological behavior during afterload adjustments. Guidance for the dynamic adjustments could be derived from a control system that minimizes the error between a reference pressure (e.g. an AOP waveform indicative of some physiological condition) and the measured pulsatile input pressure. Afterload manipulations provide the ability to alter at least the major characteristics of an input pressure waveform, and certain of these waveform characteristics can be indicative of normo- or pathophysiological states. This suggests that the ability to match the characteristics of a reference pressure waveform using dynamically guided afterload adjustments might provide a method for imposing these normal or altered physiological states on the working heart.

Hypothesis

A dynamically adjustable afterload provides a physical setup in which afterload parameters can be automatically adjusted to cause a pulsatile pressure input to match reference pressure characteristics. Furthermore, a dynamic afterload constructed to provide impedance values and pulsatile pressure in a physiologic range is suitable for implementation with an isolated heart apparatus.

Specific Aims

The overall goal of my research was to construct a computer controlled, dynamically adjustable afterload that was suitable for implementation with an isolated heart apparatus. Certain steps were necessary before the construction of the afterload. The initial preliminary step was the development of a model of the left heart and systemic afterload to demonstrate relevant pressures and flows within the main circulatory path as influenced by impedance changes. This model would enable intelligent changes in afterload parameters and manipulation of AOP and AOF waveform shapes within the model to imitate normal or diseased states. Such a model was programmed in LabVIEW^{TM} and was published in the November 2005 issue of *Annals of Biomedical Engineering*. [45] This paper comprises Chapter 2. The final preliminary step was to provide a method for data collection and analysis for afterload testing. A LabVIEW^{TM} data collection and analysis station was programmed for this requirement. This program permits collection and analysis of simulation data generated from the dynamic afterload setup, providing a method for testing the impedance of the designed afterload. Chapter 3 discusses this data collection and analysis station.

Once the preliminary steps were completed, a dynamic afterload was constructed and tested. This device has computer-controlled afterload parameters for resistance, compliance and volume. A LabVIEW^{TM} control program drives impedance changes (based on previous model guidelines) to reduce the error between a reference pressure and measured pressure. The data collection and analysis station enabled testing of the physical system's functionality based on its pressure/flow outputs with a sinusoidal pump input. The dynamic afterload was modeled using an electrical analog windkessel-type model from our cardiovascular computer model (Chapter 2). Design and testing of the afterload is detailed in Chapter 4.

CHAPTER II

A LABVIEW[TM] MODEL INCORPORATING AN OPEN-LOOP ARTERIAL IMPEDANCE AND A CLOSED-LOOP CIRCULATORY SYSTEM[*]

While numerous computer models exist for the circulatory system, many are limited in scope, contain unwanted features or incorporate complex components specific to unique experimental situations. Our purpose was to develop a basic, yet multifaceted, computer model of the left heart and systemic circulation in LabVIEW™ having universal appeal without sacrificing crucial physiologic features. This computer model would be used to guide impedance parameter adjustments in the dynamic afterload we planned to construct. The program we developed employs windkessel-type impedance models in several open-loop configurations and a closed-loop model coupling a lumped impedance and ventricular pressure source. The open-loop impedance models demonstrate afterload effects on arbitrary aortic pressure/flow inputs. The closed-loop model catalogs the major circulatory waveforms with changes in afterload, preload, and left heart properties. Our model provides an avenue for expanding the use of the ventricular equations through closed-loop coupling that includes a basic coronary circuit. Tested values used for the afterload components and the effects of afterload parameter changes on various waveforms are consistent with published data. We conclude that this model offers the ability to alter several circulatory factors and digitally

catalog the most salient features of the pressure/flow waveforms employing a user-friendly platform. This establishes the model as a method whereby we can test the pressure and flow waveforms generated by our dynamic afterload and model the physical system's overall characteristics.

Introduction

A complex model is required to adequately convey many of the detailed hemodynamics inherent in the systemic circulation. Several experienced modelers have assembled multipart branching structures, such as tapered tube models and transmission line models, to capture many of the circulatory system's intricacies.[17, 46, 47] The consequences of an increasingly complex model are amplified computation time and a large number of adjustable parameters, both of which can be discouraging to novices in the field of cardiovascular modeling or those who have a more generalized need to investigate cardiovascular system dynamics. In contrast, the *Windkessel* model, developed by Otto Frank, has inspired numerous representations of the systemic circulation that condense the impedance characteristics of many circulatory elements into a much simpler configuration.[2, 48] These circulatory models were mainly in the form of hydrodynamic systems and electrical analogs that can now be numerically simulated using computers.

While lumped-parameter models of the circulatory system do not sufficiently portray more complex features of the circulatory impedance (e.g., wave propagation and reflection), open-loop versions of these simplified models do provide a way to observe the major aortic waveform characteristics in response to afterload changes.[3, 17, 49-51] With open-loop models, an isolated impedance representing the arterial system acts on a given input of either pressure

or flow. The input is unaffected by the load placed on it, and both source and sink are infinite. Therefore, the open-loop arrangement ignores such physiological phenomena as conservation of volume within the circulatory system. If a known aortic pressure or flow is used as the input to the system, changes in the respective flow or pressure output can be observed with alterations in afterload parameters. For example, the amplitude of the aortic pressure wave is markedly altered by peripheral resistance changes and the phase difference between aortic pressure and flow is modified as systemic compliance varies. Thus, open-loop models contain a relatively small number of parameters that effect predictable changes in circulatory dynamics. These models, in turn, reveal basic trends in aortic pressure and flow under the influence of systemic impedance changes.

While the behaviors observed in an open-loop model provide important insights into the effects of afterload variations, the circulatory system is closed-loop, conserving blood volume throughout the circulatory path, and input from the heart is affected by preload as well as afterload.[52-54] Coupling a left heart pressure source to the systemic afterload reveals important information on how changes in specific afterload components affect ventricular waveforms. For instance, ventricular pressure and elastance are altered during ventricular ejection by changes in input impedance.[52] Therefore, in addition to the systemic afterload, some modelers have closed the circulatory loop by including the left heart or a complete heart and pulmonary circuit.[17, 18, 55, 56] When the pulmonary circuit is not of vital interest, the right heart and pulmonary circuit may be lumped with the venous portion using a low-pass impedance in the circulatory path that permits the venous pressure to vary slowly over each cycle.[18, 57] In many closed-loop models, the heart is typically viewed as a chamber where elastance varies through the phases of systole and diastole.[13, 17] This chamber may be filled

15

from a constant pressure source representing the atrium,[53, 58] but a more realistic model permits the atrium to be refilled from a central venous reservoir.[17, 57] More recently, models of the left heart have been developed that describe the ventricle as a pressure source that is a function of ventricular volume, outflow, heart rate, and time.[1, 53, 58, 59] These models require the user to change only a few additional parameters for typical simulations.

Closed-loop models are more effective than open-loop models in accurately portraying general circulatory system behaviors. Caution must be exercised, however, when comparing open-loop and closed-loop performance. Open-loop and closed-loop systems are inherently different in behavior; therefore, strict application of open-loop performance to closed-loop performance is not a reasonable expectation. When the afterload is inserted into a closed-loop, the afterload performance is modulated by the preload and ventricular source, among other factors. This makes it impossible to draw direct comparisons of performance between open-loop and closed-loop circulatory models.

To improve the accuracy of information from a circulatory model, increasing degrees of complexity are required. For example, additional factors that are known to influence the heart and circulatory behavior include neural reflexes (such as the carotid baroreflex), the amount of coronary flow during diastole, and wave propagation and reflection in the arteries.[15, 17, 20, 50] A model expanded to include these features may provide numerous avenues for variability in circulatory system behavior and accurate response characteristics to parameter changes, but at the cost of computation time and model complexity. An ideal solution would be to identify a model with a minimal number of circulatory parameters that captures the main features of the system's response without undue complexity.

Our objective was to develop a cardiovascular model that enables students of cardiology and hemodynamics as well as novice modelers to become familiar with the behavior of the circulatory system under the influence of varying afterload and left heart parameters in both the closed- and open-loop configurations. Several computer models are available in the literature; however, many of these models are proprietary, excessively complex or have been developed using computer languages that are antiquated, difficult to interface with existing laboratory equipment, or costly. These concerns can be avoided by utilizing a modern, user-friendly computer interface with a simplified circulatory analog. We sought to produce a model that incorporated a left heart input source with a lumped-parameter afterload using widely available multiplatform software. This model could serve as an effective tool to illustrate the overall hemodynamics of the circulatory system. Moreover, the model provides a convenient method for initial experimentation with various combinations of circulatory parameters in both clinical and laboratory settings.

Methods

Overview of the Model

Open-loop Configuration

The model employs an electrical analog for the fluid-based cardiovascular system. The two basic components of the model are an open-loop afterload for input of aortic pressure/flow and a closed circuit arrangement with the left heart providing the pressure source. Several types of lumped-parameter afterloads with varying degrees of complexity are employed for the open-loop portion (Figure 2.1). These include a two-element (2-E) *Windkessel* afterload, a three-element (3-E) *Westkessel* afterload, and two different four-element afterloads (termed 4-E and 4-E Alt. afterload). In the literature, no consistent way of

defining the role of each afterload component exists. Therefore, components of the afterloads and the associated pressures and flows are defined in a manner that essentially agrees with several investigators [3, 11, 17, 60] as shown in Table 2.1. Since our model employs two different 4-E impedances, a brief explanation of each element follows.

In both models, the parallel R_s and C_s represent the resistance and compliance of the arteries, arterioles and capillaries. The Z_o element is termed the characteristic impedance of the aorta and is defined as the impedance the aorta would exhibit in the absence of wave reflections.[3] Stergiopulos, Rideout and others use the inductor (I_s) to embody the inertance of the mass of blood moving through the arteries.[17, 60] It is common for modelers to place the inertial term in series with Z_o [17, 18, 46, 52] per transmission line theory on which the additional impedance elements are based. The 4-E Alt. model from Stergiopulos, however, uses a parallel arrangement of Z_o and I_s. The inertial term is then defined as "the summation of all local inertances of the arterial system".[60] The effect this has on impedance at various frequencies is covered subsequently in the discussion.

Each afterload model is described by a differential equation relating aortic pressure (P_a) and aortic flow (Q_v). We opted to generate waveforms using differential equations in the time domain, as opposed to impedance methods, for the following reasons: time domain methods have a broader base of familiarity among students of cardiology at all levels of understanding, the precision afforded by the time domain methods is sufficient for the purposes of our model, and the ventricular model (discussed below) adapted from literature was developed in the time domain, thereby giving consistency to both parts of the model. Equations for both 4-E models are given below [equations 1 and 2]. By setting I_s to zero, the 4-E model equation is reduced to the 3-E afterload equation, and, by setting both I_s and Z_o to

zero, the 2-E afterload equation is obtained. The 4-E Alt. afterload equation cannot be reduced to a 3-E state by setting I_s to zero. Instead, this equation reduces directly to a 2-E model.

4-E model:

$$\frac{dP_a}{dt} = I_s \frac{d^2Q_v}{dt^2} + \left(Z_O + \frac{I_s}{R_sC_s}\right)\frac{dQ_v}{dt} + \left(\frac{1}{C_s}\right)\left(1 + \frac{Z_O}{R_s}\right)Q_v - \frac{P_a}{R_sC_s} \qquad\qquad 1$$

4-E Alt. model:

$$R_sC_sI_s\frac{d^2P_a}{dt^2} + \left(I_s + R_sZ_OC_s\right)\frac{dP_a}{dt} + Z_OP_a = R_sZ_OI_sC_s\frac{d^2Q_v}{dt^2} + \left(R_sI_s + Z_OI_s\right)\frac{dQ_v}{dt} + R_sZ_OQ_v \qquad\qquad 2$$

A time expression for P_a or Q_v is generated in LabVIEW^{TM} by first taking the Fast Fourier Transform (FFT) of data points describing one period of an aortic pressure or aortic flow waveform. This transform is then converted into a time domain expression using as many as 25 harmonics. With either the P_a or Q_v time expression as input, the differential equation is solved using a fourth order Runge-Kutta routine (step size 0.005) in LabVIEW^{TM} for the respective output.

Table 2.1 Summary of Open-loop Model Parameters

Pressure and Flow Designations						
Symbol	Description				Initial Value	Units †
P_a	Aortic Pressure				80.0	mmHg
Q_v	Ventr. outflow (aortic flow)				0.0	ml s^{-1}
Impedance Parameters*						
Symbol	Description	2-E	3-E	4-E	4-EAlt	Units †
R_s	Systemic resistance post-aorta	0.7	0.7	0.65	0.63	mmHg s ml^{-1}
C_s	Systemic compliance (arteries)	3.1	3.1	2.8	2.53	ml mmHg^{-1}
Z_o	Characteristic impedance of aorta		0.03	0.028	0.045	mmHg s ml^{-1}
I_s	Inertance of arterial system			0.0018	0.0054	mmHg s^2 ml^{-1}

* Typical values used for each lumped impedance configuration
† Unit conversions (dyne cm^{-2}) = (7.5025e^{-4} mmHg) and (cm^3) = (ml)

Closed-loop Configuration

The closed-loop portion of the model that employs the left-ventricular pressure source is shown in Figure 2.1. This model had its origin in the closed-loop models of Palladino *et al.,* [56, 57] but with notable additions. A coronary feedback portion is inserted in our model and inertance terms are included in the forward path of ventricular outflow. Additionally, the mathematical description of the left ventricle that we employ is based on later models by Ottesen *et al.*[52, 53, 58] Certain portions of the model, especially the coronary circulation and the right heart and pulmonary circulation, are overly simplified by using minimal resistance and compliance circuits. Our current use of the model renders the pulmonary portion of the circuit unnecessary, thus we have bypassed this region in the present version of the model (similar to Palladino *et al* [57] and a simplified lumping of the left heart cited by Lucas [18]). The coronary circulation has been modeled by several investigators [61-65] and can involve somewhat complicated circuits with varying impedances for different portions of the coronary circulation and myocardium. Our present use of the ventricular pressure source precludes a knowledgeable coupling of this circulation to the contractility and other functional parameters of the ventricle. Therefore, with known limitations, we used a simple RC arrangement to conserve blood volume within the model. This approach is covered later in the discussion. Equations that describe the behavior of the left ventricle are provided in the literature [52, 53, 58, 59] and are presented with a brief description in equations 3-9. Parameter definitions and typical values for the model are provided in the literature [56, 58] and summarized in Table 2.2. While based on experimental data, some of the parameters have not been quantified specifically for changes in afterload (personal communication with J.T. Ottesen, May 2003). Therefore, certain parameter values were altered slightly from the

literature values to provide more regular waveform outputs and accommodate a greater range

of heart rate changes. Modified values are indicated in Table 2.2.
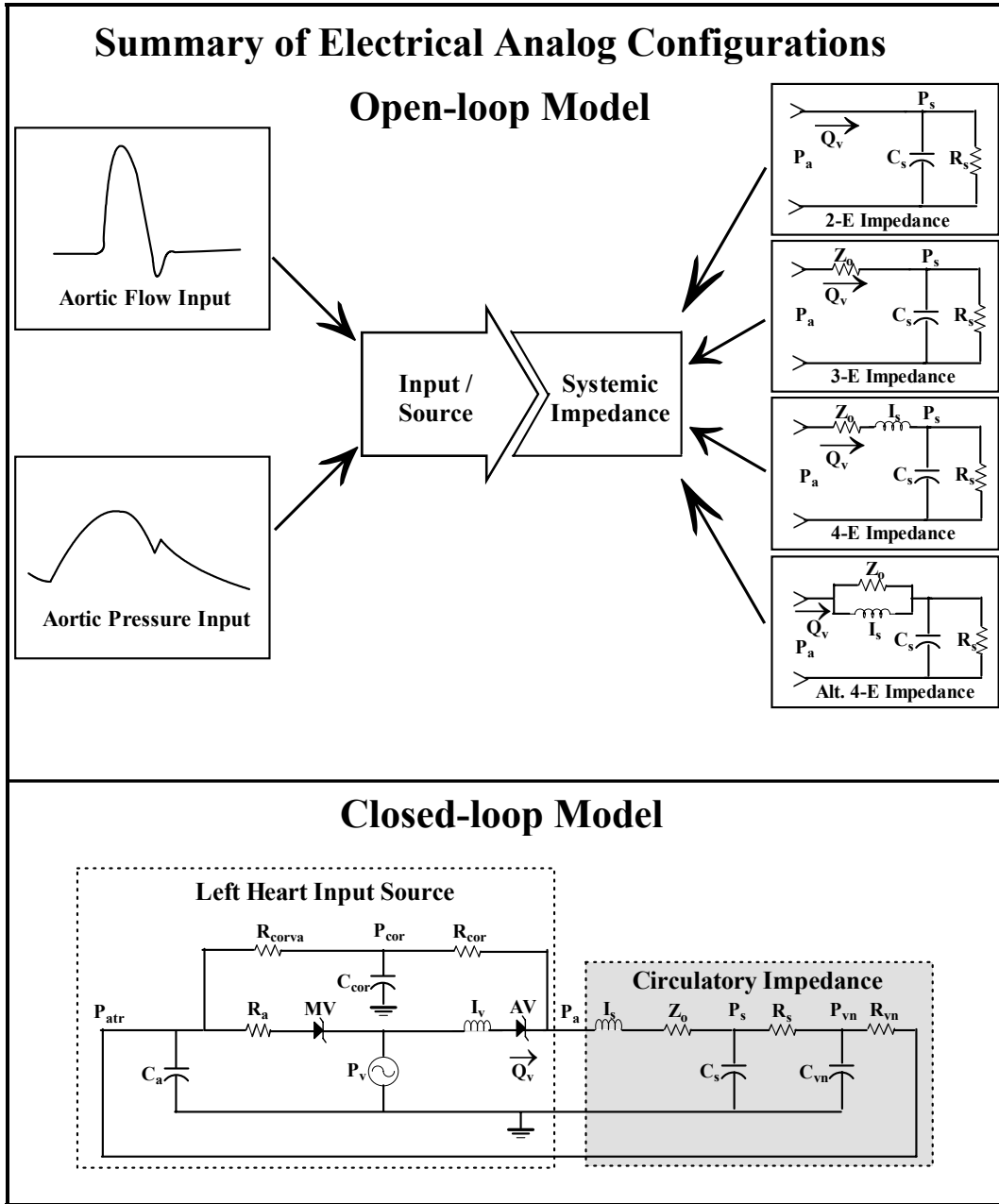
Figure 2.1 Summary of Electrical Analog Configurations. The model provides two methods for analyzing cardiovascular system behaviors: an open-loop model with digital waveform inputs and a closed-loop model with a left heart pressure source. AV and MV represent the aortic valve and mitral valve respectively. The other impedance parameters are defined in Table 2.1.

Table 2.2 Summary of Ventricular Model Parameters†

Symbol	Description	Value	Units††
a	Ventricular elastance (relaxation phase)	0.0007	mmHg ml^{-2}
b	Ventricular volume (at 0 diastolic pressure)	5	ml
c	Relates to volume-dependent developed pressure	1.92	mmHg ml^{-1}
d	Relates to volume-independent developed pressure	1	mmHg
*k_1	Corrects for calculated pressure differences (early systole)	5e^{-4}	s ml^{-1}
*k_2	Corrects for calculated pressure differences (late systole)	1e^{-6}	s ml^{-2}
*κ	Denotes change in rate of crossbridge cycling with time	0.52	
α	Denotes time for onset of contraction	0	s
m	Constant that alters speed of relaxation phase	2.2	
n	Constant that alters speed of contraction phase	2	
θ	Median of Hill function relation $t_p(H)$ (Equation 10)	1	Hz
υ	Steepness of $t_p(H)$	9.9	
*$t_{p\,min}$	Minimum time to peak pressure for $t_p(H)$	0.17	s
$t_{p\,max}$	Maximum time to peak pressure for $t_p(H)$	0.2799	s
ϕ	Median of Hill function relation $P_p(H)$ (Equation 8)	1	
η	Steepness of $P_p(H)$	17.5	
$P_{p\,min}$	Minimum value of peak pressure relation $P_p(H)$	0.842	
$P_{p\,max}$	Maximum value of peak pressure relation $P_p(H)$	1.158	

* Parameters altered from literature values to allow increased heart rate range and afterload changes
† Parameters obtained from Ottesen, Danielsen, et. al.[52, 53,58,57]
†† Unit conversions (dyne cm^{-2}) = (7.5025e^{-4} mmHg) and (cm^3) = (ml)

Equations 3-9 have been published previously.[52, 53, 58, 59] See Table 2.2 for abbreviations and definitions.

P_v as a function of t (time in sec), V_v, Q_v, H (heart-rate frequency in Hz):

$$P_v(t,V_v,Q_v,H) = a(V_v - b)^2 + (cV_v - d)F(t,Q_v,H) \qquad 3$$

where $F(t,Q_v,H)$ is the unitless ventricular activation function [equation 5].

Left-ventricular elastance (E_v (mmHg ml^{-1})):

$$E_v(t,V_v,Q_v,H) = \frac{\partial P_v}{\partial V_v} = 2a(V_v - b) + cF(t,Q_v,H) \qquad 4$$

Left-ventricular activation function:

$$F(t, Q_v, H) = f(t, H) - k_1 Q_v + k_2 Q_v^2 (t - \tau)$$ 5

where $f(t, H)$ is a normalized activation function [equation 6] and $\tau = \kappa t$ (time variable time delay (sec)).

$$f(t, H) = \begin{cases} P_p(H) \left[\dfrac{(t - \alpha)^n (\beta(H) - t)^m}{n^n m^m \left(\dfrac{\beta(H) - \alpha}{m + n} \right)^{m+n}} \right] & \xrightarrow{\text{for}} \alpha \leq t \leq \beta(H) \\ \\ 0 & \xrightarrow{\text{for}} \beta(H) \leq t \leq t_h(\text{period}) \end{cases}$$ 6

Peak ventricular pressure as a function of heart rate frequency ($P_p(H)$):

$$P_p(H) = P_{p_{min}} + \left[\frac{H^\eta}{H^\eta + \phi^\eta} \right] \left(P_{p_{max}} - P_{p_{min}} \right)$$ 7

Time for onset of ventricular relaxation as a function of heart rate frequency ($\beta(H)$):

$$\beta(H) = \frac{n + m}{n} t_p(H) - \frac{\alpha m}{n}$$ 8

Time for peak ventricular pressure as a function of heart rate frequency ($t_p(H)$):

$$t_p(H) = t_{p_{min}} + \left[\frac{\theta^\upsilon}{H^\upsilon + \theta^\upsilon} \right] \left(t_{p_{max}} - t_{p_{min}} \right)$$ 9

Equations that describe the cycle and couple the left-ventricular pressure source with the circulatory analog are given below. A description of the system behavior was generated by nodal analysis employing conservation of volume. For succinctness, the equations are presented as a single expression [equation 10] in state space form followed by a brief description of the boundary conditions employed. Table 2.3 provides definitions and initial values for the various elements of the closed-loop model.

Table 2.3 Summary of Closed-loop Model Parameters

Pressure , Volume, Flow Designations

Symbol	Description	Initial Value	Units †
P_v	Ventricular Pressure	10	mmHg
P_a	Aortic Pressure	85	mmHg
P_{atr}	Atrial pressure	8	mmHg
P_{cor}	Coronary Pressure	85	mmHg
P_s	Pressure in the main arteries post-aorta	85	mmHg
P_{vn}	Pressure in the venous system	10	mmHg
V_t	Total system volume	4972	ml
V_{sa}	Volume in systemic arteries (total)	787	ml
V_{sau}	Unstressed volume in systemic arteries	600	ml
V_{vn}	Volume in venous system (total)	4000	ml
V_{vnu}	Unstressed volume in venous system	3000	ml
V_{cor}	Volume in coronaries (total)	15	ml
V_{coru}	Unstressed volume in coronaries	15	ml
V_a	Volume in atrium	50	ml
V_v	Ventricular volume	120	ml
Q_v	Ventricular outflow (aortic flow)	0	ml s^{-1}

Impedance and System Parameters

Symbol	Description	Value*	Units †
R_a	Resistance from left atrium to left ventricle	1e^{-3}	mmHg s ml^{-1}
I_v	Inertance of blood ejecting from left ventricle	4.16e^{-4}	mmHg s^2 ml^{-1}
R_{cor}	Initial resistance of coronary arteries	0.12	mmHg s ml^{-1}
C_{cor}	Compliance of coronary circulation	0.15	ml mmHg^{-1}
R_{corva}	Resistance of venous side of coronary circulation	0.15	mmHg s ml^{-1}
C_a	Compliance of left atrium	5	ml mmHg^{-1}
R_s	Systemic resistance post-aorta	0.85	mmHg s ml^{-1}
Z_o	Characteristic impedance of aorta	0.075	mmHg s ml^{-1}
C_s	Systemic compliance of arteries	2.20	ml mmHg^{-1}
I_s	Inertance of arterial system	0.001	mmHg s^2 ml^{-1}
C_{vn}	Compliance of venous system	100	ml mmHg^{-1}
R_{vn}	Resistance of venous system	0.011	mmHg s ml^{-1}

Cardiac Cycle Values (after 4 cycles)

S.V.	Stroke volume	71.70	ml
E.F.	Ejection Fraction	0.58	
MAOP	Mean aortic pressure	94.02	mmHg
H.R.	Typical initial heart rate	75	b.p.m.

* Typical values used for the impedance parameters
† Unit conversions (dyne cm^{-2}) = (7.5025e^{-4} mmHg) and (cm^3) = (ml)

Equation 10: State Space Representation of the Closed-loop Model

$$
\begin{bmatrix} \dot{Q}_v \\ \dot{P}_s \\ \dot{P}_{vn} \\ \dot{P}_{atr} \\ \dot{V}_v \\ \dot{P}_{cor} \\ \dot{V}_{cor} \end{bmatrix}
=
\begin{bmatrix}
\dfrac{-\chi\varepsilon Z_o}{\gamma\delta I_v + I_s} - \dfrac{\chi\varphi\varepsilon R_{cor}}{I_s} & \dfrac{-\chi\varepsilon}{\gamma\delta I_v + I_s} & 0 & 0 & 0 & \dfrac{\chi\varphi\varepsilon}{I_s} & 0 \\[2mm]
\dfrac{1}{C_s} & \dfrac{1}{C_s R_s} & \dfrac{-1}{C_s R_s} & 0 & 0 & 0 & 0 \\[2mm]
0 & \dfrac{1}{C_{vn} R_s} & \dfrac{-1}{C_{vn} R_s} - \dfrac{1}{C_{vn} R_{vn}} & \dfrac{1}{C_{vn} R_{vn}} & 0 & 0 & 0 \\[2mm]
0 & 0 & \dfrac{1}{C_a R_{vn}} & \dfrac{-1}{C_a R_{vn}} - \dfrac{1}{C_a R_a} & 0 & 0 & \dfrac{\left(1 - V_{cin}/V_{cor}\right)}{C_a C_{cor} R_{corva}} \\[2mm]
-\chi\gamma\delta\varepsilon & 0 & 0 & \dfrac{\chi\varphi\gamma\delta}{R_a} & 0 & 0 & 0 \\[2mm]
\dfrac{\varphi\gamma\delta\varepsilon}{C_s} - \dfrac{\chi\varphi\delta\varepsilon}{C_{cor}} & \dfrac{\varphi\gamma\delta\varepsilon}{C_s R_s} & \dfrac{-\varphi\gamma\delta\varepsilon}{C_s R_s} & 0 & 0 & 0 & 0 \\[2mm]
-\chi\varphi\delta\varepsilon & 0 & 0 & 0 & 0 & 0 & \dfrac{-\left(1 - V_{cin}/V_{cor}\right)}{C_{cor} R_{corva}}
\end{bmatrix}
\begin{bmatrix} Q_v \\ P_s \\ P_{vn} \\ P_{atr} \\ V_v \\ P_{cor} \\ V_{cor} \end{bmatrix}
+
\begin{bmatrix} \dfrac{\chi\gamma\delta\varepsilon}{I_v + I_s} \\[2mm] 0 \\ 0 \\ \dfrac{1}{C_a R_a} \\[2mm] \dfrac{-\chi\varphi\gamma\delta}{R_a} \\[2mm] 0 \\ 0 \end{bmatrix} P_v
$$

The state space equation describes the behavior of the cardiovascular model throughout the cardiac cycle. In order to account for the nonlinear elements in the circuit model, one period of the cycle is divided into five basic parts, in effect providing piecewise linearization of the circuit during these segments. The constants χ, φ, γ, δ, ε are used to modify the state space equation as necessary by being set to zero during a specific portion of the cycle and 1 at all other times. This division of the cycle is shown more fully in Figure 2.2.

Phases of the Cardiac Cycle
in the Closed-loop Model

χ	0	1	1	1	1	
φ	1	0	1	1	1	
γ	1	1	0	1	1	
δ	1	1	1	0	1	
ε	1	1	1	1	0	
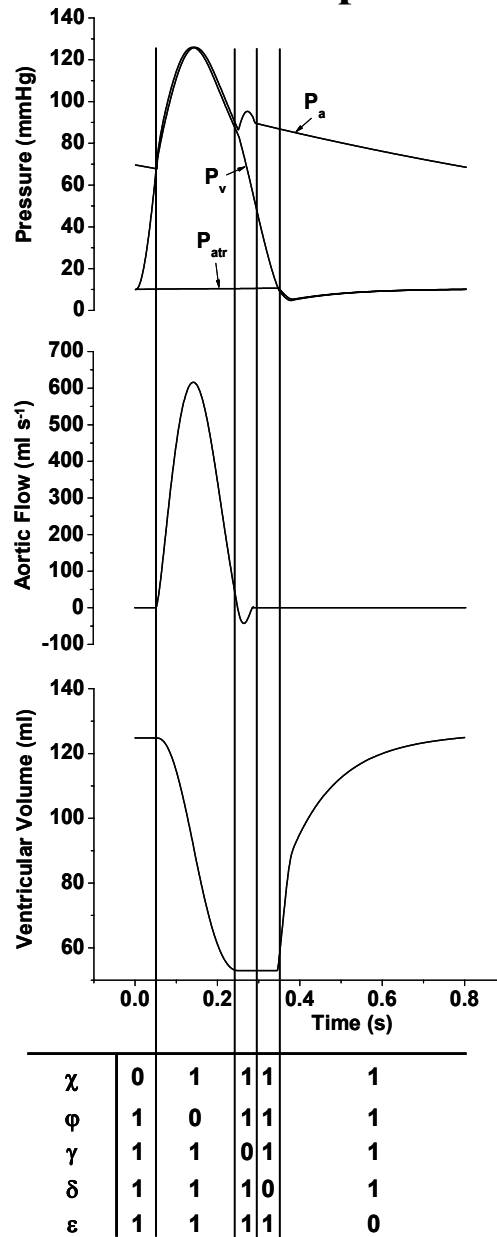
Figure 2.2 Phases of the Cardiac Cycle in the Closed-loop Model. One steady-state cardiac cycle generated by the closed-loop model to demonstrate the different phases assigned during the cardiac cycle to produce piecewise linearization. Each phase has an associated set of differential equations determined by the values of $\chi,\varphi,\gamma,\delta,\varepsilon$ (see Equation 10).

26

The first part of the cycle ($\chi=0$) is pre-ejection and partial refilling of the ventricle. Subsequently the ventricle ejects and $\varphi=0$. As the ventricle ejects, P_{cor} is allowed to follow P_a and the differential equation for P_{cor} is calculated iteratively as the time rate of change of P_a. When negative flow occurs, $\gamma=0$, and the sign of the Z_o term in the Q_v differential equation is changed. While the flow settles to zero, $\delta=0$, and the flow contribution to systemic volume is eliminated by subtracting the unsettled flow term from the P_s equation. In the final portion of the cycle, $\varepsilon=0$ as refilling occurs. The constant V_{cin} (occurring in the P_{atr} and V_{cor} differential equations) represents the initial unstressed volume of the coronary circulation. Certain conditions must also apply to the equations above in order to accurately represent the physiology involved. When the atrial pressure increases above the venous pressure, no backflow occurs from the atrium to the venous side, and this portion of the differential equation is set to zero. Similarly, while the ventricular pressure is greater than the atrial pressure no flow occurs from ventricle to atrium. Therefore, this portion of the P_{atr} differential equation is set to zero. These sets of differential equations were solved using a fourth-order Runge-Kutta routine (step size 0.001) in LabVIEW^{TM}.

Verification of Model Results

Open-loop Configuration

To validate the isolated afterload portion of the model, aortic pressure/flow tracings available in the literature with associated afterload values [11, 40, 41, 60] were scanned and digitized using UnGraph from Biosoft®. Since these digitized waveforms were not exact reproductions, they were used only to verify that the different afterloads would generate corresponding waveforms with realistic timing and magnitude. This process involved using

either the aortic pressure or flow as input and comparing the magnitude, timing and basic characteristics of the resulting output waveform. The outputs are dependent on afterload parameters, and very few literature waveforms have associated impedance values. One set of waveforms with associated afterload parameters was published by Stergiopulos and Westerhof,[60] and a match of the input/output for these waveforms is provided in the results (Figure 2.3). Using the scanned aortic pressure (AOP) waveform as input to the 4-E Alt. model, with the afterload parameters given by Stergiopulos, the aortic flow (AOF) output was obtained. Then, using the same afterload parameters, the scanned AOF waveform was employed as input, and the AOP output was produced.

For most all other cases, in order to generate outputs from the digital tracings, estimates were made for the afterload parameters. This was done by approximating values from the literature.[11, 40, 41, 60] The values for R_s, C_s, Z_o, and I_s were then adjusted to provide a waveform similar in scale and timing to the expected output. For these reasons, no specific criteria were developed for testing these outputs. The outputs were considered acceptable if they were within 20% of the magnitude and timing provided in the literature and the afterload values were in the typical range of those found in previous studies.

An interesting advantage of the open-loop model is its ability to compare outputs from the same input using different afterload configurations. This permits a comparison of impedance parameter values to distinguish which arrangement of the afterload might provide the best output for a given input waveform. Also, the user can determine which configurations are more responsive to changes in a particular afterload element. An example of this type of comparison is provided in Figure 2.4. Note that the typical impedance values provided in Table 2.1 are not meant to correspond to the simulations in Figure 2.4. The values in Table

2.1 were employed with the previously published waveforms from Stergiopulos and

Westerhof (illustrated in Figure 2.3 and used within the model as a typical AOP and AOF).

Closed-loop Configuration

With the closed-loop model, no arbitrary waveform inputs were possible, because the

equations for ventricular pressure drive the system and cannot be modified to allow arbitrary

inputs. Unfortunately, this prevented a direct comparison of how our closed-loop model

would act on the same input waveform with similar impedance parameters used in the open-

loop simulations. Therefore, the closed-loop model's outputs were cataloged and used as a

method of validation by comparing model results to waveform trends found in the

literature.[13, 38, 56, 66, 67] The effects were cataloged for single parameter changes and for

combinations of changes. Single parameter effects were analyzed by choosing three different

values for an afterload element (e.g. R_s = 0.5, 0.85, and 1.2). Several cycles of a given output

were cataloged. A steady-state cycle (typically the 4th or higher to allow settling of transient

effects) was then chosen and graphed for these three values. The typical values chosen for

the afterload parameters were well within the range of values found in the literature, and the

range of values chosen to test the model's sensitivity and demonstrate output trends was

based on the inherent variability in afterload impedance values. The values of R_s, C_s, and Z_o

can all vary markedly within the normal population of the same species (e.g. the systemic

resistance for one subject might be ½ the value of the next subject).[40, 41, 60, 68] In addition, R_s

can vary under conditions such as exercise and heart failure.[42, 44, 69, 70] Characteristic

impedance can also increase substantially with heart failure,[42, 43, 70] and significant changes in

systemic compliance can occur with conditions such as atherosclerosis, hypertension and

heart failure.[43, 69, 71, 72] In order to maintain afterload parameter values in the physiologic ranges reported in literature and to achieve reasonable volumes in the various cardiovascular spaces, unstressed volumes were added to certain portions of the model (systemic venous, systemic arterial, and coronary). All volumes for the model are reported for a standard waveform in Table 2.3.

The categories of waveforms used as an illustration of output trends were P-V loops and aortic pressure/flow. Two types of P-V loop plots were created. The first type was the pressure-volume relation using a constant preload and allowing the chosen afterload parameter to vary over its three values. The second type was the pressure-volume relationship using a constant value for the afterload parameter and adjusting the central venous pressure which allowed the preload to vary over a number of starting volumes. An End-Systolic Pressure-Volume Relationship (ESPVR) was generated for each of the two types of P-V loop plots in order to demonstrate overall tendencies. The ESPVR was generated (using a method similar to Maughan *et al.* [38]) by determining the point in the P-V loop where the pressure to volume ratio was the largest. This provided an estimate of the points at end systole on the various pressure-volume curves. These points were then plotted and a linear best-fit line (ESPVR line) was generated. The standard ESPVR line (ESPVR$_1$) was determined by using the P-V loops generated using a constant afterload with typical afterload values and a varying preload. ESPVR lines under the influence of changing afterload (ESPVR$_2$, ESPVR$_3$) were determined from P-V loops with a constant preload and varying afterload parameter values. Additional ESPVR lines were generated for constant afterload and varying preload using incremental values of R_s and C_s. Trends for all waveforms and ESPVR characteristics were compared to the literature data when available.

With multiple parameter changes, a similar protocol was employed as for the single

parameter changes, the only difference was in allowing the additional combinations (e.g. R_s =

0.5 and C_s = 1.0, R_s = 0.85 and C_s = 2.0, R_s = 1.2 and C_s = 1.0,…). For multiple parameter

changes, few if any literature comparisons were available; therefore, only trends for single

parameter changes are presented in the results. Aortic pressure/flow waveforms were

produced with the same range of single-parameter afterload changes. These pressures and

flows append the information already present in the P-V loops, and they demonstrate the

level of detail generated by the model.

The focus of our model is on the waveforms of the ventricle and aorta in response to

afterload changes, thus, these waveforms are presented as results. Additional outputs, such

as the cardiac cycle in Figure 2.2, venous pressure, total volume, mean aortic pressure

(MAOP), stroke volume (SV), ejection fraction (EF) and coronary volume/flow are also

commented on in the results to provide a rounded view of the model's behavior.

Statistical Analysis

In order to assess the agreement of P-V loops generated by the model with previous

physiologic experiments, statistical analysis was performed on the data for the ESPVR slope

(E_{ves}) and intercept (V_o). The slope and intercept of the linear best-fit lines generated under

each set of afterload conditions were compared to the standard $ESPVR_1$ line using a small-

sample two-tailed t-test for parallelism and common intercept.[73] A percent difference

between the standard slope and the slope of the lines under varying afterloads was generated

for further assessment. The magnitude of the change in V_o between the $ESPVR_1$ line and the

lines generated with different impedance parameters is also provided for comparison.

Results

Open-loop Configuration (Figures 2.3 & 2.4)

As an illustrative simulation from the open-loop portion of the model, aortic pressure/flow

waveform pairs are shown in Figure 2.3.

Open-loop Aortic Pressure and Aortic Flow Waveform Comparisons
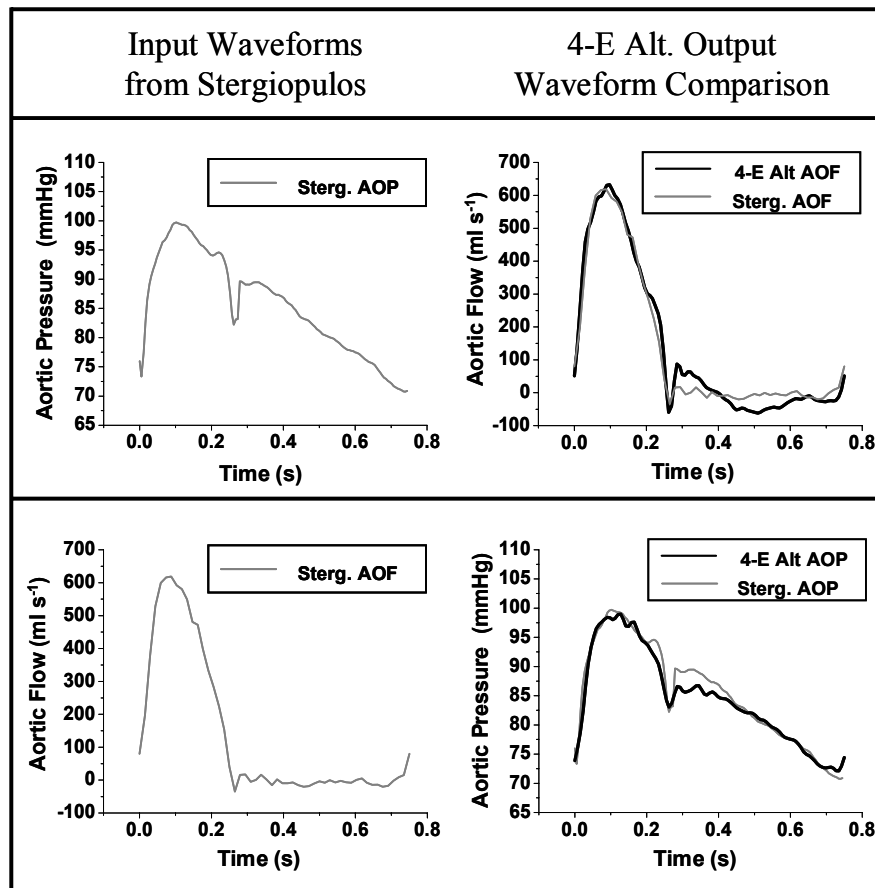
Figure 2.3 Open-loop Aortic Pressure and Flow Waveform Comparisons. Scanned and digitized aortic flow (AOF) and aortic pressure (AOP) input waveforms from Stergiopulos and Westerhof [60] (pg. H85 fig. 4 panels A and B of type C) are compared to steady-state aortic flow and aortic pressure generated using the 4-E Alt. afterload model. Using the measured AOP from Stergiopulos as input (top left gray), AOF was generated (top right black) and compared to the measured AOF from Stergiopulos (top right gray). Likewise, using the measured AOF from Stergiopulos as input (bottom left gray), AOP was generated (bottom right black) and compared to the measured AOP from Stergiopulos (bottom right gray). Simulation parameters were $R_s = 0.63$ mmHg s ml^{-1}, $C_s = 2.53$ ml mmHg^{-1}, $Z_o = 0.045$ mmHg s ml^{-1}, $I_s = 0.0054$ mmHg s^2 ml^{-1}, heart rate 80 b.p.m.

This figure demonstrates open-loop outputs that are in good agreement with the matching AOP and AOF inputs published by Stergiopulos and Westerhof.[60] These waveforms were scanned and digitized, as described in Methods. Note that Stergiopulos does not provide an output AOF waveform using an AOP input. This simulation was added to provide a more complete validation of our 4-E Alt. implementation.

An additional illustration of the open-loop afterload is given in Figure 2.4. An aortic pressure was the input to each afterload, and the parameters used for the simulation are noted. No impedance values or matching aortic flow waveform was available, so impedance values were estimated as described in Methods. The inability of the 2-E model to reduce the high frequency waveform components is illustrated in part B of Figure 2.4. For the 3-E and two 4-E models, AOF waveform outputs are slightly different, but of acceptable form with regard to magnitude, negative flow and noise. Though the two 4-E models did not have parameters fit by waveform matching, impedance moduli or other methods, it is notable that the 4-E model with Z_o and I_s in series appears to require higher values of R_s and C_s but lower values of Z_o and I_s when compared to the 4-E Alt. model. This is true for both the simulations in Figure 2.4 and those carried out with the typical AOP and AOF (Table 2.1). A brief explanation of the frequency characteristics of each afterload is provided in the Discussion.

Aortic Pressure/Flow with Various Open-Loop Impedances
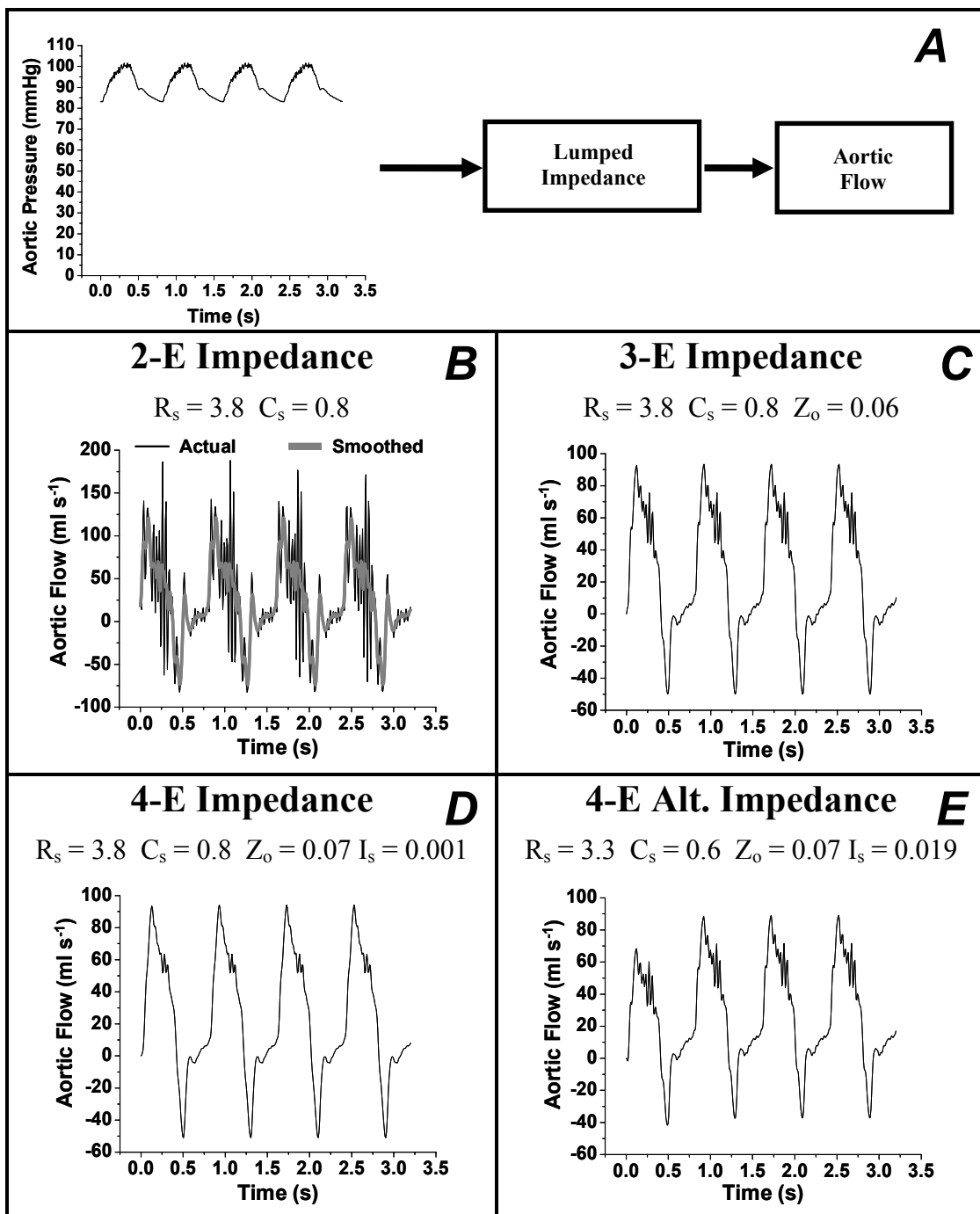
Figure 2.4 AOP/AOF for Various Open-Loop Impedances. Identical AOP input (part *A*) to the four types of open-loop impedances with resultant AOF. Impedance parameters were estimated with a heart rate of 75 b.p.m. The AOP waveform was from a 10-20 kg lamb (undergoing a mid-sternal thoracotomy) (courtesy of M. Ketner and C.L. Lucas, Department of Biomedical Engineering, University of North Carolina at Chapel Hill).

Closed-loop Configuration (Figures 2.5 – 2.8)

Figure 2.5 shows three sets of P-V loops. Each set was generated with a constant R_s value while varying preload over a range of initial volumes. Panel B of the figure illustrates the P-V loops with typical afterload values (i.e. those values used in the model for a standard waveform as given in Table 2.3). The end-systolic pressure-volume relationship for these typical values ($ESPVR_1$) is indicated in all panels. The trends for afterload changes are recorded in Table 2.4. As R_s increases, the slope of the ESPVR line (corresponding to ventricular elastance at end-systole, E_{ves}) increases only slightly. A directional difference is also seen in the volume axis intercept, with increasing R_s giving a decreasing intercept. The changes in E_{ves} seen in Figure 2.5 were not significant, and the actual percent change for all panels was 2% or less. In the case of V_o, changes in intercept were significant, but were still small in magnitude (< 2.0 ml for both cases). If the preload remains constant with changing R_s, as in Figure 2.6C, much larger differences occur in the slope of the ESPVR lines. Table 2.4 reveals that, as R_s is elevated, E_{ves} shows an increase of over 23%. Furthermore, V_o is shifted well to the right. The P-V loops themselves indicate less volume flow and higher pressures with increased R_s. The AOP and AOF plots in Figure 2.6 (A and B) illustrate this fact by showing higher AOP and lower AOF with increased R_s.

PV loops with constant R_s and varying preload
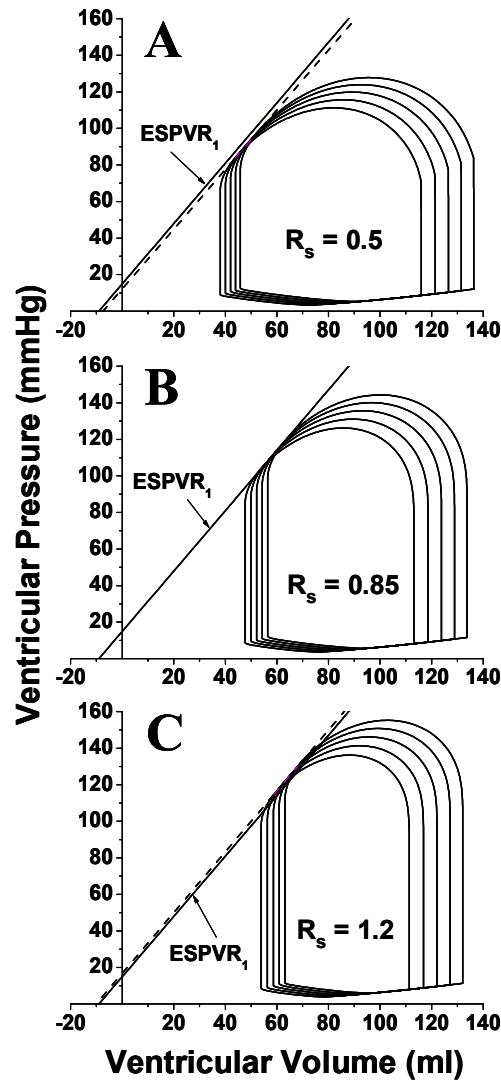
Figure 2.5 P-V Loops with Constant R_s and Varying Preload. P-V loops were generated as R_s was held constant at one of three values (0.5, 0.85 or 1.2 mmHg s ml^{-1}), and preload was varied over the range 8-12 mmHg. The average cycle values with standard error for mean AOP (mmHg), SV (ml) and EF, respectively, are: for part A (72.64 ± 4.58, 84.39 ± 4.96, 0.668 ± 0.004), for part B (93.90 ± 5.35, 71.57 ± 4.68, 0.58 ± 0), for part C (108.01 ± 5.81, 63.36 ± 4.55, 0.52 ± 0). The standard $ESPVR_1$ line (solid) is shown in all three panels as a reference for the ESPVR line (dashed) calculated using each set of simulation data.

Waveforms with varying R_s
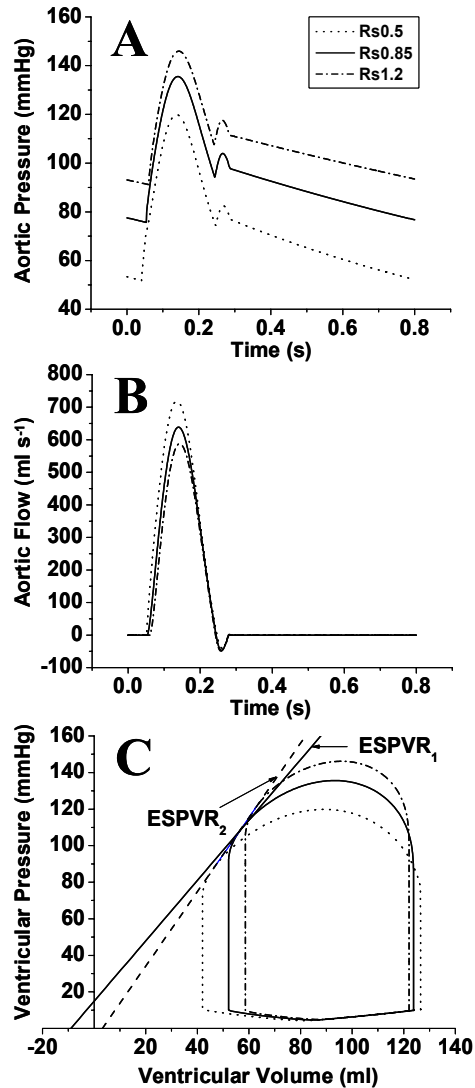
Figure 2.6 Waveforms with Varying R_s. Steady-state cardiac cycle waveforms were generated at three different values of R_s (0.5, 0.85, and 1.2 mmHg s ml^{-1}). The cycle values for AOP (mmHg), SV (ml) and EF, respectively, are: for R_s = 0.5 (72.73, 84.53, 0.67), for R_s = 0.85 (94.02, 71.70, 0.58), for R_s = 1.2 (108.22, 63.50, 0.52). The standard ESPVR$_1$ line (solid) is shown panel C as reference for the ESPVR$_2$ line (dashed) calculated using each set of simulation data.

Table 2.4 ESPVR Slope and Intercept Comparisons

	E_{ves}	% change †	V_o	$|\Delta V_o|$ †
ESPVR$_1$ ††	1.652	0	-8.998	0
ESPVR ($R_s = 0.5$)	1.634**	-1.09	-7.413*	1.585
ESPVR ($R_s = 1.2$)	1.664**	0.74	-10.063*	1.065
ESPVR ($C_s = 1.0$)	1.782*	7.87	-6.515*	2.483
ESPVR ($C_s = 3.4$)	1.573*	-4.79	-11.466*	2.468
ESPVR$_2$	2.032*	23.02	3.217*	12.215
ESPVR$_3$	4.123*	149.61	30.48*	39.474

† Relative to values for ESPVR$_1$
†† ESPVR$_1$ generated using $R_s = 0.85$ and $C_s = 2.2$
* Significantly different from ESPVR$_1$ ($p<0.01$).
** No significant difference from ESPVR$_1$.

Each set of P-V loops in Figure 2.7 was generated with a constant C_s value while preload varied over a range of initial volumes. ESPVR$_1$ (from panel B) is overlaid in all panels to demonstrate trends with changing C_s. Unlike the alterations in R_s, the changes in C_s created more noticeable differences in slope for the ESPVR line. In addition, the volume intercept was altered more markedly (Table 2.4). The changes in E_{ves} were significant; however, the actual percent change for all panels was approximately 8% or less. With V_o, the differences were approximately 2.5 ml or less for both cases. Even with the significant changes in E_{ves} and differences in V_o under the influence of varying C_s, Figure 2.7 reveals that the PV loops for all values of C_s have an end-systolic pressure point (the approximate upper left corner of the loop) that lies close to the ESPVR$_1$ line in the normal physiologic range (50-80 ml end-systolic volume). Larger deviations from the standard ESPVR occur at lower C_s values. As C_s changes with preload held constant (Figure 2.8C), increases in E_{ves} are larger (> 145%), and the intercept shifts to the right by $\approx$ 40 ml (Table 2.4). Another evident phenomenon isthe skewing of the P-V loops up and to the left with lower C_s. This would indicate that a system with lower C_s (a stiffer system) would have higher pressure in late systole with a more rapid decay of the pressure during diastole. The AOP plot in Figure 2.8 confirms both

of these characteristics. Differences in overall volume flow are apparent (though not as pronounced as with R_s increases) in both the AOF plot and the P-V loops of Figure 2.8.

PV loops with constant C_s and varying preload
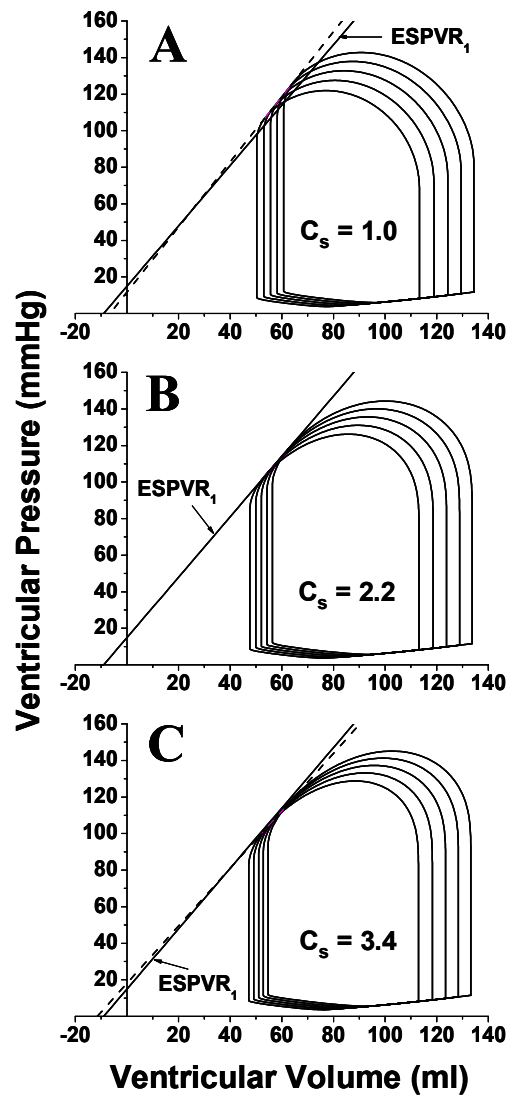
Figure 2.7 P-V Loops with Constant C_s and Varying Preload. P-V loops were generated as C_s was held constant at one of three values (1.0, 2.2 or 3.4 ml $mmHg^{-1}$), and preload was varied over the range 8-12 mmHg. The average cycle values with standard error for mean AOP (mmHg), SV (ml) and EF, respectively, are: for part A (89.30 ± 6.04, 68.53 ± 4.23, 0.55 ± 0.004), for part B (93.90 ± 5.35, 71.57 ± 4.68, 0.58 ± 0), for part C (95.07 ± 4.60, 72.26 ± 5.06, 0.59 ± 0.005). The standard $ESPVR_1$ line (solid) is shown in all three panels as reference for the ESPVR line (dashed) calculated using each set of simulation data.

39

Waveforms with varying C_s
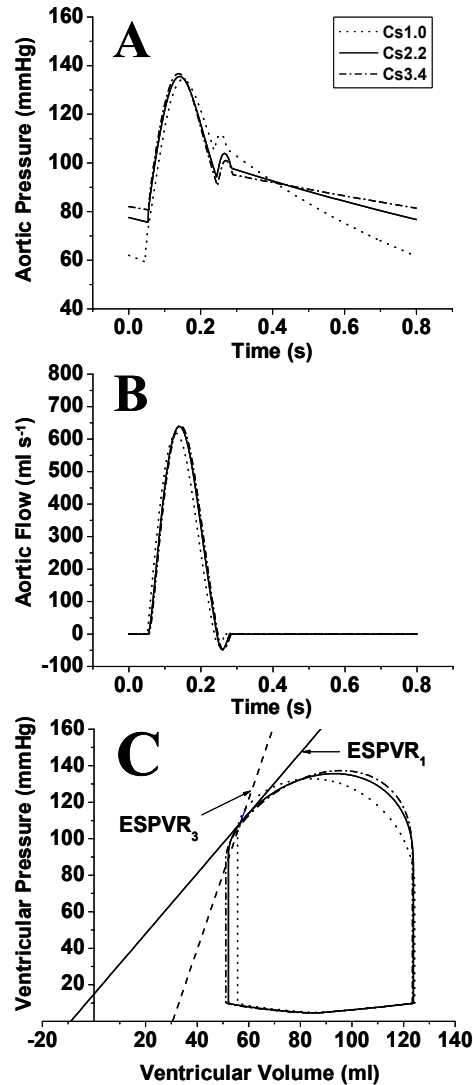
Figure 2.8 Waveforms with Varying C_s. Steady-state cardiac cycle waveforms were generated at three different values of C_s (1.0, 2.2, and 3.4 ml mmHg^{-1}). The cycle values for AOP (mmHg), SV (ml) and EF, respectively, are: for C_s = 1.0 (89.44, 68.66, 0.55), for C_s = 2.2 (94.02, 71.70, 0.58), for C_s = 3.4 (95.16, 72.40, 0.59). The standard ESPVR$_1$ line (solid) is shown panel C as reference for the ESPVR$_3$ line (dashed) calculated using each set of simulation data.

In addition to the trends seen in the P-V loops, our model captures other features of the cardiovascular waveforms. For example, the AOP and AOF plots in Figures 2.6 and 2.8 illustrate the model's ability to portray several of the main waveform features (e.g. the

dicrotic notch and negative flow). Figure 2.2 reveals that the timing and cyclical nature of

ventricular ejection and refilling is appropriate. The MAOP, SV and EF values provided in

the figure captions demonstrate that changes in afterload parameters alter the ventricular

output in predictable ways. For example, higher R_s results in an elevated MAOP, and lower

SV and EF. In the venous portion of the circuit, the pressure waveforms vary slowly (1-2

mmHg per cycle) and the venous volume acts as a reservoir for refilling the atrium. Total

volume is conserved within the circuit to within less than 0.1 ml. difference per ten cycles

(i.e. a 0.002% volume change over ten cycles). The coronary flow waveform has a rapid

increase as inflow occurs and a rapid decline as the coronary flow contributes to the atrial

volume. This aspect of the flow is not indicative of a typical coronary flow pattern, and is

due to the simple RC configuration. Nevertheless, the overall volume transfer per cycle was

approximately 2-3 ml., which lies in a physiologic range when scaled for larger hearts.[74]

Discussion

Demonstration of Model Concurrence

Open-loop Configuration (Figures 2.3 & 2.4)

The simulations generated with the open-loop impedances (Figures 2.3 & 2.4),

demonstrate the model's ability to derive realistic aortic pressure/flow outputs from

corresponding inputs with any of the four afterload arrangements. For the simulation in

Figure 2.3, we did not have the exact data points or initial conditions from the published

waveforms. Nevertheless, the model's output using the 4-E Alt. afterload arrangement

actually matches well with the waveforms published by Stergiopulos. The AOP input with

AOF output was added in our simulation to illustrate both input/output scenarios and to

41

further validate the proper functioning of the model. In Figure 2.4, the 2-E model has a large amount of noise associated with its output. This is due to the crude nature of the arterial representation that imparts difficulties when trying to represent the medium and high frequency ranges. Even though the input pressure signal contains some noise artifact, the 3-E and two 4-E portions of the model are still capable of producing an AOF with reasonable magnitude, shape and timing. The aspect of negative flow is also produced in response to the pressure downswing and dicrotic notch.

A comparison of the results, given in Table 2.1, from each 4-E model illustrates that systemic compliance was higher and Z_o and I_s lower for the 4-E model with the series arrangement of Z_o and I_s. Similarly, to achieve a realistic aortic waveform output in Figure 2.4, our 3-E and 4-E models required a higher value of C_s and an equal or lower value of Z_o in relation to the 4-E Alt. model. The trend for 3-E models to overestimate compliance and underestimate Z_o was noted by Stergiopulos *et al.*[60] At lower input frequencies, the characteristic impedance adds to the overall impedance and plays a smaller role, but at higher frequencies Z_o plays the prevailing role because the systemic compliance dominates the parallel R_s and C_s combination and drives its contribution to zero. Stergiopulos contends that, at lower frequencies when the blood mass is "accelerated simultaneously", the contribution of inertance is much greater than at higher frequencies. In addition, it is noted that the series arrangement allows the I_s term to raise the impedance moduli at all frequencies (except 0 Hz). This addition of impedance at all frequencies (as in the series arrangement) would likely not tend to alleviate the problem of C_s overestimation and Z_o underestimation as seen with the 3-E model. Alternatively, the parallel arrangement of Z_o and I_s allows both elements to make their largest contributions in the appropriate frequency ranges. As

demonstrated by numerous modelers, both types of four-element models can effectively portray arterial impedance characteristics. Nevertheless, when waveforms with significant higher frequency contributions are used, the 4-E Alt. model may follow a more realistic impedance and phase spectrum at these higher frequencies (leveling off at Z_o) instead of tending to high values of impedance as in the 4-E model. Though the parallel arrangement does provide advantages in producing impedance and phase moduli that more closely match physiological data, it does not have the ability of being directly reduced to a 3-E afterload configuration (setting I_s to 0 effectively eliminates both I_s and Z_o). Furthermore, nodal analysis of the 4-E Alt. model produced equations that were much less stable. For these reasons, we chose not to implement this configuration in the closed-loop arterial impedance model.

Closed-loop Configuration (Figures 2.5 – 2.8)

   P-V loops and aortic waveforms generated by the left heart portion of the model mirror several trends seen in physiological data. Figures 2.5 and 2.7 along with Table 2.4 indicate that only minor changes occur in the ESPVR slope when preload is incrementally increased at different values of R_s and C_s. However, the divergence in E_{ves} was statistically significant for changes in C_s. Variations in V_o were observed for all afterload changes, showing a trend of decreasing V_o with increasing R_s and with increasing C_s. Experiments employing excised canine hearts have demonstrated no significant changes in E_{ves} with regard to changes in resistance and compliance of the systemic circulation.[38, 75] The same studies showed that V_o did shift to the left with increasing R_s, but there was no significant change in V_o with alterations in compliance. Other researchers have compared P-V loops generated with a

constant preload and varying R_s or C_s. Their findings indicated a significantly increased ESPVR slope when either peripheral resistance or compliance was increased,[66, 67] and the increase in slope was higher for rises in compliance than for elevation of peripheral resistance.[67] An illustration of model results (Figures 2.6C, 2.8C and the values reported in Table 2.4) confirms a significant increase in slope with constant preload and alterations in R_s and C_s. In addition, the rise in slope is greater for changes in compliance than for variations in peripheral resistance. Thus, our model confirms the reported physiological response to these changes.

Our model differs somewhat from the physiological data presented in such studies as Maughan *et al.* [38] by showing a significant change in E_{ves} and V_o with changing afterload (Figures 2.5, 2.7 and Table 2.4). Though significant, the percent changes for E_{ves} and magnitude changes for V_o are relatively small when compared to changes for constant preload and varying afterload (Figures 2.6C, 2.8C and Table 2.4). Several factors likely contribute to this behavior of the model. One factor is the type of statistical test used in analyzing our model's results. In the aforementioned physiological studies, there was the possibility of variation among the canine hearts themselves, even with identical preload and afterload conditions. Therefore, the investigators used a two-way analysis of variance and showed no significant changes in E_{ves}, even though the actual change in slope they obtained was greater in magnitude than what our model produced. With the mathematical model, there is no variation in the heart source, thus, the small-sample t-test was employed to test the slopes and intercepts. This test allows a narrower range of variation, and thus, it indicated significant changes in E_{ves}. The V_o changes in our model may be due, in part, to the lower values of slope produced by the model as compared to those seen in previous studies with

44

animals and humans. A lower slope would cause any difference in the slope to be distributed over a larger range of intercepts. This, along with the added sensitivity of our statistical test, would tend to produce significantly different results for V_o. Another aspect that might alter the trends of E_{ves} and V_o is the use of mixed parameter values in the ventricular and afterload portion of the model. For example, several of the ventricular parameters are based on canine studies; however, the typical afterload values used are more closely associated with humans. This perspective is discussed in detail in Model Deficiencies.

The aortic waveforms generated by the model show definite changes as R_s is increased. Figure 2.6A reveals a trend of elevation in MAOP with a rise in R_s. Since resistance is proportional to aortic pressure, it follows that systemic resistance is inversely proportional to aortic flow. Such an inverse proportionality implies that as R_s is elevated, aortic flow should fall, and this is indeed the result shown in the SV and EF numbers for Figure 2.6B. When compliance is decreased during simulation, MAOP magnitude decreases while the range of aortic pressure actually increases (Figure 2.8A). This response is again related to the proportionality of AOP and the systemic impedance. The impedance of a compliance element is expressed as $-j\omega^{-1}C^{-1}$; therefore, a lower compliance will result in higher impedance and a higher peak pressure. Since this impedance is frequency dependent, a lower compliance value would also allow more rapid filling and decay with pressure increases (maintaining a higher value during systole). Thus, the higher values of compliance result in an aortic pressure that changes less rapidly and maintains a higher mean value. Following similar arguments as with systemic resistance, the SV and EF would be reduced with a lower C_s, and Figure 2.8B agrees with this expectation. Very few direct comparisons of AOP waveforms under the influence of isolated changes in afterload parameters can be found in

the literature. Nevertheless, Elzinga and Westerhof were able to construct a mechanical afterload whereby they imposed changes on the individual components of the afterload with an isolated feline heart.[35] As R_s increased, they reported a higher systolic and diastolic aortic pressure and a corresponding lower peak aortic flow and stroke volume. With a reduction in C_s they observed a higher peak AOP during systole and a lower diastolic AOP with a slightly lower peak AOF and SV. Their results agree remarkably well with the output of our model (Figure 2.6 (A and B) clearly illustrate that AOP is elevated and AOF reduced with increasing R_s). Furthermore, Figure 2.8 (A and B) reveal a higher systolic and lower diastolic AOP with a reduction in AOF as C_s is reduced. It is also possible to verify the aortic waveform output of the model from another perspective. Since AOP closely follows ventricular pressure during systole and AOF is simply the ventricular volume change during systole, the P-V loops generated under isolated changes in afterload parameters provide an indication of alterations in AOP and AOF with changes in R_s and C_s. Previous studies show that elevations in R_s produce higher ventricular pressure and less SV.[13, 37, 38, 66, 67] These changes imply a higher AOP and lower AOF as the model demonstrates in Figure 2.6 (A and B). The same studies illustrate that reductions in systemic compliance result in a higher peak AOP later in systole with slight reductions in SV,[13, 37, 38, 67] and Figure 2.8 (A and B) demonstrate a similar outcome from the model.

The model incorporates afterload and volume values that are similar to those reported in the literature.[19, 54] Values for MAOP, SV and EF generated by the model also fall well within the physiologic range (Figures 2.5-2.8).[54] The afterload parameter values used for R_{vn} and C_{vn} are somewhat elevated in relation to systemic arterial resistance and compliance. Nevertheless, the ratios of C_s to C_{vn} and R_s to R_{vn} are not unreasonable when compared to

similar models.[19, 21, 56, 57, 76-78] The lumping of numerous circulatory elements on the venous and pulmonary side of the circulatory path is certainly a contributing factor to the higher values of R_{vn} and C_{vn}.

Model Deficiencies

Open-loop Configuration

Though there are a number of ways in which the model accurately portrays physiological trends, as with most models of a complex system, the model's output differs from data produced in animal studies in several areas. The open-loop portion is certainly unrealistic in its depiction of the arterial system as an isolated impedance that has no volume conservation and no mechanism for feedback to its input source. In the open-loop configuration, the model receives an actual aortic pressure or aortic flow waveform as input. However, the model is, at most, second order, and does not account for such phenomena as wave propagation/reflection. Thus, the model fails to capture some of the details in its output waveforms. Most of the waveforms also have few if any associated afterload parameters, which adds to the divergence of the model output from the true waveform. Employing a higher order model and accounting for afterload and wave reflection parameters would greatly improve the accuracy of the model; however, the accuracy would only be improved for a single waveform from a single animal. As was previously discussed, the variation in afterload parameters, even within species, can be quite large, and adding these levels of complexity would be cumbersome in the generation and operation of the model. In addition, increased complexity would add little to the understanding of the overall trends for changes in the major afterload parameters.

Closed-loop Configuration

Waveform Characteristics and ESPVR Trends

In the closed-loop left heart configuration of the model, the basic features of the waveforms are preserved; however, certain details of the waveforms and characteristics of the P-V loops are lacking. Without having actual aortic pressure/flow waveforms as inputs, the particular characteristics of a ventricle and afterload combination must be generalized. Adding complexity to the ventricular model would serve to capture many details that are missing, but again this addition would compromise the model's ability to instruct on a more fundamental level.

The model has demonstrated the ability to capture several typical behaviors seen in P-V loops generated in animal studies [38, 66, 67, 79] such as predictable changes in ESPVR slope with variations in preload and afterload parameters. Nevertheless, in these same studies, certain trends were not reproduced by the model. For example, in experiments, the slope of the ESPVR lines was typically in a range from 2 to 7 mmHg ml^{-1} with a V_o from 0 to 20 ml. In our simulations, the model generated slopes from 1.55 to 1.75 mmHg ml^{-1} with typical V_o less than 0 ml. Investigators have noted that variations in P-V loops and associated ESPVR lines could occur due to variations in the species under investigation and the method of preparation of the heart (excised or closed-chest).[12] Other investigators have actually reported such outcomes as negative values for V_o. [79, 80] Though variations in P-V diagram characteristics can and will occur across species and with different preparations, these factors likely do not account for all the variation seen by our model. One potential factor contributing to divergence in the model's results is that many of the ventricular model parameters were obtained from experiments on canines;[58, 59] however, the ventricle described

48

by these parameters is then coupled to an afterload with parameter values more closely related to man.[11, 60] Though the overall trends should be preserved by this approach, the exact range of values may be somewhat different. Another major issue that is not addressed in the simulation results is the isolated nature of the afterload changes and the lack of change in contractility during simulations. Isolating changes in specific afterload parameters using a computer controlled artificial afterload may be possible, but in reality changes would never occur in isolation within the circulatory system. This fact makes it difficult to state that a particular change in an afterload parameter will create a given change in output waveform within the circulatory system itself. A more accurate statement is that a given condition (state) of the circulatory system is typically characterized by a directional change in value for a specific component of the afterload. This is illustrated by studies that show a higher value for R_s in subjects with heart failure,[42] whereby the system attempts to elevate aortic/arterial pressure to compensate for the lessened strength of the heart.[54] Other studies on R_s during exercise reveal that peripheral resistance drops during exercise;[44] however, the aortic pressure actually increases due to compensatory mechanisms such as increases in heart rate and contractility.

Simplified Coronary Circulation

   Another factor affecting contractility and ESPVR changes is the simple RC analog used for the venous/pulmonary path and the coronary circulation. As discussed previously, the highly simplified RC arrangement for the venous and pulmonary paths lends a higher ratio of venous to systemic resistance and compliance. The alteration in venous resistance and compliance influences the filling of the atrium and ventricle which would affect preload and

49

contractility. Though this was not apparent in our simulations over the heart rate range of

50-120 b.p.m, the refilling of the ventricle could be compromised at higher heart rates.

Regarding the coronary RC analog, our simulator was not an attempt to model the coronary

pressure and flow, and the single-branch RC model simply acts as a placeholder for a more

rigorous analog of the coronary impedance. Nevertheless, the antiphasic nature between the

left ventricular pressure and the left heart coronary flow is preserved, and the volume

entering and exiting the coronary circulation per cycle is in a physiologic range. In order for

the coronary adjunct of the model to be more effective, it must be coupled properly to the

ventricular pressure source. This would involve not only relating the coronary pressure/flow

to the aortic pressure as a function of arterial bed alterations, but also altering the coronary

contribution based on left ventricular loading.[15, 81] The coronary flow per cycle must then act

as a partial determinant of ventricular contractility. To our knowledge, the relationships

necessary to carry out this coronary/ventricular coupling have not been determined for this

ventricular model.[58, 82] This is an area that must be addressed for a more complete

description of the ventricular/afterload interactions, but it was not our purpose to make

modifications on the basic equations describing the ventricular source. Though in its present

form the ventricular description does not couple contractility with coronary flow, it does

allow for some alterations in contractility (through the parameter "c" in Table 2.2). Future

work may involve a relation of this parameter to the blood supply from the coronary

circulation.

Additional Considerations

Changes in the model could be undertaken in the areas of baroreflex-feedback control mechanisms and wave reflections in the major arteries. Ursino *et al.* developed a pulsating heart model of the carotid baroreflex that attempts to integrate numerous responses initiated by this feedback mechanism. The gain of the baroreflex response is altered based on the frequency of the change in carotid pressure.[19, 20] The nonlinear elements of feedback response have been modeled by others.[83-87] Each of these models employs a variable elastance model of the ventricle. One drawback to our use of the mathematical description of the ventricle given by Ottesen *et al.* is that, in its current state, the parameters of the model do not provide an avenue for baroreflex-feedback control.[82, 84] The time domain description of the ventricular pressure and the simplistic lumped impedance also render it difficult to account for wave propagation/reflection.[50] Both of these aspects must be accounted for if the model is to serve as a more comprehensive illustrator of circulatory behavior.

In light of the complex adjustments that go on in the circulatory system and the lack of compensatory mechanisms employed in our model with isolated changes, some differences between our model results and physiological data are not surprising. For example, in generating P-V loops with constant afterload and varying preload, canine hearts used in experiments would have experienced changes in contractility according to the Frank-Starling law of the heart and the coupling of ventricular contractility with preload. These changes in contractility were not accounted for in our simulations. Studies by Grossman *et al.*, Suga and Sagawa, demonstrate the increase in slope and V_o that occurs with an increase in contractility.[14, 79] Inclusion of such relevant factors would help realign the numbers for ESPVR slope and intercept, having a more reasonable range.

Despite the fact that the model lacks certain intricacies present in physiological systems the basic waveform features generated and the overall tendencies elucidated for afterload changes are within an acceptable range for simple modeling of the left heart and systemic circulation. The model is not overly sensitive to isolated afterload changes within the range of typical physiologic systems (Figures 2.5-2.8), and a number of parameters can be adjusted to alter the pressure/flow dynamics. Therefore, assembling combinations of afterload and ventricular parameter changes to mimic some altered state of the physiological system and observe accurate trends in all output waveforms is possible.

Model Comparisons and Contributions

In the ever-expanding area of computer modeling, it seems necessary to make a brief comparison between the model we propose and the models of others currently available. Olansen *et al.* [21] developed a model (based on their previous work with Chung *et al.* [22]) that includes a heart model based on time-varying ventricular elastance incorporating ventricular interaction through the septum and a time-varying elastance description of the atria. In addition, the model includes pericardial pressure relationships, a closed-loop circulatory path that includes systemic and pulmonary circulation, and a parameter estimation routine for optimizing afterload parameters based on input data. The model we developed differs from that of Olansen in several ways. Their model allows users to enter known data and then performs parameter optimization according to that dataset. The user can then modify parameter values to mimic some typical or altered circulatory state. Our model allows arbitrary waveform inputs to the open-loop portion, in which the user can vary impedance values. The closed-loop portion of our model does not allow arbitrary waveform inputs due

to the ventricular source properties. In our model we do not, at present, offer a parameter optimization routine. The mathematical description of the ventricle in our model is more rigid in that it does not permit large alterations in parameter values for achieving reasonably shaped waveforms and the model does not support right/left ventricular interactions. Therefore, our model offers starting impedance values that the user can adjust within practical limits. Though more rigid, the ventricular model we use does have some advantages in providing a volume-dependent time-varying description of ventricular pressure that takes into account changes in ventricular elastance during ejection, isovolumic pressure changes and heart rate changes (for a more complete description of the ventricular model properties see [53, 58, 82]). Neither our model nor Olansen's adequately accounts for coronary circulation or wave reflections. Nevertheless, the model by Olansen *et al*. has been further expanded by Lu *et al*. to include cardiopulmonary interactions and cerebral flow.[88] This type of expansion with the ventricular source we employ has yet to be done, but we do provide a placeholder within our circuit for a satisfactory coronary addition. Furthermore, the LabVIEW[TM] software we used in development enables extension of our model in areas such as parameter fitting, spectral analysis and additional circulatory pathways by inclusion of the appropriate functions (subVIs).

Another model that is similar to ours is the instructional model published by Davis and Gore.[23] This model is effective as a basic teaching tool. The layout is simple to use and an executable version is available as a web link. Davis and Gore's model enables the user to alter a lumped afterload, heart rate, contractility, preload and other main determinants of ventricular function, while viewing aortic and ventricular pressure along with P-V loops. The Davis/Gore model lacks more detailed waveforms for ventricular pressure, volume, and

elastance, as well as aortic pressure and flow. Our model produces these waveforms from a ventricular input in a closed-loop manner. We have included a coronary and venous portion to the feedback along with an afterload of up to 8 lumped parameters (including venous and coronary impedance values). All the afterload elements are individually adjustable (as opposed to adjustment of one lumped value in the Davis/Gore model). A unique description of the ventricular source is employed in our model that accounts for the ejection effect (described by Danielsen and Ottesen [52, 58]) and accommodates changes in contractility and heart rate. In addition, adjustments in preload and venous pressure are available in our model, and several important waveforms can be captured and cataloged to data files. The dicrotic notch from the aortic reverse flow does not appear in the waveforms published by Davis and Gore. In our model, this is actually determined by interactions between the various parts of our closed-loop (a balance between ventricular pressure, aortic pressure, and coronary pressure). In the open-loop portion, we provide realistic aortic waveforms and frequency plots of magnitude and phase for the different afterloads. We have also provided the equations for both open- and closed-loop models along with the electrical analogs on which these equations are based. Our model currently lacks a classroom or laboratory teaching module, but an executable version and a full code version are available online at http://www.unc.edu/~rcole/SAVIAv1/SAVIAv1_O_A_Form.htm through a no-cost end-user license agreement drafted by the University of North Carolina at Chapel Hill.

Other models are available with varying degrees of detail, ease of use, and accessibility.[89, 90] While our model is not all-encompassing in its inclusion of circulatory parameters, it does contain many basic constituents of the cardiovascular system that are necessary in modeling overall circulatory performance. Also, by the addition of the closed-loop coronary portions,

the model is a step forward in expanding the use of the mathematical description of the ventricle promoted by Ottesen *et al.*[58, 82] Our specific use for the model did not necessitate parameter fitting, neural feedback or certain other factors; therefore, the model was not developed with these dynamics. There are educational uses in introductory studies of hemodynamics. Moreover, there are uses for our model in such areas as estimation and cataloging of limitations and trends with changing impedance parameters. This would be useful in guiding future studies with a live heart setup (e.g. Langendorff) or other experiments that benefit from an open-loop approach. Making the aforementioned additions of a more realistic coronary circuit and an acceptable neural feedback, along with a feature for parameter estimation, would greatly enhance the model's capabilities and render this particular representation of the ventricular source a widely applicable tool for modeling.

Conclusion

   While it is certainly true that the intricate nature of the systemic circulation belies the thoughts of a simplistic model, that such an approach is sufficient on a more basic level has been demonstrated repeatedly. We believe that our lumped-parameter model, fashioned on the groundwork of Frank's windkessel-type systemic afterload and the ventricular pressure source (adapted from Ottesen and Danielsen *et al.*), has demonstrated the ability to capture the salient features of the cardiovascular waveforms and follow physiologic trends in these waveforms under the influence of changing afterload. Therefore, the model possesses the properties of simplicity and sufficient accuracy in portraying the cardiovascular hemodynamics. These assets establish the model as an instructive tool for students of the heart and circulatory system as well as an aid in experimental research. For purposes of

testing the proposed fluid-mechanical dynamic afterload, this model is more than sufficient to reveal trends in AOP with impedance changes and to provide a method for testing possible open-loop models of the dynamic afterload system.

Acknowledgements

CHAPTER III

A GENERAL SOFTWARE PROGRAM FOR ACQUISITION AND ANALYSIS OF SIGNALS (PAAS)[2]

Background

A clinical research faculty member had previously identified a need for a comprehensive analog signal acquisition and power spectral processing program, and our need was to develop a software system for data collection and cross-channel investigation to be used in system analysis. Preliminary work [91] demonstrated the scientific value of the spectral information from the electrocardiogram collected during ventricular fibrillation (VF) in the heart. Collectively, the team suggested several innovative ways to analyze this spectral data, but the original data processing and display system lacked the required features and capabilities necessary to interrogate the data with those objectives in mind. Thus, the basic research and engineering faculty joined with the clinician and defined the scope of the project which included a comprehensive and flexible state-of-the-art data acquisition platform, a multifunctional data selection and analysis capability, data display features that included the most common power spectral analysis tools and, finally, simple software tools to permit verification of system performance and accuracy while allowing users to generate simple test signal constructs and explore processing outcomes using those known inputs. For our purposes, this software program would serve as a tool for system analysis of the dynamic

afterload we would construct. The program employs cross-channel frequency analyses using averaging methods to achieve noise reduction (discussed subsequently). These methods make the program an ideal platform on which to test the behavior of the dynamic afterload.

The program we developed (**PAASv1**, **P**rogram for **A**cquisition and **A**nalysis of **S**ignals **V**ersion **1**) features real-time signal acquisition, along with analysis and test signal generation written in LabVIEW[TM] (LV) for use with National Instruments[TM] (NI) hardware. Our intent was to duplicate and upgrade the capabilities of our existing collection and analysis software while generalizing the routines and expanding its capabilities to include additional time- and frequency-domain analyses. Separate panels for each feature of the new program allow the different aspects of the program to be operated independently. In its final form, the program has four panels: a data acquisition panel, two signal selection and analysis panels and a signal generation and data conversion panel. A description of the program follows, and an executable version of this program, along with a simple *User Manual*, is available from the authors using the electronic contact information provided through a no-cost end-user license agreement drafted by The University of North Carolina at Chapel Hill.

Introduction

Correlation and spectral analysis methods are powerful tools for investigation of linear systems, as well as signals used to characterize their behavior. Averaging segmented records of stationary waveforms is effective for reducing noise in both the time and frequency domains and providing indices of relationships (e.g. correlation and coherence functions) between signals. While many of these procedures have their theoretical origin in the continuous domain, contemporary signal processing is applied in the digital realm.

We present general algorithms for correlation and spectral analysis and derive discrete applications which we test in MATLAB® (ML) and implement in LV, using the programming language G. ML provides a way to rapidly prototype the algorithms and test their effectiveness. LV was chosen as a fast, widely available, and versatile tool for both interfacing digital-to-analog conversion hardware (DAC) and expressing discrete algorithms for real-time or off-line processing. The application which we present is an off-line processing tool to evaluate interactions between signals before committing the effort of real-time software development for a specific application.

Our description of PAASv1 relates mainly to the presentation and development of the discrete algorithm expressions, and verification of their correct software implementation through the application of appropriate test signals with known results. PAASv1 has two fundamental modes of use. The first mode is for collection of signals and analysis of the correlation or spectral properties of one or more signals sampled from the analog world. Of particular interest is the interaction between signal pairs, especially when these represent the input and output of a system. The second mode is devoted to generation of test signals, both sinusoidal and random, to verify the integrity of the software implementation of the algorithms. We have additionally found that this mode is useful to test the performance of various random signals.

The equal variance (EV) algorithms we present are practical for analysis of stationary signals and noise sources in both time and frequency domains. This software system is a convenient and versatile tool for: (a) estimating the correlation or spectral content of signals, (b) investigating the interaction between signals, such as in system identification and, (c) as a teaching and learning tool for the student of signal processing. The pragmatic discrete

expression of general continuous-time equations for correlation and spectral analysis are fully presented.

System and Program Description

PAASv1 runs on a Windows PC environment. We employ data acquisition (DAQ) hardware from National Instruments^{TM} (NI) integrated with the NI software LV. The instruments and software are used for data sampling, processing and archiving.

Data Collection

A diagram depicting the setup for data collection and data file storage is shown in Figure 3.1 (Panel A), and an illustration of the data collection front panel is shown in Figure 3.2. Electrical data is collected via NI DAQ hardware. LV software is used to sample the signal and write out the data to a file in 16-bit binary format. A time stamp and event markers, generated within the collection loop, are written out as separate files. Within the LV collection routine, the user can choose the number of channels, voltage range and A/D conversion bits for resolution depending on the NI compatible hardware selected. Collection files for data, time stamp and event markers are named according to the date and time of collection. A window on the collection panel informs the user about initial volume space and the size of the data file currently being written. When collection occurs on multiple channels, the user can choose to view up to three of these channels simultaneously on the front panel in a strip chart format. Data collection can be paused and resumed without generating any new collection files.

Flow Chart for Operation of the Program

A. Data Collection	B. Data Analysis	C. Data Generator
Electrical Signal ⬇ **NI DAQ Hardware** ⬇ **LV Collection Panel** **Sample signal(s)** **Generate time stamp** **Set event markers** ⬇ ⬇ **Data file** **Time file** **16-bit** **32-bit** **binary** **single** ⬇ **Events file** **32-bit** **single**	**LV Analysis Panel 1** **Select time segment** ⬇ **Retrieve data portion** ⬇ **Plot 1-min. segment** ⬇ **Cursor-select data region** ⬇ **Select analyses types** ⬇ **Write out analyses** ⬍ **LV Analysis Panel 2** **View analyses graphs**	**LV Test Data Panel** **Select sample rate** ⬇ **Select signal ampl.** ⬇ **Select signal phases** ⬇ **Generate test data and write to file**

Figure 3.1 Flow Chart for Operation of the Program. PAAS has three main features that operate independently: data collection (Panel A), data analysis (Panel B), and test data generation (Panel C). These features operate from separate panel displays within the same program. NI data acquisition hardware (NI DAQ Hardware) is required for data collection. Due to the number of graphical analyses available, users must toggle between two LV analyses panels to see the full results (Panel B).

LV Data Collection Panel
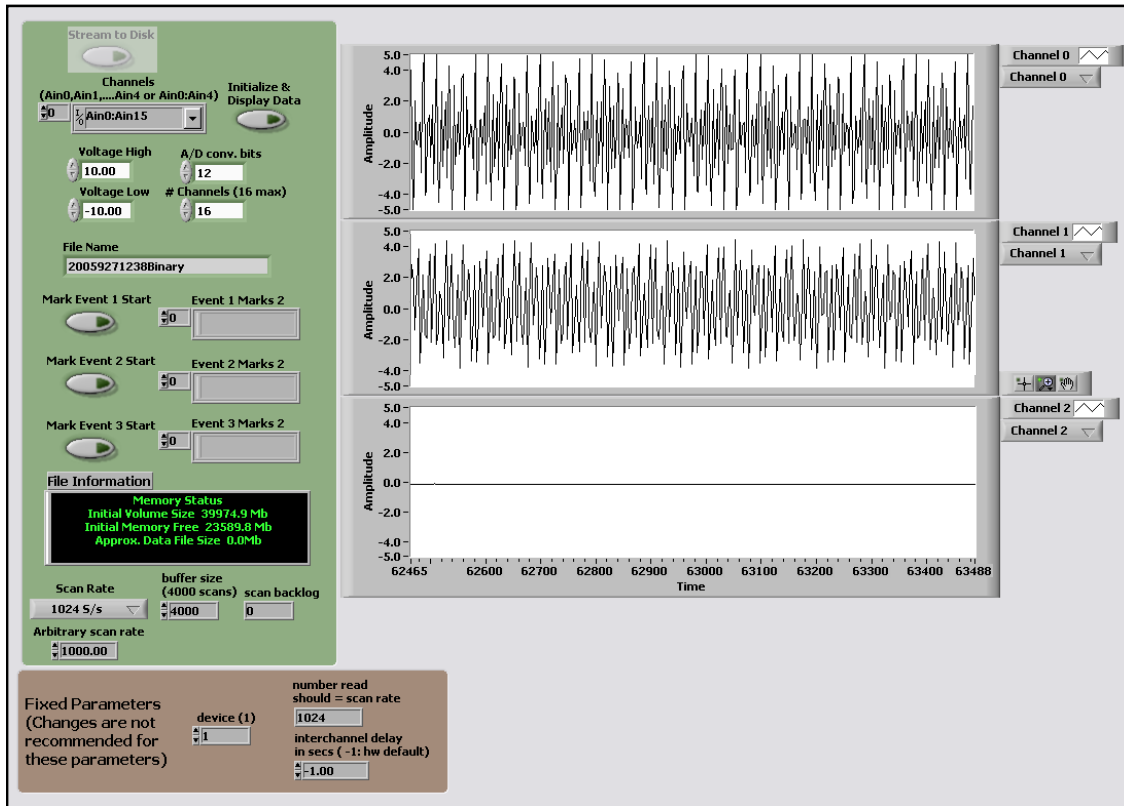
Figure 3.2 LV Data Collection Panel. Up to three waveform charts are employed for display of the data collected using NI DAQ hardware. User selectable signal acquisition parameters are shown on the left along with event markers.

Data Analysis

The data analysis portion of the program is diagrammatically represented in Figure 3.1 (Panel B). There are two main panels for data analysis (Figures 3.3 and 3.4). In analysis Panel 1, the user selects a certain portion of the data to read in. A limit is placed on the amount of data that can be brought in at any one time (this is necessary to avoid overtaxing the system RAM for large data files). The incoming data is graphed in one-minute segments, and a chosen (possibly smaller) segment of this data is graphed on a separate plot for selection of an analysis region. Moveable cursors are employed to define the data to be

analyzed, and the user can choose different analysis types and various cross-channel comparisons. Graphical and tabular results from these analyses can be written out to a spreadsheet file. The user can toggle between analysis Panel 1 and analysis Panel 2 in order to view correlation, spectral and coherence analyses results. In analysis Panel 2, auto- and cross-correlation, auto- and cross-spectra and coherence analyses are presented in separate plots. The user may choose to view any or all of the single-channel or cross-analyses pairs on the graphs simultaneously.

LV Data Analysis Panel 1
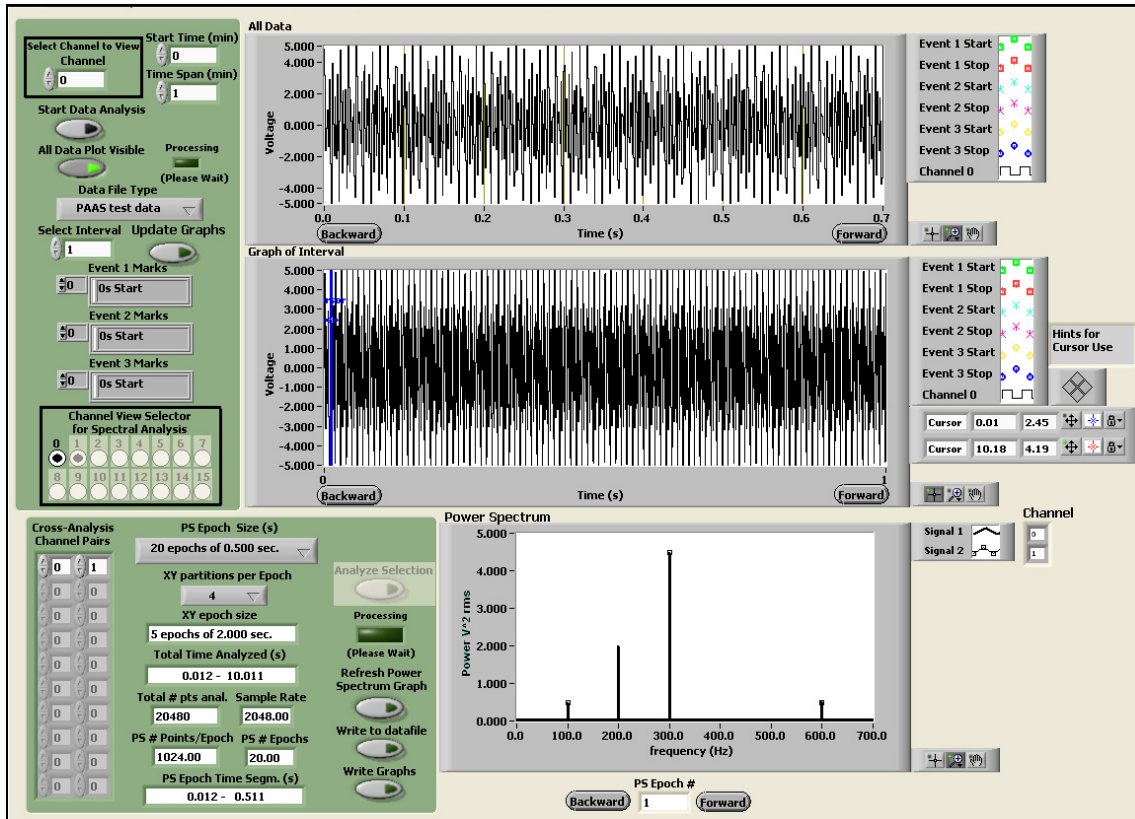
Figure 3.3 LV Data Analysis Panel 1. All channels of the data file are read in on this panel and can be displayed, one channel at a time, in the upper graph. Data in the upper graph is decimated (every other point in the display only) to reduce memory requirements. The middle graph displays a portion of the full, undecimated data and allows cursor selection of an analysis region. Controls for customizing analysis display, for cross-analysis choices, and for time epoch selections appear on the left.

LV Data Analysis Panel 2
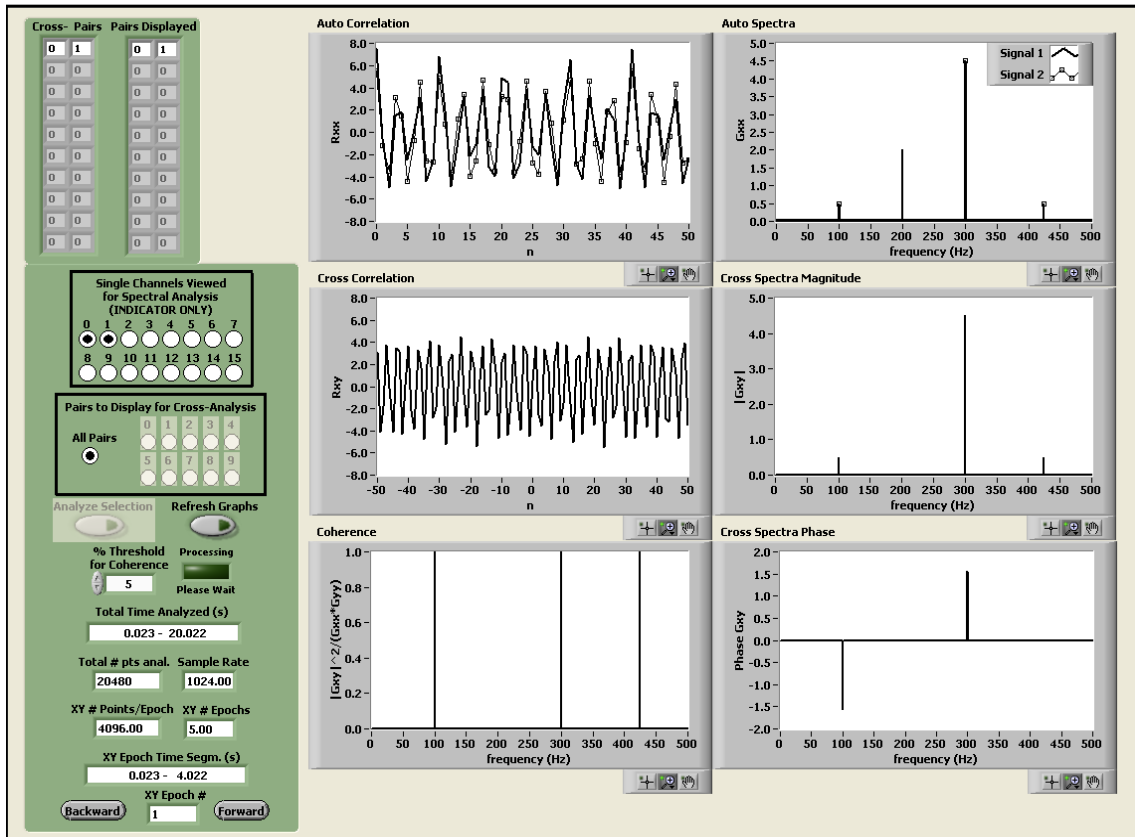
Figure 3.4 LV Data Analysis Panel 2. Additional analysis graphs are presented on the second analysis panel. These include auto- and cross-correlation (upper and middle plots on left), auto- and cross-spectra (plots on right), and coherence (lower plot on left). Controls and information regarding channel views, cross-analysis pairs and time epoch selections are displayed on the left.

Test Data Generation

A fourth panel in the program was designed for the generation of user-defined test data (diagrammatically presented in Figure 3.1 Panel C and Figure 3.5). A one minute segment for two signals may be generated and placed in an external data file. Each signal is formed by the summation of as many as four sinusoids having known amplitudes, frequencies, phases and sample rates. Once generated, the signals are written to a data file. That file, in

turn, can be reloaded using the signal analysis panels and processed as though it were source data collected from the NI DAQ hardware. The data generator panel also enables conversion of text-formatted data files into a suitable binary format for import into the data analysis panels, thereby allowing a wider range of signal sources to be analyzed.

LV Data Generation Panel

This segment of the program will generate a one minute interval of test data. Each test data signal is the sum of 4 sinusoids of varying amplitudes, frequencies, and phases along with a noise component. The two signals will be saved to a designated folder with two associated files (necessary for reading in for data analysis). Simply set the signal parameters, choose a sample rate, and press the <<Generate Test Data>> button. To properly access this data in the Data Analysis portion, select <<Yes>> in the dialog box when asked if this was LabVIEW generated test data.

Generate Test Data

Samples /s
1024 S/s

Signal Form

$$Signal_1 = a_{1,1}\sin(f_{1,1}2\pi nT + ph_{1,1}) + a_{1,2}\sin(f_{1,2}2\pi nT + ph_{1,2}) + a_{1,3}\sin(f_{1,3}2\pi nT + ph_{1,3}) + a_{1,4}\sin(f_{1,4}2\pi nT + ph_{1,4})$$

Signal 1

| amplitude 1,1 | freq (Hz) 1,1 | phase (deg) 1,1 |
| 1.00 | 100.00 | 0.00 |

| amplitude 1, 2 | freq (Hz) 1,2 | phase (deg) 1,2 |
| 2.00 | 200.00 | 0.00 |

| amplitude 1, 3 | freq (Hz) 1,3 | phase (deg) 1,3 |
| 3.00 | 300.00 | 0.00 |

| amplitude 1, 4 | freq (Hz) 1,4 | phase (deg) 1,4 |
| 1.00 | 600.00 | 0.00 |

Signal 2

| amplitude 2,1 | freq (Hz) 2,1 | phase (deg) 2,1 |
| 1.00 | 100.00 | -90.00 |

| amplitude 2,2 | freq (Hz) 2,2 | phase (deg) 2,2 |
| 0.00 | 200.00 | 0.00 |

| amplitude 2,3 | freq (Hz) 2,3 | phase (deg) 2,3 |
| 3.00 | 300.00 | 90.00 |

| amplitude 2,4 | freq (Hz) 2,4 | phase (deg) 2,4 |
| 1.00 | 600.00 | 0.00 |

Convert formatted ASCII file for read-in

This function converts a properly formatted ASCII file to enable read-in as 16-bit binary. The proper formatting for the ASCII file is as follows. The file must contain data only (no timestamp). The data must be tab-delimited, columnar and cannot exceed 16 columns. The sample rate used for data collection must be known.

Convert ASCII file

Figure 3.5 LV Data Generation Panel. In this panel, two alternate forms of data entry into the main analysis panels are provided. In one pathway, two separate data signals can be generated using a summation of known sine wave components that are subsequently sampled and saved for retrieval by the analysis panels. In the second pathway, ASCII formatted data collected from other sources can be imported for analysis.

Computational Methods and Theory

Overview

Standard correlation, spectral and coherence formulas that are based on continuous signals are excellent for theoretical development. However, these formulas are not practical for discrete computations using biological signals which must be digitally sampled. [92, 93] For many types of biomedical signal analyses, it is also important to partition the data into smaller time epochs. This allows progression of time-dependent phenomena to be more readily observed and formats the data for statistical weighting. We have programmed discrete implementations of these algorithms accordingly, to be suitable for sampled signal analysis. Our algorithmic implementation of these correlation and spectral formulas enable operation on partitioned data, provide unbiased estimates and give equal statistical weight to each data point.

Implementation of Digital Algorithms for Correlation, Spectra and Coherence

Continuous time formulas for unbiased auto- and cross-correlation (R_{xx}, R_{xy}) , one-sided auto- and cross-spectra (G_{xx}, G_{xy}) and coherence (γ_{xy}) estimates (^) are given by Bendat and Piersol. [93] These are shown in equations 1-5:

$$\hat{R}_{xx}(\tau) = \frac{1}{T-\tau} \int_0^{T-\tau} x(t)x(t+\tau)dt \qquad 0 \le t \le T \qquad\qquad 1$$

$$\hat{R}_{xy}(\tau) = \frac{1}{T-\tau} \int_0^{T-\tau} x(t)y(t+\tau)dt \qquad 0 \le t \le T \qquad\qquad 2$$

$$\hat{G}_{xx}(f) = \frac{2}{n_d T} \sum_{k=1}^{n_d} |X_k(f,T)|^2 \qquad\qquad 3$$

$$\hat{G}_{xy}(f) = \frac{2}{n_d T} \sum_{k=1}^{n_d} X_k^*(f,T) Y_k(f,T) \qquad\qquad 4$$

where $T_{total} = n_d T$ denotes a collection of sample records of period T and

X_k and Y_k denote the continuous time Fourier transform of x and y.

$$\hat{\gamma}_{xy}^2(f) = \frac{\left|\hat{G}_{xy}(f)\right|^2}{\hat{G}_{xx}(f)\hat{G}_{yy}(f)} \qquad\qquad 0 \leq \hat{\gamma}_{xy}^2 \leq 1 \qquad\qquad 5$$

Correlation Algorithm Implementation

When converted to algorithms for discrete time, an unbiased version of the auto- and cross-correlation functions may be derived from Bendat and Piersol [92] as shown in equations 6 and 7. The inclusion of only positive lag numbers (positive values for m) results in a correlation which contains only M points from 0 to M-1. We hereafter refer to this as a one-sided correlation. For a full correlation with both positive and negative lag values, the limits on m would run from $-$ (M-1) to +(M-1), providing 2M-1 points in the full correlation. This full correlation we have termed two-sided.

$$\hat{R}_{xx}(m) = \frac{1}{M-m} \sum_{n=1}^{M-m} x(n)x(n+m) \qquad m = 0, 1, 2, \ldots M\text{-}1 \qquad\qquad 6$$

$$\hat{R}_{xy}(m) = \frac{1}{M-m} \sum_{n=1}^{M-m} x(n)y(n+m) \qquad m = 0, 1, 2, \ldots M\text{-}1 \qquad\qquad 7$$

where M is the total number of points in the data record.

It is readily observed from equations 6 and 7 that the variance (statistical weight) is not equal for each point of the correlation. For example, the $m = 0^{th}$ value of the correlation is formed from the sum of M multiplications, while the $m = (M\text{-}1)^{th}$ value of the correlation is formed

from the sum of only one product term. To achieve an unbiased discrete time correlation function with equal statistical weight (equal variance) for each correlation point, we chose to divide the M data points into 2λ segments of length N (refer to Figure 3.6). Thus, $2\lambda N = M$, and λ is the number of 2N segments of M. We then defined a p segment where p includes 2N points (i.e. one of the λ segments). For M equal to some 2^x number of data points, we can set the limits on each variable in our EV correlation formula: $N = 1,2,3,\ldots 2^x/2\lambda$; $n = 1,2,3,\ldots N$; $m = 0,1,2,\ldots N\text{-}1$; $p = 0,1,2,\ldots 2\lambda\text{-}1$. The one-sided discrete time EV correlation formulas are given in equations 8 and 9:

$$\hat{R}_{xx}(m) = E\left[\hat{R}_{xx}(m)_p\right] = \frac{1}{(2\lambda-1)N} \sum_{p=0}^{2\lambda-2} \sum_{n=pN}^{(p+1)N-1} x(n)x(n+m) \qquad 8$$

$$\hat{R}_{xy}(m) = E\left[\hat{R}_{xy}(m)_p\right] = \frac{1}{(2\lambda-1)N} \sum_{p=0}^{2\lambda-2} \sum_{n=pN}^{(p+1)N-1} x(n)y(n+m) \qquad 9$$

In effect, these formulas provide an expected value for the correlation by averaging the correlation from $2\lambda\text{-}1$ of the p segments, each of length 2N. From Bendat and Piersol, the autocorrelation function is by definition an even function, [93] and a one-sided version, where the shift occurs only toward positive m, is sufficient for this process. However, for the cross-correlation, the relationship between a positive shift in m ($R_{xy}(+m)$) and a negative shift in m ($R_{xy}(-m)$) is not as straightforward. [94] To achieve a two-sided cross-correlation with equal variance, we shifted the signals in both the positive and negative direction and linked these two results at the $m = 0$ point.

For a practical understanding of how the formula operates on the data, consider taking the first 2N points (sections A and B in Figure 3.6) as the first 2N segment (where $p = 0 = p_0$). The correlation of the first N points (section A) can be calculated using these first 2N points.

By shifting the p segment down N points (to section B) and repeating the correlation process, we will obtain the correlation for the points in section B using the points from sections B and C. This process is repeated until the final 2N points are employed as the last p segment. In the calculation of each segment's correlation, we use only N points at any one time for the multiplication and summation. We accomplish this by setting the last N points in the shifting p segment to zero. These zeros are shifted through the p segment as the p segment is shifted down each data point (e.g. the last value of the p segment used to calculate the $m = 0^{th}$ correlation point will become the first value of the p segment used to calculate the $m = 1^{th}$ correlation point). Thus, at any one time, N of the multiplication and summation values are zero. The factor in the summation is $2\lambda - 1$, rather than 2λ, because the first and last segments are not included in the correlation. A two-sided process for cross-correlation is illustrated in Figure 3.6. The process is the same for both a positive shift in m to calculate ($R_{xy}(+m)$) (top portion of the figure) and a negative shift in m to calculate ($R_{xy}(-m)$) (bottom portion of the figure). For this correlation implementation, each correlation point has equal variance.
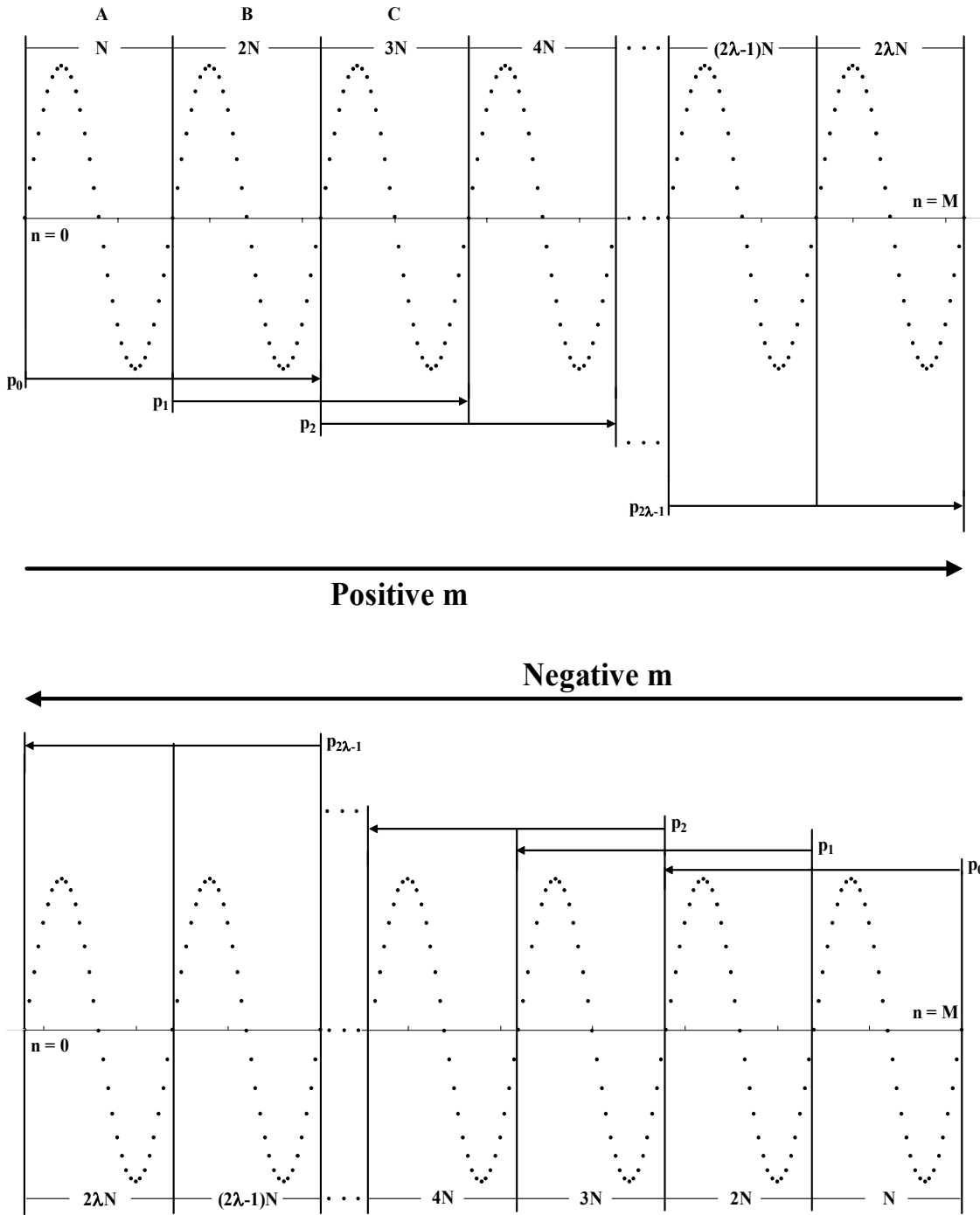
Figure 3.6 Illustration of the Data Partitioning Method. A total of M points are segmented into 2λ divisions of N-points each. Any two consecutive N-point divisions constitute a 2N point partition (p). The points within a p segment are employed to generate the correlation for the first N points in the segment. The cross-correlation is obtained by averaging the correlation over 2p segments. Twice the number of segments (4λ) occurs in the cross-correlation due to the positive shift in time (Positive m) and the negative shift in time (Negative m).

Spectral Algorithm Implementation

The discrete time version of the one-sided autospectrum is related to the continuous

Fourier transform in equations 10 and 11. [92]

$$X(k) = \frac{1}{h}X(f) \qquad h = \text{sample period} = 1/(f_s) = 1/(\text{sampling freq.}) \qquad 10$$

$$G_{xx}(f) = h^2 G_{xx}(k) = \frac{2}{T}E\left[|X(k)|^2\right] \qquad 11$$

Combining these formulas and equation 3, with $T = Nh$ (where T is the sampling period and

N is the number of data points in T), we obtain the following formula for the estimate of the

one-sided auto-spectra.

$$\hat{G}_{xx}(k) = \frac{h^2}{2\lambda}\left(\frac{2}{Nh}\right)\sum_{r=1}^{2\lambda}|X(k)_r|^2 = \left(\frac{h}{\lambda N}\right)\sum_{r=1}^{2\lambda}X^*(k)_r X(k)_r \qquad 12$$

This formula includes an averaging over all 2λ segments of the data record where r

increments through the N-point segments (e.g. $r = 1$ is segment A in Figure 3.6). Each one-

sided spectrum is calculated for N points, and this process is repeated until a spectrum has

been calculated for all 2λ segments. The spectra for all 2λ segments are then averaged to

provide an estimate of the autospectrum over all M points.

Following the development of the auto-spectrum estimate above for 2λ sequential

segments of the M-point data, the cross-spectrum estimate is obtained (equation 13).

$$\hat{G}_{xy}(k) = \left(\frac{h}{\lambda N}\right)\sum_{r=1}^{2\lambda}X^*(k)_r Y(k)_r \qquad 13$$

Note that the cross-spectrum estimate contains both magnitude and phase information. This

differs from the autospectrum estimate which contains only a magnitude. To actually

implement this formula, we expand the Fourier transforms into their real and imaginary parts

as given below:

$$X^*(k) = X_R(k) - jX_I(k) \qquad\qquad 14$$

$$Y^*(k) = Y_R(k) - jY_I(k) \qquad\qquad 15$$

Here the subscripts R and I denote the real and imaginary parts of the DFT respectively.

When the product of $X^*(k)_r$ and $Y(k)_r$ (r is the index of the 2λ segments) is formed within the

summation of the cross-spectrum estimate, four product terms are generated (two real and

two imaginary) summed over the 2λ partitions. Writing out these terms under the summation

and collecting real and imaginary parts produces the following:

$$\hat{G}_{xy}(k) = \frac{h}{\lambda N}\left[\sum_{r=1}^{2\lambda}\left(X_R(k)_r Y_R(k)_r + X_I(k)_r Y_I(k)_r\right) + j\sum_{r=1}^{2\lambda}\left(X_R(k)_r Y_I(k)_r - X_I(k)_r Y_R(k)_r\right)\right]$$

Simplifying the notation (below), this equation can be written as equation 16.

$$XY_R = X_R(k)_r Y_R(k)_r + X_I(k)_r Y_I(k)_r$$

$$XY_I = X_R(k)_r Y_I(k)_r - X_I(k)_r Y_R(k)_r$$

$$\hat{G}_{xy}(k) = \frac{h}{\lambda N}\left[\sum_{r=1}^{2\lambda}\left(XY_R(k)_r\right) + j\sum_{r=1}^{2\lambda}\left(XY_I(k)_r\right)\right] = \frac{h}{\lambda N}\left[\sum XY_R(k) + j\sum XY_I(k)\right] \quad 16$$

where the summation symbol and the removal of the subscript from the DFT terms

indicates a summation over the 2λ segments.

In this implementation, each spectral point has equal variance. The magnitude of the cross-

spectrum estimate is given by equation 17.

$$\hat{G}_{xy}(k)_{mag} = \frac{h}{\lambda N}\left[\sum XY_R(k)^2 + \sum XY_I(k)^2\right]^{\frac{1}{2}} \qquad\qquad 17$$

The determination of an estimate for phase is slightly more involved, as the arctangent

function will only place the complex vector in the first or fourth quadrant. Therefore, we

determined the quadrant separately, and placed the angle in the proper quadrant.

i. First quadrant: $\sum XY_R(k)$ and $\sum XY_I(k)$ both positive

$$\hat{G}_{xy}(k)_{phase} = \tan^{-1}\left[\frac{\sum XY_I(k)}{\sum XY_R(k)}\right]$$ 18

ii. Second quadrant: $\sum XY_R(k)$ negative, $\sum XY_I(k)$ positive

$$\hat{G}_{xy}(k)_{phase} = \tan^{-1}\left[\frac{\sum XY_I(k)}{\sum XY_R(k)}\right] + \pi(rad)$$ 19

iii. Third quadrant: $\sum XY_R(k)$ and $\sum XY_I(k)$ both negative

$$\hat{G}_{xy}(k)_{phase} = \tan^{-1}\left[\frac{\sum XY_I(k)}{\sum XY_R(k)}\right] - \pi(rad)$$ 20

iv. Fourth quadrant: $\sum XY_R(k)$ positive, $\sum XY_I(k)$ negative

$$\hat{G}_{xy}(k)_{phase} = \tan^{-1}\left[\frac{\sum XY_I(k)}{\sum XY_R(k)}\right]$$ 21

The phase spectrum estimate has valid values between $\pm \pi$, irrespective of the magnitude of the data. Therefore, erratic swings in phase will occur at frequencies where noise

73

dominates the signal. Displaying these erratic swings in the phase plot was avoided by comparing the kth point in the magnitude plot to the maximum value of the cross-spectrum magnitude estimate. If the value of the magnitude plot at this k^{th} point was less than 5% of the maximum, then we assigned the corresponding point in the phase plot a value of zero (i.e. of no interest). This percent value for the zero threshold is adjustable within the code to allow accommodation of various noise levels.

Coherence Algorithm Implementation

The coherence estimate in equation 22 follows directly from the determination of the auto- and cross-spectral estimates. [92, 93]

$$\hat{\gamma}_{xy}^{2}(k) = \frac{\left|\hat{G}_{xy}(k)\right|^{2}}{\hat{G}_{xx}(k)\hat{G}_{yy}(k)} \qquad\qquad 0 \le \hat{\gamma}_{xy}^{2} \le 1 \qquad\qquad 22$$

For the sake of brevity, we hereafter drop the phrase "estimate" when referring to the auto- and cross-spectrum and coherence. Furthermore, the notation for the auto- and cross-correlation, auto- and cross-spectra, and coherence will be shortened by dropping the discrete time function notation. In equation 22, the auto- and cross-spectra are calculated with discrete time algorithms as opposed to the assumption of continuous time in equation 5. Since the auto- and cross-spectra are averaged from the 2λ partitions of N points, the coherence is also estimated over the 2λ partitions. When calculating the coherence, the noise threshold (5% threshold mentioned previously in the phase calculation description) was again employed.

Verification of the Implemented Algorithms

The EV algorithms were initially programmed and tested in ML. After testing, the algorithms were implemented in LV as virtual instruments (VIs). Test signals are used, first to validate the implementation of the algorithms, and second to illustrate the detection of an input signal with noise present. In both the EV correlation and spectral analyses, we provide unaveraged versions of these calculations obtained using the non-segmented signal. This is included to illustrate the noise reduction obtained using the EV algorithm. The cross-correlation function in ML is used to generate the standard unbiased cross-correlation. The ML algorithm creates a correlation with 2M-1 points, where M is the total number of data points in y(n) while the EV algorithm generates 2N-1 points. For the unaveraged spectra, the calculation will produce M points, whereas the averaged spectra will be N points in length. It is important to note that we employed pseudorandom noise non-integer multiple (PRN-NIM) as demonstrated by Maki. [95] This type of noise was used to minimize bias error due to correlated effects of pseudo-random noise (PRN) [95] and to illustrate the effectiveness of the averaging techniques. The PRN-NIM was generated as a sum of sinusoids where the sinusoids had frequencies that were non-integer multiples of each other. The phases for each sinusoid were assigned by a pseudorandom process over each N-point period using the ML pseudorandom number generator in the range from 0 to 2π. An illustration of a known input signal with PRN added is provided in the results for a comparison between the two types of noise for both correlation and spectral methods. A brief comparison of the two types of PRN is given in the Discussion.

The types of signals we employed in our tests were as follows: elementary sinusoids without noise for which the correlation, spectra and coherence was known; elementary

sinusoids plus high PRN-NIM; elementary sinusoids plus high PRN. The first, noise-free signal assures validity of the implemented correlation and spectral algorithms. The PRN-NIM and PRN test signals illustrate the performance of our implementation of the spectral and correlation methods.

Samples of Typical Program Runs

Verification of the Implemented Algorithms

Elementary Sinusoidal Signals with Known Correlation, Spectra and Coherence

Figures 3.7 and 3.8 illustrate the results for a pair of basic sinusoidal signals. The two signals used, x(n) and y(n), are given by:

$$x(n) = \sqrt{2}\left[\sin(nf) + \frac{1}{\sqrt{1.33}}\sin(2nf) + \frac{1}{\sqrt{1.5}}\sin(4nf) + \frac{1}{\sqrt{2}}\sin(8nf)\right] + random\ noise \quad 23$$

$$y(n) = \sqrt{2}\left[\sin(nf + \frac{\pi}{2}) + 0 + \frac{1}{\sqrt{1.5}}\sin(4nf + \frac{\pi}{3}) + \frac{1}{\sqrt{2}}\sin(8nf - \frac{\pi}{4})\right] + random\ noise \quad 24$$

where f is the fundamental frequency and random noise is PRN-NIM.

The parameters for the simulation (refer to Figure 3.6) were: M = 20480, λ = 10, N = 1024, f = 8 Hz. Random noise was equal to zero for this test, and the sine wave amplitudes were limited to a range of $\pm\ 2^{1/2}$. The threshold for the phase and coherence plots was set to 5% of the maximum value of the cross-spectrum magnitude. Values of G_{xy} magnitude that were less than this 5% value were set to zero before they were used to calculate the phase and coherence. However, all values of the G_{xy} magnitude were preserved for the cross-spectral magnitude plot in Panel C of Figure 3.8.

76

The sinusoidal signals are shown in Panels A and B of Figure 3.7. These signals were cross-correlated using two methods. The first method was the EV algorithm (Panel E) and the second method (Panel F) was the ML algorithm (standard method). Because we partition the data into smaller segments, the number of points in the EV correlation is limited to 2N-1 (2047) as opposed to the 2M-1 points generated in the ML algorithm. Panel C illustrates the 2N-1 point R_{xy} (EV algorithm without averaging). The ML cross-correlation of 2N-1 points is illustrated in Panel D, while the entire ML cross-correlation (2M-1 points) is presented in Panel F. Panels C, D and E are very similar in appearance, as we are using a deterministic signal without noise, and are presented to verify the methods. Note the divergence at the end points of Panel D.

In Figure 3.8 (no random noise) the autospectra from the signals of equations 23 and 24 are shown in Panels A and B. Panels C and E illustrate the cross-spectral plots for magnitude and phase respectively. The coherence of the two input signals is provided in Panel D, and the unaveraged cross-spectrum is given in Panel F (inconsistent estimate). [93] As expected when using deterministic signals with no noise, Panels C and F are identical.

Correlation for Sinusoids Without Noise
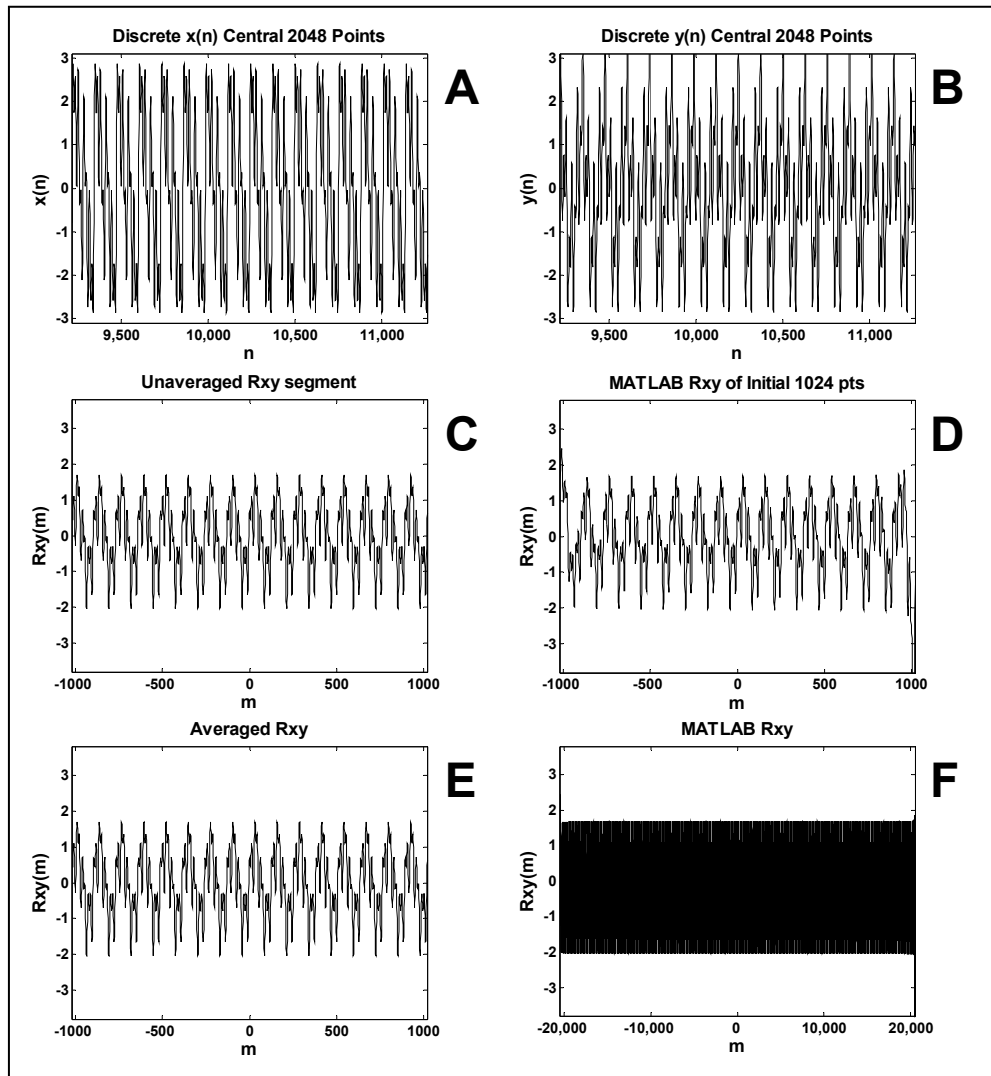
Figure 3.7 Signals and Correlation (No Noise). Panels A and B contain 2048 points of the sinusoidal signals with no random noise. R_{xy} using the EV algorithm is given in Panel E. In Panel C, the unaveraged R_{xy} for a single N-point segment of the data partition is shown (ie. this is one of the R_{xy} segments included in the averaged result in Panel E). Panel F shows the ML R_{xy} using the complete $x(n)$ and $y(n)$ signals. Panel D contains the ML R_{xy} for only the initial 1024 points of $x(n)$ and $y(n)$. Note the divergence at the end points of Panel D.

Spectra for Sinusoids Without Noise
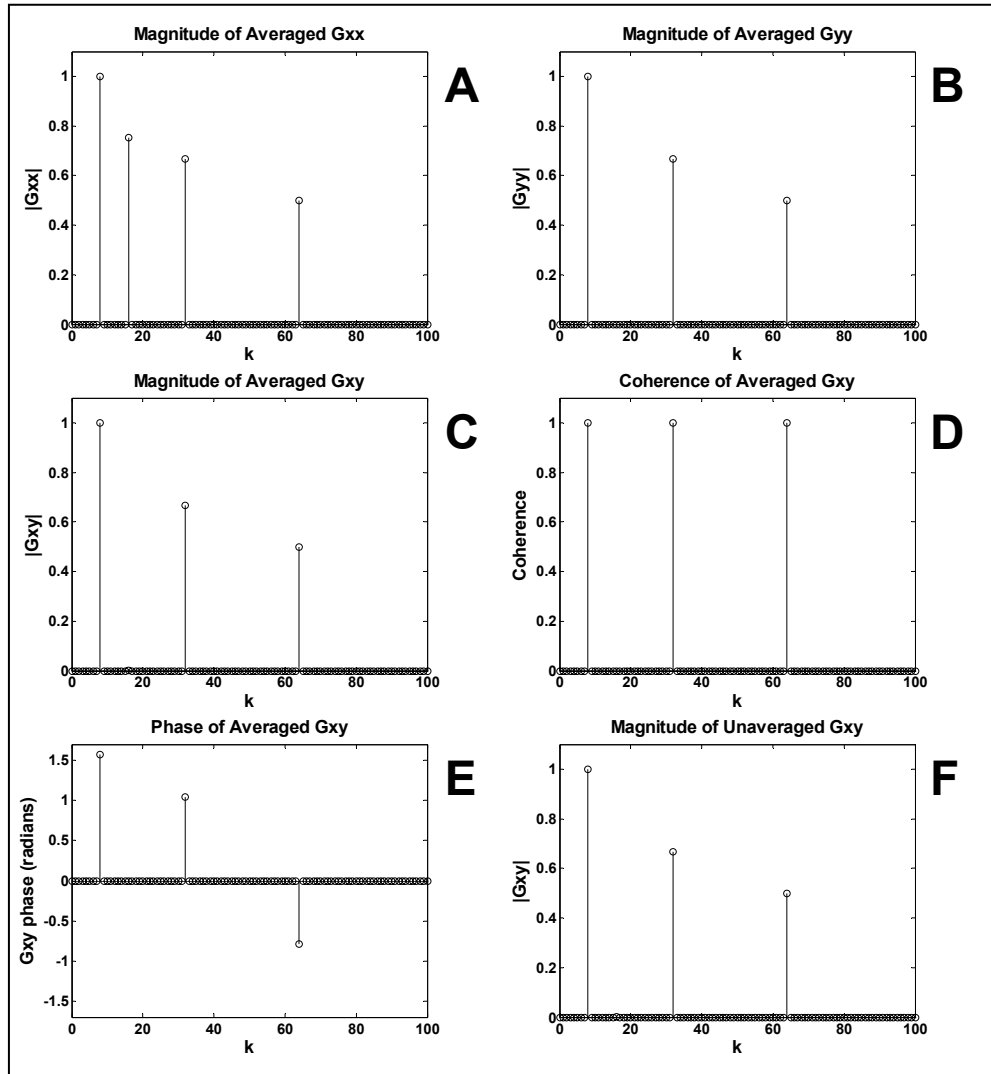
Figure 3.8 Spectra (No Noise). Panels A and B illustrate the autospectra of the sinusoidal signals without random noise using the averaging algorithm. In Panels C and E, the EV algorithm was used to obtain the magnitude and phase of G_{xy}. Panel D shows the coherence of the cross-spectrum obtained using the averaged G_{xy}. In Panel F, the magnitude of the unaveraged G_{xy} is given, where the cross-spectrum was obtained without partitioning the signals.

Elementary Sinusoidal Signals with High PRN-NIM Added

Figures 3.9 and 3.10 illustrate the results for the sinusoidal signals of equations 23 and 24

where a large amplitude of PRN-NIM was added (random noise had a range of

approximately $\pm\,50*2^{1/2}$ and the sine wave amplitudes were limited to the $\pm\,2^{1/2}$ range, for a 50/1 noise to signal ratio). The parameters for this simulation (refer to Figure 3.6) were: M = 20480, λ = 10, N = 1024, f = 8 Hz. The zero threshold for the phase and coherence plots was set to 5% of the maximum value of the cross-spectrum magnitude.

Panels A and B of Figure 3.9 show sinusoidal signals with high PRN-NIM added. The signals were cross-correlated using the EV method (Panel E) and the ML algorithm (Panel F). Panel C illustrates the 2N-1 point R_{xy} (EV algorithm without averaging), and Panel D shows a 2N-1 point cross-correlation obtained using the ML algorithm.

In Figure 3.10, the averaged autospectra from the signals with high PRN-NIM contain noise peaks at the appropriate frequencies (Panels A and B). The peaks from the sinusoidal signals of known frequency appear just above the baseline, being vastly overshadowed by the noise peaks. Panels C and E illustrate the cross-spectral plots for magnitude and phase respectively. The coherence estimate for the input signals is provided in Panel D. Panel F shows the cross-spectral results obtained using the algorithm without averaging.

Correlation for Sinusoids Plus High PRN-NIM
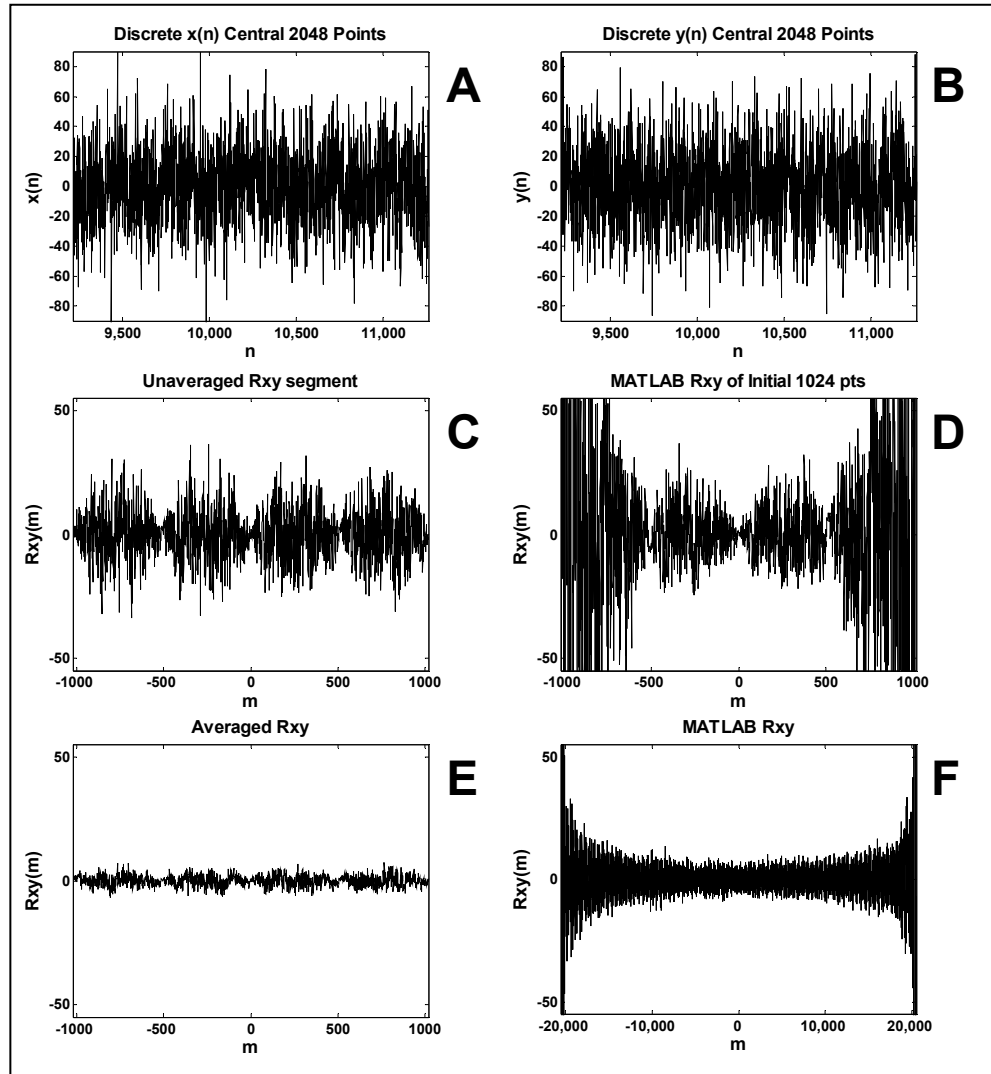
Figure 3.9 Signals and Correlation (PRN-NIM). Panels A and B contain 2048 points of the sinusoidal signals plus PRN-NIM of amplitude $\pm 50*2^{1/2}$. These are the same signals as in Figure 3.7, with a noise to signal ratio of 50/1. R_{xy} using the EV algorithm is given in Panel E. In Panel C, the unaveraged R_{xy} for a single N-point segment of the data partition is shown (i.e. this is one of the R_{xy} segments included in the averaged result in Panel E). Panel F shows the ML R_{xy} using the complete x(n) and y(n) signals. Panel D contains the ML R_{xy} for only the initial 1024 points of x(n) and y(n). Note the large divergence at the endpoints in Panels D and F.

Spectra for Sinusoids Plus High PRN-NIM
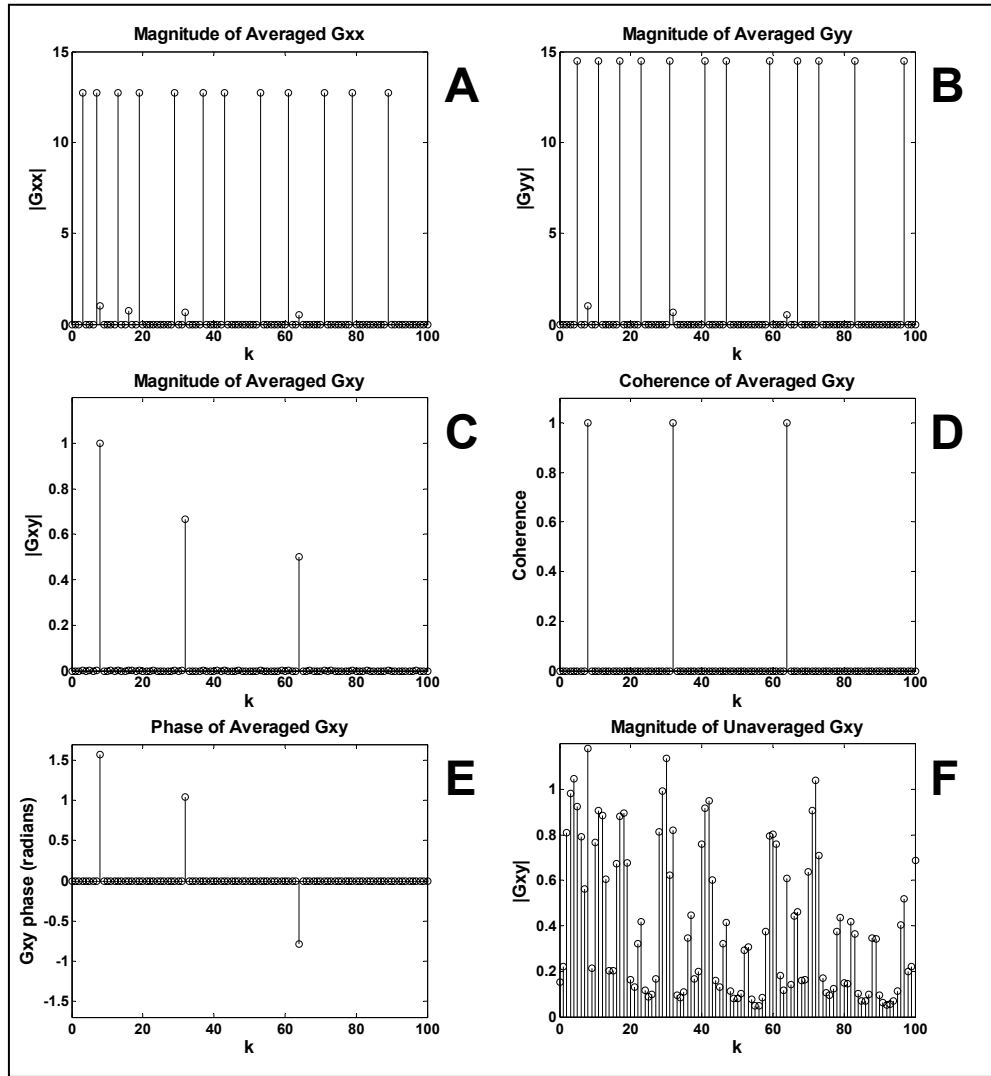
Figure 3.10 Spectra (PRN-NIM). Panels A and B illustrate the autospectrum of the sinusoidal signals plus PRN-NIM (amplitude $\pm 50*2^{1/2}$) using the EV algorithm. These are the same signals as in Figure 3.7, with a noise to signal ratio of 50:1. In Panels C and E, the EV algorithm was used to obtain the magnitude and phase of G_{xy} for the two signals. Panel D shows the coherence of the cross-spectrum obtained using the averaged G_{xy}. In Panel F, the magnitude of the unaveraged G_{xy} is given, where the cross-spectrum was obtained without partitioning the signals. Note the difference in noise levels between Panels C and F.

Elementary Sinusoidal Signals with High PRN Added

Figures 3.11 and 3.12 illustrate the results for the sinusoidal signals of equations 23 and 24

where a high amount of PRN was added (PRN had a range of $\pm 10*2^{1/2}$ and the sine waves

82

were limited to the $\pm 2^{1/2}$ range, for a 10/1 noise to signal ratio). The parameters for this simulation (refer to Figure 3.6) were: M = 20480, λ = 10, N = 1024, f = 8 Hz. The zero threshold for the phase and coherence plots was set to 5% of the maximum value of the cross-spectrum magnitude.

Panels A and B of Figure 3.11 show sinusoidal signals with PRN added at approximately 10 times the amplitude of the largest sinusoid. These two signals were cross-correlated using the EV method (Panel E) and the ML algorithm (Panel F). Panel C illustrates the 2N-1 point R_{xy} (EV algorithm without averaging), and Panel D shows a 2N-1 point cross-correlation obtained using the ML algorithm.

Panels A and B of Figure 3.12 show the autospectra from the signals with the added PRN. The cross-spectra, revealing the common frequencies between the input signals, are shown in Panels C and E (magnitude and phase), and the coherence estimate is provided in Panel D. An unaveraged (inconsistent estimate) of the cross-spectral magnitude is given in Panel F. Note the similarity between Panels C and F.

Correlation for Sinusoids Plus High PRN
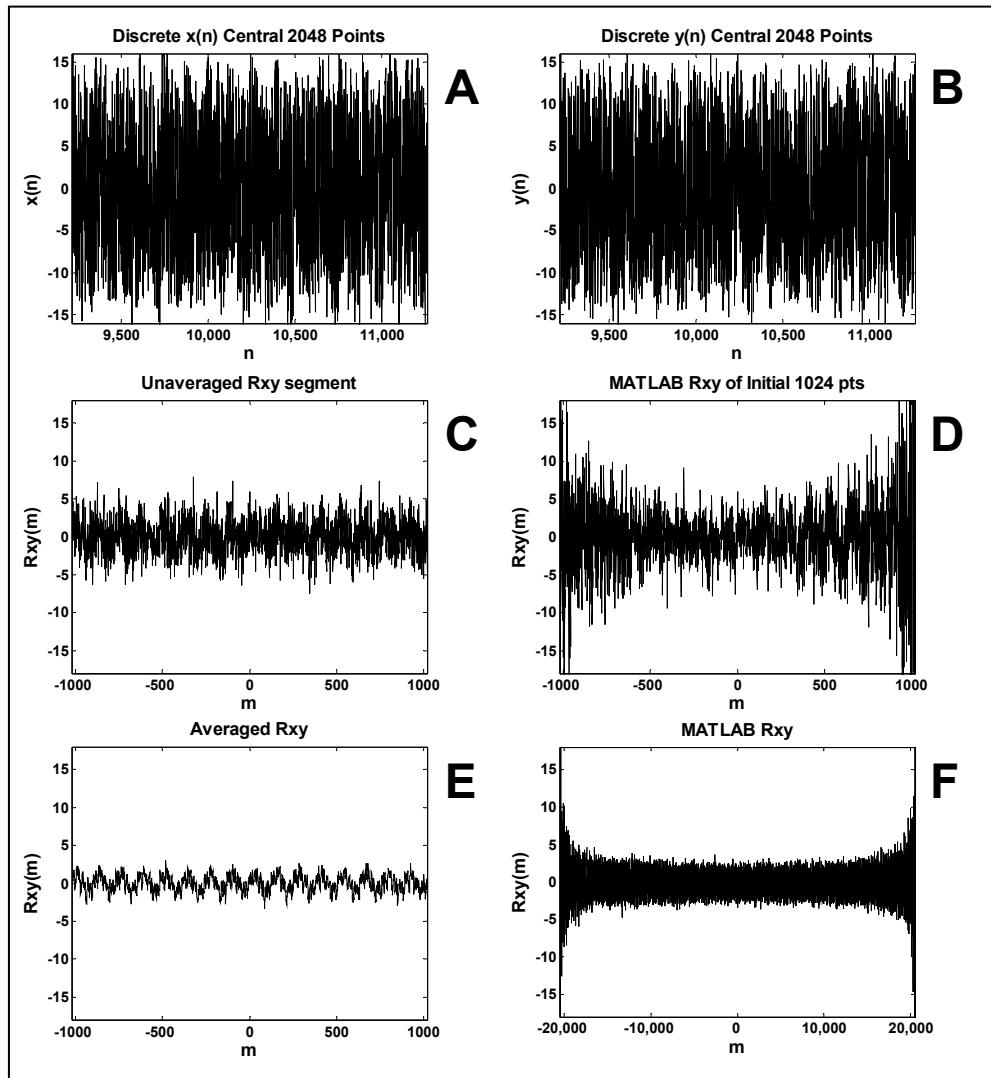
Figure 3.11 Signals and Correlation (PRN). Panels A and B contain 2048 points of the sinusoidal signals plus PRN of amplitude $\pm 10*2^{1/2}$. These are the same signals as in Figure 3.7, with a noise to signal ratio of 10:1. R_{xy} using the EV algorithm is given in Panel E. In Panel C, the unaveraged R_{xy} for a single N-point segment of the data partition is shown (i.e. this is one of the R_{xy} segments included in the averaged result in Panel E). Panel F shows the ML R_{xy} using the complete $x(n)$ and $y(n)$ signals. Panel D contains the ML R_{xy} for only the initial 1024 points of $x(n)$ and $y(n)$. Note the large divergence at the endpoints of Panels D and F.

Spectra for Sinusoids Plus High PRN
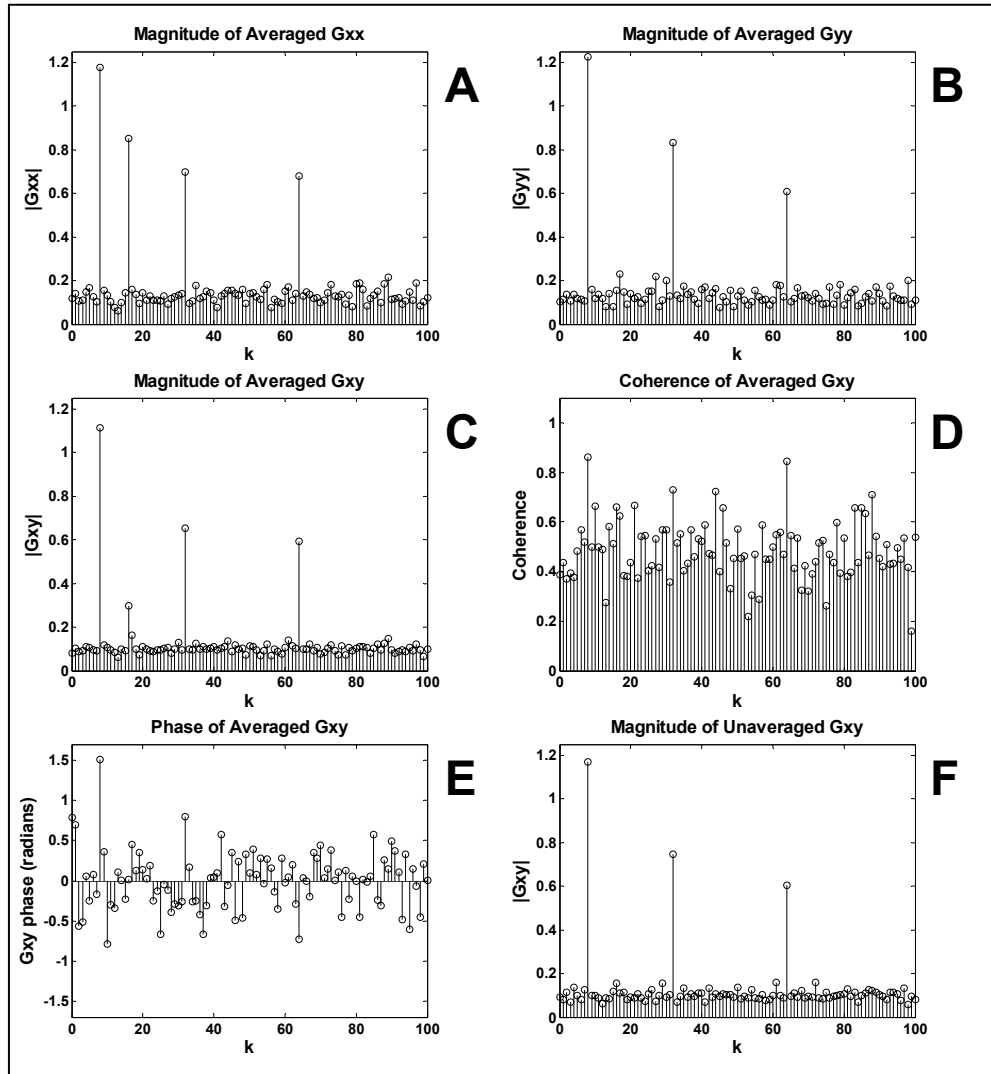
Figure 3.12 Spectra (PRN). Panels A and B illustrate the autospectrum of the sinusoidal signals plus PRN (amplitude $\pm 10*2^{1/2}$) using the EV algorithm. These are the same signals as in Figure 3.7, with a noise to signal ratio of 10:1. In Panels C and E, the EV algorithm was used to obtain the magnitude and phase of G_{xy} for the two signals. Panel D shows the coherence of the cross-spectrum obtained using the averaged G_{xy}. In Panel F, the magnitude of the unaveraged G_{xy} is given, where the cross-spectrum was obtained without partitioning the signals. Note the similarity between Panels C and F.

Characteristic Effects of PRN vs. PRN-NIM

Apparent in Figure 3.12 (Panels C and F) is the lack of noise reduction in the segmented cross-spectrum of the signal with PRN as compared to the unsegmented cross-spectrum.

Furthermore, there is little or no reduction in noise level between auto- and cross-spectral analyses (Panels A, B and C). These plots seem to indicate that there is no advantage to the segmented cross-spectrum for noise reduction when PRN is used, especially when compared to the substantial noise reduction seen in Figure 3.10 (where PRN-NIM is used). To explain this outcome, a correlation test was performed for both the ML PRN and the PRN-NIM (Figure 3.13), to reveal the degree to which the noise is correlated with itself. [96] Correlated noise would affect the ability of any algorithm to reduce noise levels using averaging techniques. It should be noted that we tested PRN from several sources including LV, Mathematica®, PCQNG[TM], [97] and random.org (True Random Number Service). [98] The ML PRN algorithm performed at least as well as any of these other sources, so only the ML PRN is included in Figure 3.13. In Panel A of Figure 3.13, the initial 64 points (from a record of 20480 points) are shown for two records of ML PRN. Panel B of Figure 3.13, illustrates the same for PRN-NIM. These plots illustrate that the noise from each source was of approximately the same amplitude. The autocorrelation for one of the ML PRN signals from Panel A is shown in Panel C, and the cross-correlation for the pair of ML PRN signals from Panel A is shown in Panel E. The corresponding records for the PRN-NIM are shown in Panels D and F. The cross-correlation of the PRN-NIM demonstrates a large reduction in noise level, as seen in Panel F (uncorrelated noise), while the cross-correlation of PRN, as illustrated in Panel E, shows no reduction (correlated noise).

Correlation of MATLAB PRN and PRN-NIM
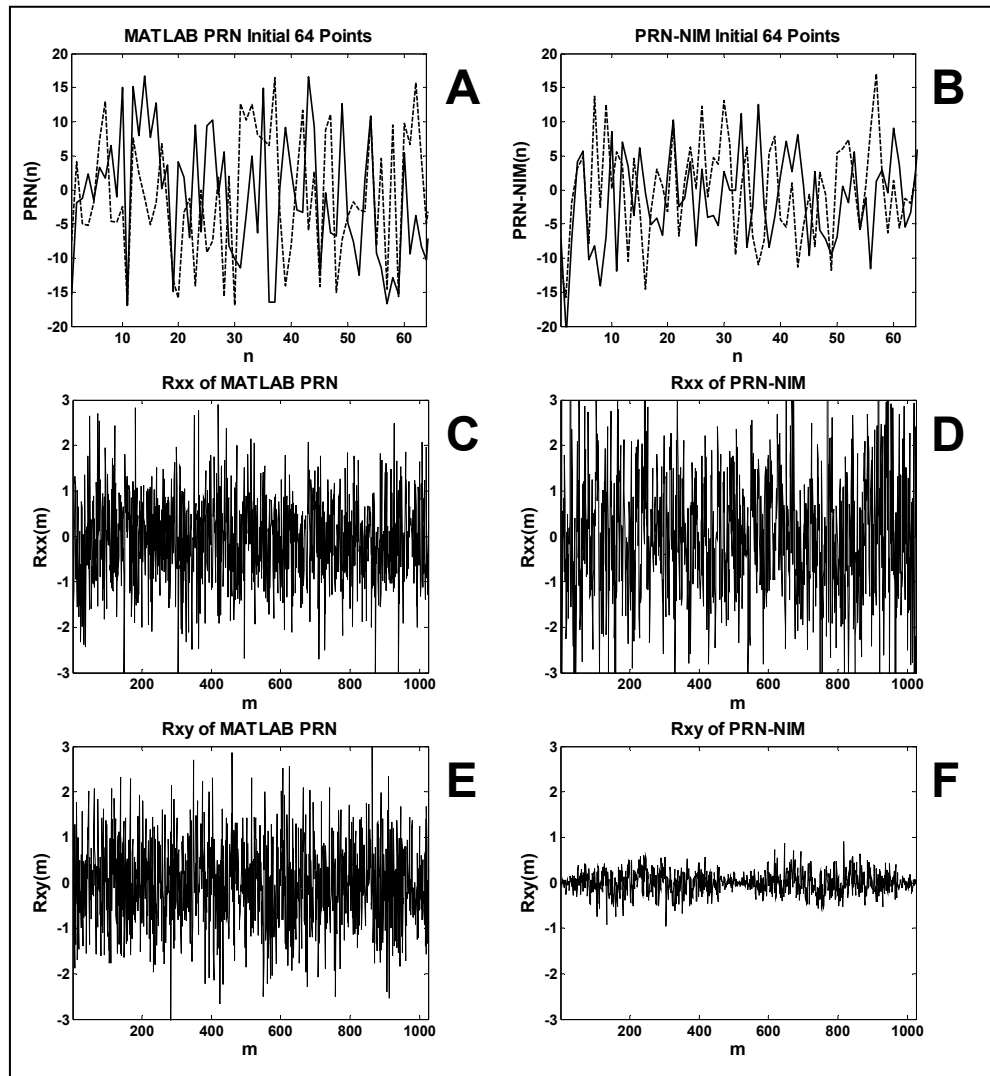
Figure 3.13 Signals and Correlation (MATLAB PRN and PRN-NIM). Panels A and B illustrate two types of noise: ML PRN (Panel A), PRN-NIM (Panel B). In both panels, the dotted line and solid line represent two different noise signals. In Panel C the R_{xx} is shown for one of the noise signals in Panel A (zero lag point removed), and Panel D shows the R_{xx} for one of the noise signals in Panel B (zero lag point removed). Panel E gives the R_{xy} of both noise signals in Panel A, and Panel F shows the R_{xy} for both noise signals in Panel B. This is the center portion (with the minimum variance) of the 40959 points in the R_{xy}.

Biomedical Applications Example

Coincident HRV and respiratory signals from a pediatric subject are shown in Panels A

and B of Figure 3.14 (a representative number of data points from the total number data

points). For this subject, the heart rate was approximately 180 b.p.m., and the respiratory

rate was in the range of 0.6 to 1.0 Hz. The data was provided at 224 Samples/sec from the

SpaceLabs Ultraview 1700 Monitoring system (Spacelabs Medical, Redmond, WA, USA)

SQL database. The parameters for this application (refer to Figure 3.6) were: 7 segments

with 128 points per segment. The respiratory signal (arbitrary units) was re-sampled at the

same points in time as the HRV signal. The zero threshold for the phase and coherence plots

was set to 30% of the maximum value of the cross-spectrum magnitude.

Panels C and E of Figure 3.14 show the cross-spectrum (magnitude and phase) from the

HRV and respiratory signals. The coherence estimate for the HRV and respiratory signals is

shown in Panel D, and the unaveraged estimate of the cross-spectral magnitude is provided in

Panel F.

Spectral Analysis of HRV and Resp. Signals
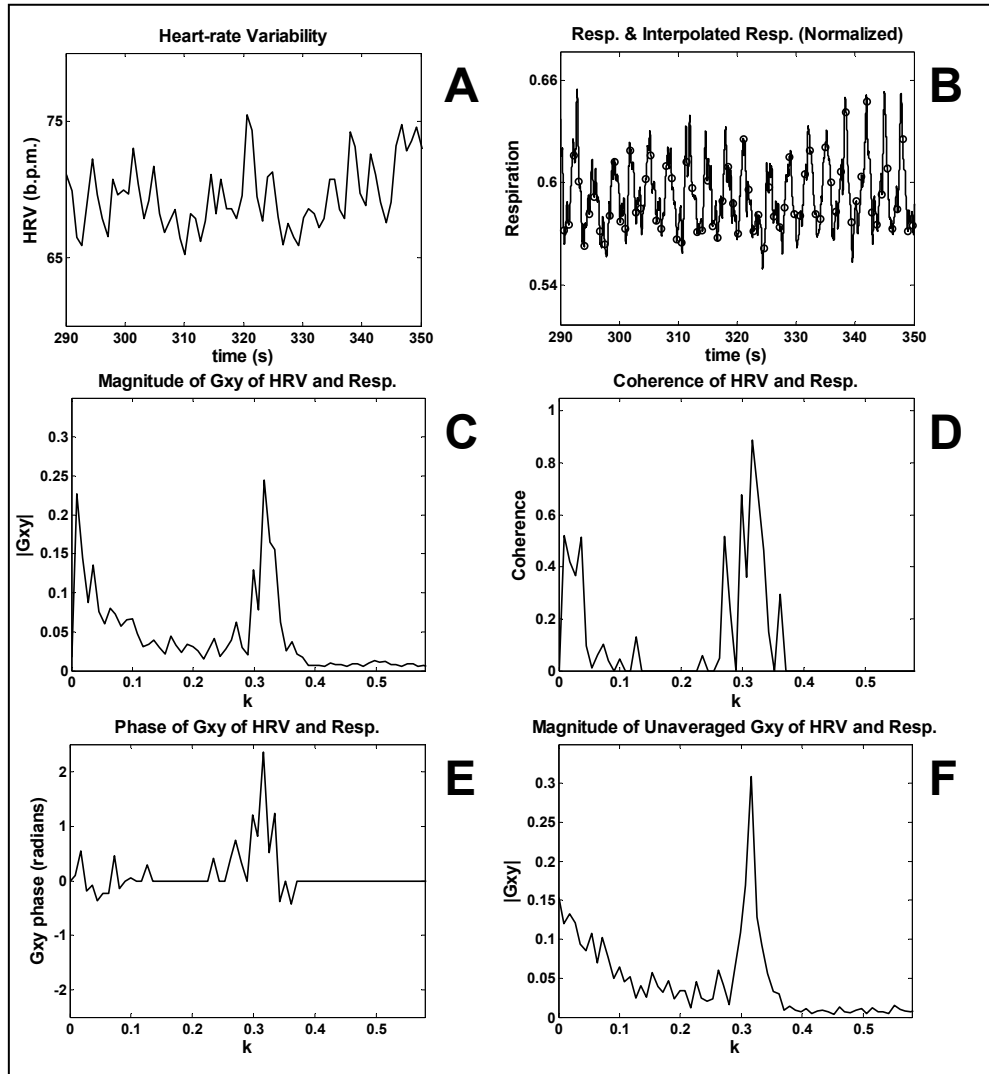
Figure 3.14 Spectra (HRV and Respiration). Panel A illustrates a portion of the HRV signal from a pediatric subject. Panel B shows a portion of the coincident respiratory signal from the same subject (solid line) with the re-sampled respiratory signal overlaid (circles). In Panels C and E, the magnitude and phase of G_{xy} are shown. Panel D provides the coherence of the cross-spectrum. In Panel F, the magnitude of the unaveraged G_{xy} is given, where the cross-spectrum was obtained without partitioning the signals.

Discussion

There is considerable interdependence in the many processes in biological systems, from the whole organ systems to the level of chemical reactions. Discovery and quantification of

these interactions is valuable in the understanding of normal physiology and in the pathology of disease processes. While most biological processes are both nonlinear and nonstationary, methods of nonlinear and nonstationary analysis are not consistent with the powerful methods of linear analysis, nor do they conform well to the conceptual generalizations of our reasoning. Thus nonlinear processes are sometimes described as counter-intuitive. However, many of these processes may be linearized, and analyzed under carefully controlled circumstances where stationarity may be approximated. Under these conditions we may use correlation and spectral methods to study both the characteristics of individual biological signals as well as the interaction between them. To this purpose, we have developed a very fast and powerful software package to apply the tools of linear signal processing to biological systems.

We have previously reported software packages, specialized to investigate the behavior of very specific biological systems, including thalomo-cortical evoked potentials (LINK computer), [99] neuromuscular bioelectric potentials (PDP-11), [100] neurally evoked potentials (PDP-11), [101] and spectral analysis of the EEG (IBM-AT). [102] Our interests in this application are very general.

Our immediate interests in developing this software are to investigate linear interactions between various biological signals, in health and disease, to provide a tool for behavioral analysis of physical systems, as well as to have a convenient tool to compose and validate an optimal white noise signal for system identification. [103] We define this optimum white noise signal to have broad spectral range and to be independent with itself (uncorrelated with itself, either in time offset or in independent parallel generation). That is, ensemble and segmented independence.

System and Program Description

The flow chart in Figure 3.1 and Figures 3.2 – 3.5 illustrate a number of options that are available within the LV collection and analysis system. With only basic inputs required, the data collection portion is straightforward. Collection files for the data are stored in an efficient 16-bit binary format, and the user can view several channels and track file size information during collection. In the data analysis section the choice of analyses and partitioning of the data is uncomplicated assuming some basic understanding of the data partitioning method and analysis types (see *Computational Methods and Theory* section). A variety of methods are available for auto- and cross-analysis of numerous channels, and the results can be saved for future processing.

Implementation of Digital Algorithms for Correlation, Spectra and Coherence

Correlation Algorithm Implementation

Typical digital correlation algorithms produce marked inconsistencies in their output due to the changing variance (statistical weight) through the record (see discussion of equations 6 and 7 in *Computational Methods and Theory* section). [93] This is illustrated by the results from the ML algorithm in Panels D and F of Figures 3.7, 3.9, and 3.11. In Figure 3.9 Panel F, a value of the correlation exceeding 50 occurs near the endpoints of the ML results; however, in the central portion of the ML results, the cross-correlation is very similar in magnitude to the results we achieved (Panel E). Panel E of Figures 3.7, 3.9, and 3.11, illustrate the effect of equal variance at each data point from the EV algorithm, which produces an output that does not diverge at the endpoints. The implementation of an averaging process to achieve unbiased results and equal statistical weight required

partitioning of each data set, and the resultant correlation contains fewer data points than the standard correlation algorithm. With our implementation of the algorithm, we are showing the local correlation over an extended period of time, and the correlation maintains the same variance at both ends. The standard cross-correlation method shows the global correlation over the same extended period, but it loses resolution at the end points due to monotonically increasing variance. The final step in our implementation averages the correlations for each local area to reveal the average local correlation for the extended period.

Spectral Algorithm Implementation

Dramatic noise reduction is achieved by averaging multiple records from an ensemble of records or from segments of a single record. [92, 93, 95] This effect can be observed when the cross-spectrum from the EV averaging algorithm is compared to the cross-spectrum where averaging is not employed (note Panels C and F of Figure 3.10). In Panel F, the level of the noise overtakes the underlying signal at certain frequencies, whereas the underlying signal is clear from Panel C. The phase plot is restricted to only show phase at frequencies where significant cross-spectral magnitude occurs (e.g. > 5% of maximum).

Coherence Algorithm Implementation

The coherence function is derived from information shared between multiple records of the auto- and cross-spectra. Noise is diminished by elimination of variations which are not common to the two data records: to generate a coherence function which has pragmatic value when displaying only those results where the data exceeds a minimum threshold in the cross-spectral plot (i.e. where the amplitude of the cross spectrum is significant). For our

implementation, the coherence plot reveals peaks of magnitude 1 only at the common frequencies of the test signals and zero at all other frequencies. This interaction between signals is as expected in the absence of noise (Panel D of Figure 3.8) as well as in the presence of very high amplitude (50/1 noise to signal ratio) PRN-NIM noise (Panel D of Figure 3.10).

Verification of the Implemented Algorithms

Elementary Sinusoidal Signals with Known Correlation, Spectra and Coherence

Figures 3.7 and 3.8 illustrate the results for a simple sum of sinusoids with known amplitudes and phase shifts. The auto- and cross-correlations of the elementary sinusoids, shown in Panels C, D and E of Figure 3.7, are periodic as would be expected for periodic input signals. [94] In Panel F, the 2M-1 point ML cross-correlation results are shown for the full data set, and the amplitude is approximately the same as with the EV algorithm results shown in Panel E. In the absence of noise, the EV algorithm generates identical results to the averaged (Panel E) and unaveraged (Panel C) cross-correlation. However this differs from the result of the ML algorithm, where the cross-correlation diverges at the end points in Panel F. This divergence is illustrated in Panel D, where the data set is reduced to N = 1024 points for each signal. This occurs because the variance of the data increases from the variance of 2048 points in the middle (where the signals are completely overlapped) to the variance of 2 data points at the ends (where only a single point of each data set overlaps). While this effect is not dramatic in the absence of noise (Figure 3.7), it is clearly evident when noise is present (Figures 3.9 and 3.11).

Panels A and B of Figure 3.8 illustrate the autospectra of two test signals composed of 4 sinusoids: three sinusoids at frequencies common to both, but differing in phase, and the fourth sinusoid at a frequency present in only one of the signals. The cross-spectral plots demonstrate peaks at the common frequencies (Panel C), with phase shifts of $+\pi/2$, $+\pi/3$, and $-\pi/4$ as seen in Panel E. In Panel D, the coherence is 1 at the frequencies common to the signals and zero elsewhere. The single record cross-spectrum of Panel F is identical to the multiple record cross-spectrum in Panel C. This validates our implementation of the spectral algorithms for the condition of multiple deterministic signals in the absence of noise.

Elementary Sinusoidal Signals with High PRN-NIM Added

Figures 3.9 and 3.10 illustrate the results for elementary sinusoids with known amplitudes and phase shifts with high PRN-NIM added (N/S = 50/1). This high level of PRN-NIM renders signals that show no signs of the underlying sinusoids (Panels A and B of Figure 3.9). Both the auto-correlations (not shown) and cross-correlation (Panels C, D, and F) are noisy, as would be expected in the presence overriding noise. Note that the correlation at the end points in the unaveraged EV algorithm is consistent with the correlation in the central portion (Panel C). However, the ML (standard) algorithm diverges dramatically at the end points (Panel D). For the correlation in Panel C, the variance is constant throughout the record, while the variance in Panel D increases from the center to the endpoints. Additionally, for the EV algorithm, averaging over the segments (2N-1 point correlation for each segment) may be applied to greatly diminish the noise in the correlation record (Panel E), while the ML correlation (2M-1 points) illustrates less noise reduction at the central points and the dramatic divergence at the end points (Panel F).

94

The autospectra of the sinusoids plus high PRN-NIM tests signals are presented in Panels A and B of Figure 3.10. They illustrate the 50 fold N/S ratio of the PRN-NIM noise over the sinusoidal test signals, with the test signals barely above the baseline. The non-overlapping frequencies, which characterize PRN-NIM noise, is also evident in these panels. However, the multiple record cross-spectrum eliminates the PRN-NIM noise, revealing the underlying signal, as evident in the magnitude (Panel C) and phase (Panel E) spectra. These are comparable to the cross-spectral case with no noise present, as seen in Panels C and E of Figure 3.8, with non-zero coherence of 1 only at the common frequency tests signals (Panels D of Figures 3.8 and 3.10). In Panel F, however, the single record cross-spectrum indicates the presence of the PRN-NIM noise in the data, as expected. This validates the implementation of the spectral algorithms in the presence of uncorrelated noise. [93]

Elementary Sinusoidal Signals with High PRN Added

Figures 3.11 and 3.12 illustrate the results for elementary sinusoids with known amplitudes and phase shifts with high PRN added. While the PRN is at a much lower level in Panels A and B of Figure 7 (N/S = 10/1) than for the PRN-NIM shown in Panels A and B of Figure 3.9 (S/N = 50/1), the signals still do not reveal the underlying sinusoids. Both the auto-correlations (not shown) and cross-correlation (Figure 3.11; Panels C, D, and F) are noisy, as would be expected in the presence of overriding noise. However, the correlation at the end points in the unaveraged EV algorithm is consistent with the correlation in the central portion (Panel C), while the ML (standard) algorithm diverges dramatically, with the variance, at the end points (Panel D). Additionally, for the EV algorithm, averaging over the segments (2N-1 points per correlation per segment) may be applied to greatly diminish the noise in the

95

correlation record (Panel E), while the ML correlation (2M-1 points) illustrates less noise

reduction at the central points and divergence at the end points (Panel F).

Panels A and B of Figure 3.12 illustrate the autospectra of the two input signals (with

PRN). The baseline noise is lower than with the PRN-NIM case due to the lower N/S ratio,

and because the power of the PRN is uniformly spread throughout the spectrum. The highly

correlated nature of the PRN is evident in that the N/S ratio is minimally diminished in the

cross spectrum, with high coherence throughout the spectrum. Of particular interest is that

the magnitude of the cross spectrum, at the frequencies of the common test signals, are

actually increased and the phases shifted, indicating interaction between the test signals and

the PRN. These results, for both the PRN and the PRN-NIM cases, are consistent with the

findings reported by Maki, [95] and validate the implemented spectral algorithms.

Characteristic Effects of PRN vs. PRN-NIM

PRN is commonly added to signals in order to achieve increased frequency resolution in

determination of system transfer functions. This is mainly due to its easy availability in

software such as ML. A major problem with this approach is that significant energy in PRN

can oftentimes be associated with frequencies that are integer multiples of frequencies

contained in the signal. This would tend to bias the transfer function and skew results when

using the coherence estimate to determine the linearity of a system. [95, 104] Though Suki and

Lutchen [104] and Victor and Shapley [105] suggest optimized frequencies for non-integer

multiple PRN, the use of PRN-NIM as given by Maki [95] was sufficient for illustrative

purposes. This is because the test signal we selected had known frequencies that were not

multiples, sums or differences of the frequencies employed in the input PRN-NIM. When

PRN is used in signal processing applications, Figure 3.12 clearly illustrates the negative effects of this type of noise. Even with the benefits of averaging the spectra across twenty segments, the noise level remains at around 10-15% of the maximum spectral peaks in both the auto- and cross-spectra. The phase plot reveals obvious problems, with noise phase cluttering the peaks of the underlying signals. This makes it difficult for the phase plot to provide any meaningful information. The coherence estimate is generally in the range of 0.3 to 0.8 at frequencies where only PRN is present, while the coherence of the underlying signals is reduced from the expected value of unity.

Correlation tests [96] were performed on the two noise sources that were used (PRN and PRN-NIM) to reveal the degree to which each noise source was correlated with itself (i.e. one run is highly correlated with an independent run using the same algorithm). Apparent from Figure 3.13 is the fact that the PRN noise source is highly correlated with itself, in contrast to the PRN-NIM. The correlation test for both types of noise (Figure 3.13) provides a clear illustration of why the segmented cross-spectral algorithm in Figure 3.12 fails to eliminate the high PRN noise. As seen in Figure 3.13 (Panels C and E), there is no reduction in correlation between the autocorrelation and the cross-correlation, indicating the PRN is highly correlated with itself. With PRN-NIM (Panels D and F), there is a substantial reduction in correlation between the R_{xx} and the R_{xy}, which demonstrates that the PRN-NIM is uncorrelated with itself. This correlation between PRN signals explains the lack of noise reduction between the G_{xx} and G_{xy} in Figure 3.12. Since the signals contain noise which is correlated with itself at these frequencies, no amount of averaging will be able to remove this noise component.

The negative effects of commonly used PRN make it unreliable for use in system analyses where the transfer function is unknown. However, it is useful to illustrate the ability of our LV software implementation to assess the value of different types of test signals used for system analysis.

Biomedical Applications Example

Figure 3.14 illustrates the interaction between HRV and respiration. The cross-spectral magnitude plot (Panel C) illustrates the interaction of respiration with heart-rate resulting in sino-atrial arrhythmia occurring from 0.3 to 0.35 Hz. In Panel D the coherence is seen to peak at 0.9 in this frequency range, indicating a strong linear relationship. From the phase plot (Panel E), respiration is seen to lead heart-rate by about 2.2 radians at the 0.32 Hz (approximately 1.05 seconds). This relationship has been demonstrated previously by many authors, [106] and is illustrated here to demonstrate the utility of the software.

Advantages of this Software

The first advantage that the PAASv1 software has is its use of the modified algorithms for correlation and spectral analysis. The maintenance of an even statistical weight for each point produces correlations that are uniform (equal variance) from beginning to end. This is in contrast to the typical correlation algorithm, such as that used by ML, where the beginning and ending points reveal large inconsistencies, especially with higher noise levels. The averaging process, employed in EV spectral analysis, has the advantage of greatly reducing the noise level. With cross-spectral analysis and coherence estimates, this noise reduction helps clarify the true underlying signals when heavy noise is present.

A primary feature of our software is the implementation and packaging of data collection and data analysis routines. These routines are optimized for unbiased estimation of correlation and spectral analysis of signals and systems. This combination of features allows researchers to readily collect, analyze and store the analysis for many types of electrical signals, from biological or other sources. Additionally, we have developed and included an algorithm to generate correlation estimates with equally weighted variance through the correlation record. While this approach is not applicable to follow the interactions of transients (or non-stationarities) in two data sets, it is useful in revealing the presence of periodicities.

We have found this software to be useful in investigating the properties of various expressions of random noise. In addition, the numerous analyses available and ease of use make this software an excellent instructional tool in both laboratory and classroom settings.

Finally, our software is coded in a widely available software package (LabVIEW^{TM} from National Instruments^{TM}). Hardware interfaces for this software are also available from NI, with both this hardware and LV software commonly used in laboratories throughout academia and industry.

Improvements for Our Software Package

Some aspects of our software could be improved to increase usability. Currently, the data analysis is restricted to the importation of binary files formatted for our LV routine. The data collection side automatically formats these files, but many users may have their own previously collected files they would prefer to analyze. An increase in the types of analyses available would also be beneficial.

Current Uses for PAASv1

At the present time, PAASv1 is being evaluated for use in various experimental and clinical settings. At the University of California - San Francisco, Dr. Chris Barton is evaluating PAASv1 in order to assess its utility as a replacement for the original program he developed. At East Carolina University, PAASv1 is being used for the experimental interrogation of calcium transients traveling from cell-to-cell in cultured stem cells. The goal is to verify and quantify the development of cell communication via gap junctions at the cells mature into myocytes. Finally, also at ECU, PAASv1 is being used to collect high-fidelity proximal and distal coronary artery pressure recordings across vessel lesions in the clinical cardiac catheterization laboratories at the time of stenting. The goal is to establish a more rigorous quantification of lesion hemodynamics in order to better define therapeutic strategies.

PAASv1 was also used to provide a system analysis of the dynamic afterload as presented in Chapter 4. The averaging methods employed in the software enabled an average impedance spectrum from multiple waveforms to be determined in an efficient manner. Along with the impedance spectra, coherence plots were generated by PAASv1 and presented as part of the dynamic afterload analysis.

Conclusion

In this software, we have combined data collection and data analysis in a single package. The EV implementation of the discrete correlation and spectral algorithms provides advantages in noise reduction for stationary signals which contain uncorrelated noise. Our program is currently being used for signal acquisition and analysis in laboratory settings;

however, the easy-to-use LV interface and the ability to retrieve and test numerous types of

signals also make the system an excellent instructional tool. This software has broad

research applicability as a tool for collection of electrical signals, data analysis and

evaluation of the characteristics of random inputs for system description.

CHAPTER IV

DESIGN AND IMPLEMENTATION OF A FLUID-MECHANICAL DYNAMIC AFTERLOAD FOR USE IN AN ISOLATED HEART APPARATUS

A fluid-mechanical afterload system was developed that incorporates dynamic control of resistance, compliance and volume adjustments. Design of the mechanical portion of the afterload is acceptable for attachment to an existing Langendorff heart apparatus. Digital controls for the afterload are enacted to reduce the difference between the mean and range values of a reference pressure and the measured pressure input. The system is able to match these mean and range characteristics within ± 5% for ten reference pressures within a realizable physiologic range. System settling time is less than 60 cycles (typically 45 – 50 cycles). The mechanical afterload is modeled by a four-element windkessel-type impedance, and estimated afterload parameter values fall within a physiological range. Effects of changing impedance on the mean, range and stroke volume follows anticipated trends. The dynamic afterload we developed exhibits the qualities necessary for implementation with an isolated heart apparatus.

Introduction

More than a century ago, Oscar Langendorff introduced his Untersuchungen am uberlebenden Saugethierherzen ("Investigations on the surviving mammalian heart").[6, 107] The ability to maintain a living mammalian heart (*ex vivo*) produced a major milestone in

cardiovascular research, enabling extensive studies of the contractile and electrochemical

properties of the myocardium. For several decades, researchers attempted to improve upon

Langendorff's system by developing a working heart model. Such a model would add to the

Langendorff apparatus by introducing a fluid backpressure (afterload) to a preloaded left

ventricle at the aortic output. The afterload would force the ventricle to work by requiring it

to eject its volume of blood against a mechanical impedance. A working, isolated heart

model would provide a mechanism by which to study not only contractile and

electrochemical properties of the myocardium, but also pressure and flow within the heart

chambers and myocardial properties that were dependent on ventricular load. In the 1960's,

Schreiber, Neely and Morgan et al. [7, 8] published their findings on heart function using a

working model of the isolated heart. Neely's model was a simple backpressure without any

attempt to isolate the components of the ventricular afterload. In the late 60's and early 70's,

Westerhof et al. [11] furthered the working heart model by constructing a mechanical afterload

with adjustable in-line resistance and an air-pressure compliance chamber. This afterload

enabled studies of myocardial energy expenditure, aortic pressure (AOP) and aortic flow

(AOF) changes under various loading conditions. [35] Ever-increasing computational power

soon allowed researchers, such as Westerhof et al. [16] and Suga and Sagawa et al., [12-14] to

control more precisely the isolated afterload components and the ventricular preload.

In the last decade of the 20th century, several components of modern artificial circulatory

apparatus were developed. Controlled displacement pumps for simulation of physiologic

flow[24, 27, 28] and mechanical ventricles [25, 27, 28] were engineered. Increasingly accurate

pressure and flow sensors, combined with improving computer, video and data acquisition

capabilities, enabled researchers to construct more sophisticated versions of the working

heart. Such a system, employing an artificial ventricular sac, is described by Gao et al. [31] [32]

A hybrid, electro-hydraulic heart and circulatory impedance simulator has also been

proposed by Kozarski et al. [108, 109] Additionally, an isolated four-chamber working swine

heart preparation with video capabilities was developed by Chinchoy et al. [33]

(http://www.visibleheart.com/background.html).

Currently, working heart apparatus are available commercially from companies such as

ADInstruments and Radnoti Glass Technology Inc., (http://www.adinstruments.com/),

QuantaMetrics (http://quantametrics.com/exp-prod05b.htm), and Harvard Apparatus

(http://www.harvardapparatus.com/). With these systems, researchers can study numerous

indicators of cardiac function under a variety of afterload conditions.

Past working heart apparatus have their advantage in straightforward construction and

hands-on manipulation of afterload parameters. Modern working heart devices have the

benefit of turn-key applications with numerous input and output permutations and extensive

data collection capabilities. At least one aspect of the working heart system, however, has

not been insufficiently addressed by past and current models, the dynamic nature of the

afterload manipulation. Most models provide static components for control of individual

afterload parameters (resistance and compliance). Other devices (e.g. ADInstruments

working heart setup), provide little control over the individual components of the afterload.

Dynamic afterload resistance control was demonstrated by Fisher et al. [34] while attempting to

maintain a physiologic pressure using a three-element afterload similar to that proposed by

Westerhof. [11] Fisher's system employed calculations for the desired resistance based on the

measured pressure and calculated flow. This control did not extend to the compliant element

of the afterload, and dynamic control of neither resistance nor compliance has not been developed for any of the other aforementioned devices.

A dynamic afterload provides an automatic method to direct pressure and flow waveform outputs. The pressure and flow outputs from the heart (as with any fluid system) reveal what conditions the ventricle is experiencing upstream (preload) and downstream (afterload). Elzinga and Westerhof and others have demonstrated that arterial impedance changes alter AOP and AOF waveforms in predictable ways. [14, 35, 36, 38] Researchers have shown that a number of pathophysiological states are characterized by directional afterload changes;[3, 40, 43] furthermore, impedance values are provided for several of these conditions. [11, 44, 70, 77, 110] In most of the reported studies, afterload changes were carried out in larger fractional steps. For instance, for the first trial of an experiment, the working heart system is set against a constant resistance value. Then, for subsequent trials, the value of systemic resistance is increased and held constant at two or three times the initial value. As a consequence of this protocol, a settling time is required for the heart to adjust to the new afterload and intermediate values are not considered. While this approach is suitable for understanding overall trends of AOP and AOF changes with arterial impedance adjustments, afterload changes within the body occur over a longer period and in a more continual fashion. In addition, changes in compliance occur within each beat during expansion and subsequent recoil of the larger arteries. [111-115]

Our goal for the dynamic afterload is to provide a continuously adjusting load for a pulsatile fluid input whereby a given mean and range of pulsatile pressure can be achieved. This afterload will eventually be employed with an isolated porcine working heart previously used in our laboratory to study the electrophysiology of cardiac arrest, [91] thus we must

provide physiologically appropriate loading conditions. We demonstrate that the afterload

we designed provides dynamic impedance adjustments to meet the mean and range

requirements for a given set of pulsatile flow inputs. Furthermore, this afterload provides

impedance values in a physiologic range and can be modeled with a four-element

windkessel.

Methods

Overview of Design Plan

We have developed and have previously published a computer model of AOP and AOF

waveform changes with impedance parameter adjustments (SAVIAv1). [45] This model was

used to guide the decision-making steps for impedance adjustments in the final afterload

control program. Simulations from the model were also used to verify that the behavior of

our physical afterload was similar to that of a four-element windkessel.

Impedance spectra from pressure and flow outputs were used to demonstrate the range of

the afterload parameters for our system and to verify that our system can be modeled by a

four-element windkessel. From Bendat and Piersol [93] we assume that, for a stationary

system, an unbiased estimate of the impedance spectrum with reduced noise can be generated

using auto- and cross-spectral estimates of the two signals, averaged over several segments.

$$\left| \hat{Z}_{xy} \right| = \left| \frac{\hat{G}_{xy}}{\hat{G}_{xx}} \right| \qquad\qquad 1$$

where x represents flow, y represents pressure, (^) represents an estimate, $|Z_{xy}|$ is the

magnitude of the impedance estimate, $|G_{xx}|$ and $|G_{xy}|$ are the magnitudes of the auto- and

cross-spectral estimates respectively.

We have developed and have previously published a program that can generate the impedance spectrum from auto- and cross-spectra obtained using averaging methods (see Chapter 3 manuscripts submitted for publication).

Our system is designed to receive fluid input (from a heart or other pump source) into an afterload with resistance, compliance and volume control elements. Pressure and flow data are obtained and the pressure is compared to a reference pressure. Adjustments are then made in the afterload elements in order to reduce the error between the reference pressure values and the measured pressure values. The dynamic nature of the adjustments for the fluid afterload requires controlling hardware and software within a feedback loop. In addition, if the fluid afterload model is to be widely employed, efficiency and cost-effectiveness are a must. Figure 4.1 provides an overview of the system layout.
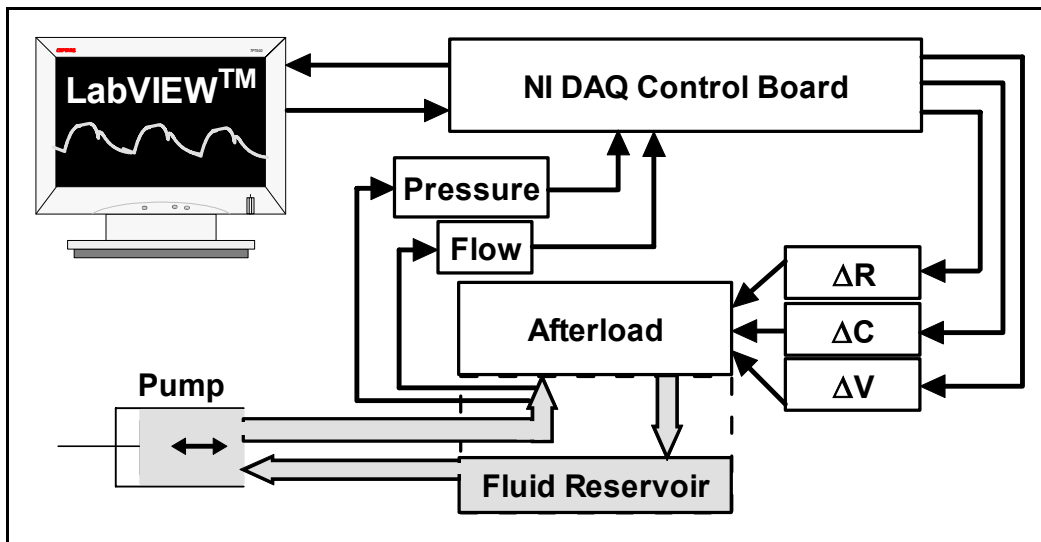
Figure 4.1 Afterload Control System Diagram. The control system (programmed in LabVIEW^{TM}) drives changes in the afterload R (resistance), C (compliance) and V (volume) to reduce error between the measured pressure and the reference pressure.

The NI DAQ hardware consisted of a terminal block connected to the computer through a DAQCard 6062E PCMCIA card. The pump in Figure 4.1 is a Respiration Pump (Model no. 607, Harvard Apparatus Co. Inc., Holliston, Mass.). This pump provides a very basic plug flow that is modified with the afterload parameter changes.

Afterload Design

The physical components of the afterload consist of a fluid inlet, a chamber to receive fluid input, a fluid outflow path to a proportional valve, a compliant end cap, and a volume adjustment balloon connected to air inflow. All components in contact with the fluid are constructed of clear acrylic (main chambers), latex (end cap and balloon) or biocompatible plastic (inlet and outlet tubes). The afterload rests on top of the Langendorff case, and fluid enters from the bottom. Figure 4.2 illustrates the components of the afterload [Note that this is a conceptual layout where components are placed to allow optimal viewing].
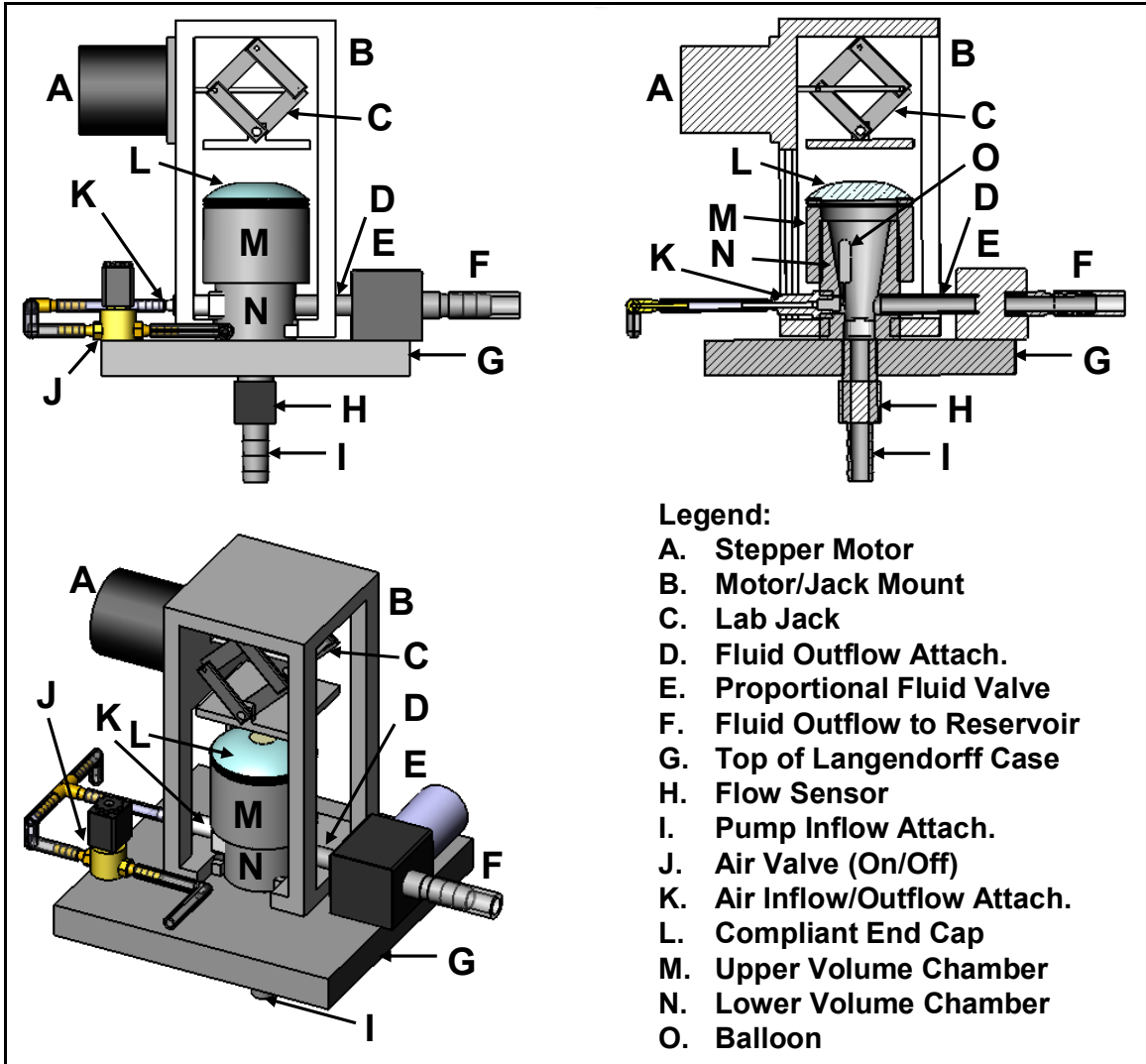
Figure 4.2 Afterload Design. Three views of the conceptual afterload layout are provided. Definitions for each component are provided in the figure legend (bottom right).

The following description of the afterload refers to Figure 4.2. The main chamber was designed as a two-part cylinder, threaded to allow coarse volume adjustment. The lower chamber (part N) was tapered to reduce wave reflections and turbulence that could occur from a large step increase in diameter. This lower chamber receives the fluid input through the pump inflow attachment (part I) that is threaded through the top of the Langendorff case (part G). A portion of the pump inflow attachment is flexible tubing. A fixed constrictor

was placed on this portion to provide an increase in characteristic impedance. Before the pump inflow attachment, a one-way fluid valve was inserted to reduce ringing from pressure wave reflections (addressed subsequently in *Discussion*). The fluid exits the main chamber through an outflow attachment (part D) connected to a proportional valve (part E, 12V standard proportional control valve, hard anodized aluminum Teknocraft Inc. Melbourne, Florida). The proportional valve is used to adjust resistance, and fluid exits from the proportional valve through an outflow port (part F) to a fluid reservoir. A latex balloon (part O, size 16 (3ml)), present within the lower chamber, is connected to an air inflow/outflow attachment (part K). The upper chamber (part M) has a compliant latex end cap (part L) of 0.010 – 0.025 inch thickness. This end cap is adjustable through contact with a lab jack platform (part C) that is raised and lowered by a stepper motor (Size 28, 5V, 3.6Ω, 7.5° per step, Hansen Corp., Princeton, IN. part A). The lab jack and stepper motor are mounted (part B) to the top of the Langendorff case. A Transonic Systems ME13PXN inline flow sensor (Part H) coupled with a TS410 flow meter (Transonic Systems Inc., Ithaca, NY) records the flow at the pump inflow attachment. The pressure is measured just above the flow sensor using a 5 French MPC-500 Mikro-Tip® pressure transducer (Millar, Houston, TX). The airflow in and out of the balloon is regulated by a 3-way on/off valve (part J, Teknocraft Inc. Melbourne, Florida).

Design Specifications and Calibrations

   Details of the afterload component dimensions and calibrations can be found in the *Appendix*. The main chamber was constructed to provide a volume range of approximately 135 – 250 ml. Coarse volume adjustments are enacted by raising or lowering the threaded

upper chamber. Volume adjustments during an input cycle are facilitated by coupling a

compliant end cap with a latex balloon that is pressurized briefly to 4-5 psi. The small

volume adjustment of the balloon was implemented as an optional aid for producing

sufficient backflow, which is usually provided by the expansion and recoil of the proximal

aorta. The volume adjustment balloon is triggered to inflate through the on/off valve.

Resistance within the afterload system is mainly generated by the proportional control

valve and a parallel tube line to the reservoir from the fluid outflow attachment. Calibrations

performed with the proportional valve (see *Appendix*) demonstrated a range of approximately

$0.5 - 4$ mmHg s ml^{-1}, which is in agreement with published physiologic values. [11, 35 43 116 60]

The resistance of the proportional valve was dependent on both the voltage applied and the

pressure at the input. Calculation of the resistance estimates that are provided in the results

(Figures. 4.6 and 4.7) was based on these calibrations for the resistance values over a

physiologic range of pressures. Resistance for pressures that fell between or beyond these

values was determined by a weighted average of the resistance values at the adjacent

pressures.

Compliance for the afterload system is provided in large part by the compliant end cap on

the upper chamber and to a lesser degree by the volume adjustment balloon within the main

chamber. A range of compliance from $0.5 - 4.0$ ml mmHg^{-1} was desired to remain within the

range of published physiologic values. [11, 60, 67, 111, 116] Several factors affect the compliance of

the end cap in our system, including the thickness of the latex sheet (typically 0.025 inch

thick), the degree to which the latex is stretched over the end of the upper chamber, the

position of the lab jack platform, the compression level of the springs in the lab jack, and the

inflation level of the small balloon. Reliably calibrating for each of these variables would be

extremely difficult. Therefore, our calibrations consisted of determining that we could achieve a physiologic range for various positions of the lab jack platform based on changing pressure and volume within the chamber (detailed in the *Appendix*). Using a 0.025 inch thick latex sheet, the range of compliance was approximately 1.75 – 2.25 ml mmHg^{-1}, well within the physiologic range. Varying other parameters (e.g. latex thickness, amount of stretching) can expand the range to meet other physiologic values. Compression of the end cap by the lab jack platform enables adjustment of the compliance both between and within cycles. Adjustment of the lab jack platform is made in a sinusoidal manner within each cycle – first to a higher position and then returning to the lower position. With a compliant system receiving pulsatile pressure input (e.g. the aorta), the compliance will drop as the pressure spikes. [113] An adjustment in the position of the lab jack platform is necessary to reduce the stiffness of the system as the pressure spikes. The lab jack platform is raised or lowered by a threaded rod turned by a stepper motor. At least a quarter turn of the threaded rod is required to provide significant movement of the jack platform, and this quarter turn must be made in a rapid manner within each cycle. Therefore a stepper motor with a larger degree per step was used (48 steps per revolution). Compliance estimates for the sample cycles shown in Figures 4.6 and 4.7 were made by using a variation of the pulse pressure method (PPM). Instead of calculating the differential equation for each step over the pressure waveform, the differential equation is solved for compliance (equation 2) and the mean value of pressure is substituted for the value of pressure.

$$\hat{C} = \frac{SV}{PP} - \frac{dt}{PP} \frac{\bar{P}}{R} \qquad\qquad 2$$

The ratio of stroke volume to pulse pressure tends to overestimate the compliance, [117] and our method subtracts the term based on the mean pressure to offset this overestimation. The

values for compliance calculated in this manner are only used as a rough estimate of

compliance for each cycle.

Afterload Adjustments Within Each Cycle and Between Cycles

An example of a single cycle is illustrated and labeled in Figure 4.3 to demonstrate the

timing of the afterload adjustments within each cycle and between cycles.
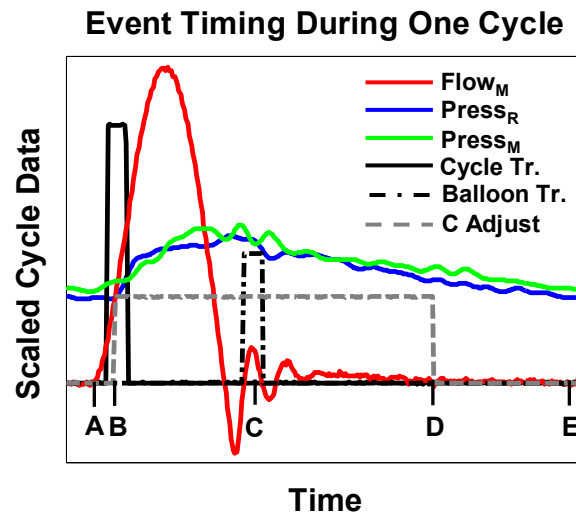
Figure 4.3 Timing of Events During a Single Cycle. Subscripts ($_R$ and $_M$) represent
reference and measured values respectively. The trigger for the cycle and the balloon is
abbreviated (Tr.), and compliance adjustments are termed (C Adjust). Positions within the
cycle are denoted by the letters A - E along the horizontal axis.

At the start of the flow input from the pump (position A in Figure 4.3), the cycle is

triggered. Triggering of each cycle is currently based on a roller switch mounted on the

respiratory pump. The adjustment period for the lab jack platform (compliance adjustment

within the cycle) begins shortly after the trigger (position B to position D in Figure 4.3).

Inflation of the balloon is enacted by briefly connecting to the pressurized air through the

on/off valve. This inflation occurs once per cycle, at a point near the dicrotic notch location

of the template waveform (position C in Figure 4.3). During the cycle, resistance voltage is

not varied and resistance changes slightly based on pressure. Resistance values are adjusted

after each cycle (after position E) by varying the voltage applied to the proportional valve.

At the end of each compliance adjustment period (position D in Figure 4.3), the level of the

jack platform can be raised or lowered to a different home position. This allows compliance

to be increased (when the jack platform is raised) or decreased (when the jack platform is

lowered).

Control System Design

The digital control system for the afterload was programmed in LabVIEW^{TM} 7.1.

Guidance for directional afterload changes to produce optimal impact on pulsatile pressure

characteristics was determined from simulations with SAVIAv1. The main characteristics of

pulsatile pressure are the mean and range, and, for an isolated working heart, the timing of

the dicrotic notch associated with reverse flow is also an important consideration. A control

system was implemented where resistance changes control the mean and compliance changes

control the range of the pulsatile pressure. The timing of the reverse flow is aided by balloon

volume changes within each cycle. Measured pressure (P_M) is compared with a reference

pressure (P_R) near the end of each cycle, and adjustments are made in the afterload elements

based on how well the mean and range of the two waveforms match. A flow chart is

provided in Figure 4.4 to illustrate the logic of the digital controller.
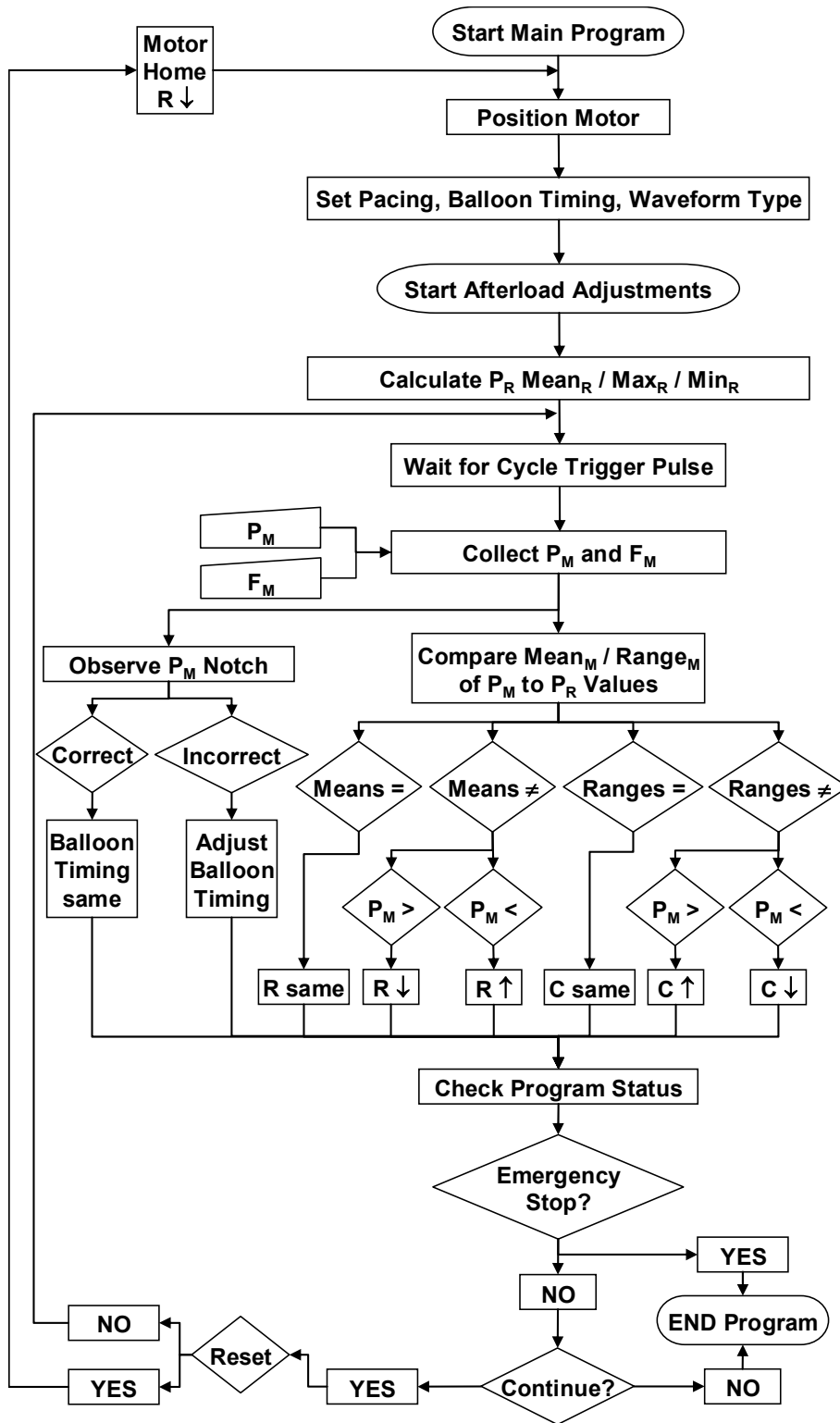
Figure 4.4 Flow Chart Describing the Digital Control Logic. Subscripts denote reference ($_R$) and measured ($_M$) values. R and C represent resistance and compliance respectively.

A ± 5% error from the reference pressure in mean and range values is allowed. The level of adjustment for resistance and compliance after each cycle is set to provide a smooth approach to the reference values. Some overshoot is allowed to avoid lengthy settling times. Changes in the voltage to the proportional valve (providing changes in resistance) are implemented in the following manner. For the first 15 – 20 cycles, adjustments are made at the 0.25 V level. At this point, the system is approaching the desired mean, and the adjustment level is dropped to 0.025 V. The number of initial cycles included at the 0.25 V adjustment range can be adjusted depending on the step increase in mean pressure applied by the reference pressure. An interaction occurs between adjustments in resistance and adjustments in compliance as the system approaches the mean. As the mean pressure increases toward the goal, the range, and subsequently the compliance adjustments are continuously changing. If the system approaches the mean too rapidly, the compliance adjustments to ease the pressure on the latex end cap may not occur rapidly enough and the system could rupture. For this reason, the adjustments in resistance are made at a somewhat slower pace, and the settling time for the range values always lags behind the settling time for the mean. A four-step adjustment can be made after each cycle to raise or lower the lab jack platform as necessary. The level of compliance adjustment is affected by several factors: the resolution of the stepper motor, the thread pitch on the lab jack platform arm, the pacing of the pulsatile pressure input. For this reason, adjustments of compliance within each cycle are limited to a sinusoidal stepping of 16 or 24 steps. These values provide optimal changes for most of the pacing values used. Timing of the dicrotic notch is adjusted (within an allowable range) by using a slide adjustor within the controller code. An

emergency stop button was implemented to raise the lab jack platform and minimize resistance in case of a system malfunction.

Data Analysis and Modeling of the System

Simulations were performed with ten different types of AOP waveforms used as the reference pressure. These pressures were of a variety of mean and range values that were relevant physiologically. Included in the different reference pressure types were AOP waveforms representative of certain normal and pathophysiological conditions (e.g. aging, heart failure, ventricular septal defect). The simulation data were collected at 256 samples/sec and analyzed using Matlab®. Each simulation consisted of 100 cycles and was repeated five times under similar conditions. The data were filtered by convolution in the time-domain with an ideal low-pass filter [118] centered at zero with a cutoff frequency of 20 Hz. The bandwidth (BW) was used to approximate the number of points (M) in the filter as $BW = 4/M$. From each simulation, a coincident and consistent segment of measured pressure and flow (F_M) was chosen after the mean and range had settled. This data segment was typically 3-5 cycles in length. The measurement of pressure was approximately 5cm from the measurement of flow; therefore, assuming a rigid tube, the pulse wave velocity is fast enough to eliminate the need for a time delay correction between pressure and flow measurement. [119] The 3-5 cycle segment was resampled using a Matlab® FIR resampling algorithm to provide 256 samples per waveform. The mean, range and stroke volume (SV) were determined for P_M within this segment. Values for the mean and range were averaged from the five simulations and compared with the mean and range of P_R. For each data segment, an impedance spectrum was generated from P_M and F_M data using a Matlab®

version of PAASv1 (see Chapter 3). This method uses an average of the cross-spectrum over the number of cycles. Values of the cross-spectrum with a low coherence (typically 0.4 or less) were eliminated. The remaining values were fit to the impedance modulus for a four-element windkessel model using a Levenberg-Marquardt algorithm with a tolerance of 1E-6. Values for the impedance parameters were averaged from the five simulations. An illustration of the four-element model is shown in Figure 4.5, and the equation for the impedance modulus ($|Z_{4E}|$) for this model is given in equation 3. This electrical analog model corresponds well with the physical layout of our fluid-mechanical system. The Z_o resistor represents the characteristic impedance of the afterload, which is mainly governed by the pump inflow attachment leading to the main chamber. The Z_I inductor represents the inertance of the fluid, which is provided by the column of fluid to be accelerated through the pump inflow attachment during each cycle. The capacitor (C) represents the compliance of the system, provided by the latex balloon and end cap. The resistor (R) represents the resistance generated by the proportional valve. To illustrate the suitability of the four-element model for this system, flow and pressure pairs were generated using the four-element model in SAVIAv1. The F_M from a data segment from one simulation was used as input and the impedance parameters were estimated for that same simulation segment as the model impedance parameters. The model's output pressure (P_{MOD}) was then compared with P_M. Two examples of the data analysis, including an illustration of mean and range settling time, are shown in Figures. 4.6 – 4.8.
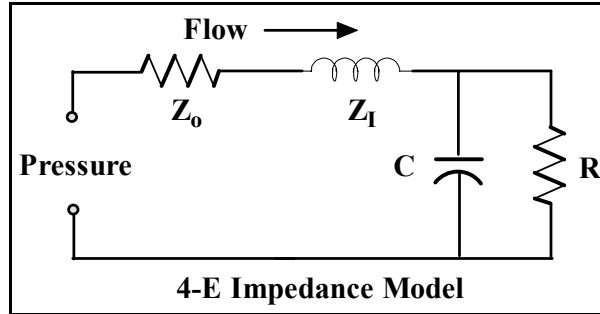
Figure 4.5 Four-element Impedance Model. Z_o is the characteristic impedance. Z_I is the inductance (inertance). C is the capacitance (compliance), and R is the resistance.

$$|Z_{4E}| = \frac{1}{1+(\omega RC)^2} \sqrt{\left(\omega Z_I\left(1+(\omega RC)^2\right) - \omega R^2 C\right)^2 + \left[R + Z_o\left(1+(\omega RC)^2\right)\right]^2} \quad 3$$

Averaged values from the P_M waveforms and reference values from five selected AOP (P_R) inputs are provided in Table 4.1. When considering settling time, the step input of mean pressure (Δ Mean) was the only meaningful value. The change in the mean of the measured waveform was always unidirectional and the range is affected by the increase in proportional valve resistance until the system is close to settling around the mean. For example, the starting range difference between P_M and P_R could be relatively small (10 mmHg or less), but by the time the mean is increased to an appropriate level, the difference in range may have increased. This means that the settling time for the range denotes the system settling time, as the mean settles more quickly.

Plots of mean, range and SV with changes in resistance and compliance were generated using data from all ten types of AOP (P_R) waveforms. The mean value of P_M is a dc value, thus resistance is the main factor affecting the mean. However, both resistance and compliance have some affect on the range and SV. To demonstrate the changes in range and SV with increasing system impedance, we employed a two-element windkessel impedance

(resistance and compliance in parallel) using the impedance values for resistance and compliance estimated from the four-element model. Values of range and SV were plotted against this impedance at 1, 2, and 4 Hz.

Results

An example of the simulation results and data processing from the Type 1 P_R (Table 4.1) is given in Figure 4.6. The analysis was carried out for the four cycles shown in Panel A. Adjustments in resistance that drove the P_M mean to settle at the mean of P_R are illustrated in Panel B. Settling time for the mean was slightly less than 40 cycles. The necessary increase in range was enacted by decreasing compliance (Panel C). Since the range is a difference signal and our system was not free from noise, the signal representing the range was low-pass filtered at 1 Hz cutoff to enable a reasonable observation of the range settling time (approximately 40 cycles). Note that increases in resistance produce increases in the mean and decreases in compliance produce increases in the range as predicted. Panels B, D, and F provide the spectral analysis of the data segment. In Panel B, the impedance spectrum is generally well-matched by the estimate from the four-element impedance model. Parameter values for the impedance are all within the range of physiologic values. In the phase plot (Panel D), the phase difference is underestimated for most of the plot. At lower frequencies (< 5Hz), the shape of the phase estimate conforms well to the measured phase, and at high frequencies (> 10Hz) the phase approaches a $\pi/2$ phase difference. Difficulty in estimation is more apparent in the 6-9 Hz frequency range. From the coherence plot (Panel F), the simulation has a noise source affecting the signal from 7-9 Hz. This unwanted noise produces inconsistencies in the signal that make it difficult to estimate the values of

impedance at these frequencies (addressed subsequently in the *Discussion*). Above 18 Hz,

the coherence drops to negligible values, and these points are not included in the impedance

estimation.

Processing Example From Type 1 Reference Pressure
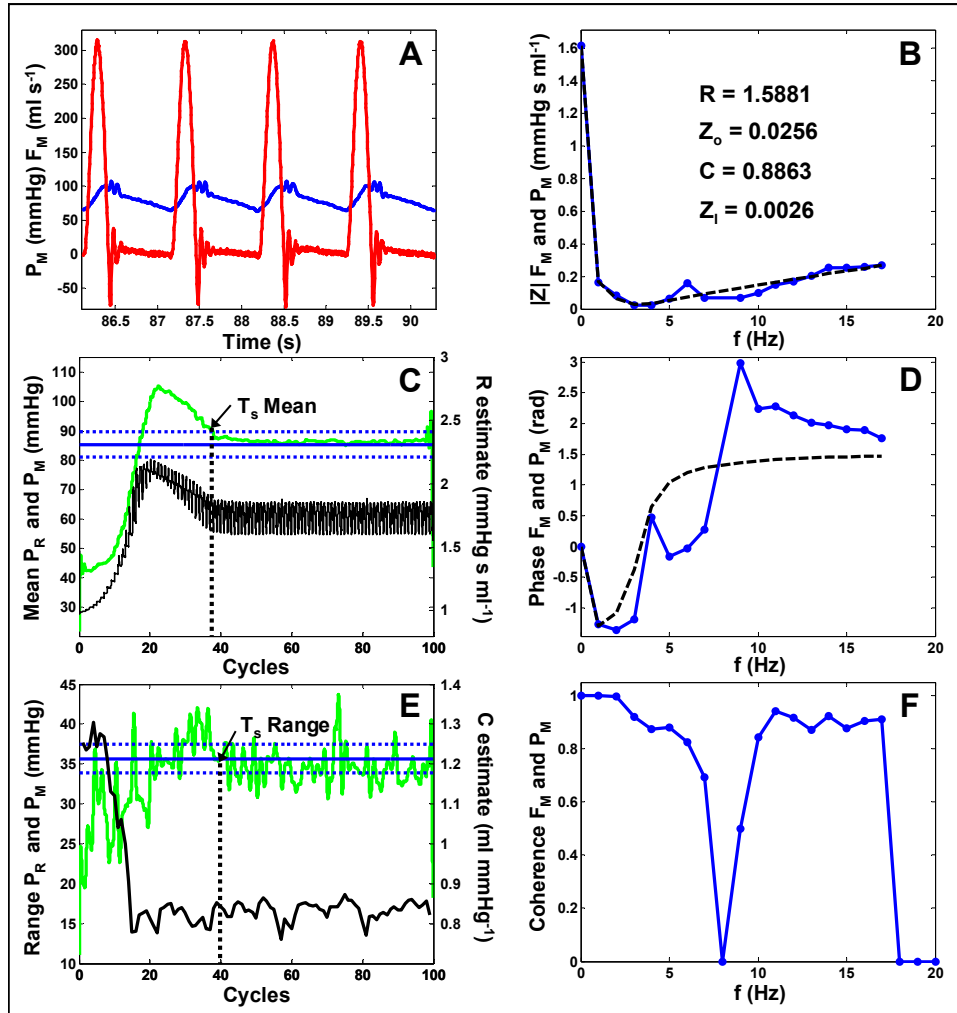
Figure 4.6 Sample Data Analysis for Type 1 P_R. Panel A shows the three cycles of P_M (blue) and F_M (red) that were analyzed. The P_R mean and range (+/- 5% blue) and the mean and range for P_M (green) are illustrated in Panels C and E respectively along with settling time (T_s) approximations. An estimate for R over the course of the simulation is provided in Panel C (black), and a similar estimate for C is provided in Panel E (black). In Panel B, the impedance modulus (|Z|) for F_M and P_M is shown (blue) with the estimated impedance generated for the four-element model (black dashed). Units for the parameters are R and Z_o (mmHg s ml^{-1}), C (ml mmHg^{-1}), Z_I (mmHg s^2 ml^{-1}). In Panel D, the phase for F_M and P_M (blue) is presented with the estimated phase for the four-element model (black dashed). Panel F shows the coherence for F_M and P_M.

Figure 4.7 shows a simulation example and the data processing results from the Type 3 P_R (Table 4.1). For this example, the analysis was carried out for three cycles (Panel A). Adjustments in resistance that drive the P_M mean to settle at the mean of P_R are illustrated in Panel B. Settling time for the mean was approximately 35 cycles. A decrease in compliance caused an increase in the P_M range (Panel C), where the range signal was low-pass filtered at 1 Hz cutoff. Settling time for the range was slightly less than 40 cycles. The four-element estimate of impedance matches well with the calculated impedance (Panel B), and the parameter values are within the physiologic range. For this simulation, the phase plot (Panel D) is estimated more accurately than the phase estimate shown in Figure 4.6. At lower frequencies (< 5Hz), the shape of the phase estimate is reasonably conformed to the measured phase, and at high frequencies (> 10Hz) the phase approaches a $\pi/2$ phase difference. The estimate for phase still maintains problems in the 6-9 Hz frequency range where the coherence falls (Panel F). However, the coherence drop is not as sharp as that seen in Figure 4.6 Panel F, and the model estimated phase is not as far from the true phase. Above 18 Hz, the coherence drops to negligible values, and these points are not included in the impedance estimation.

Processing Example From Type 3 Reference Pressure
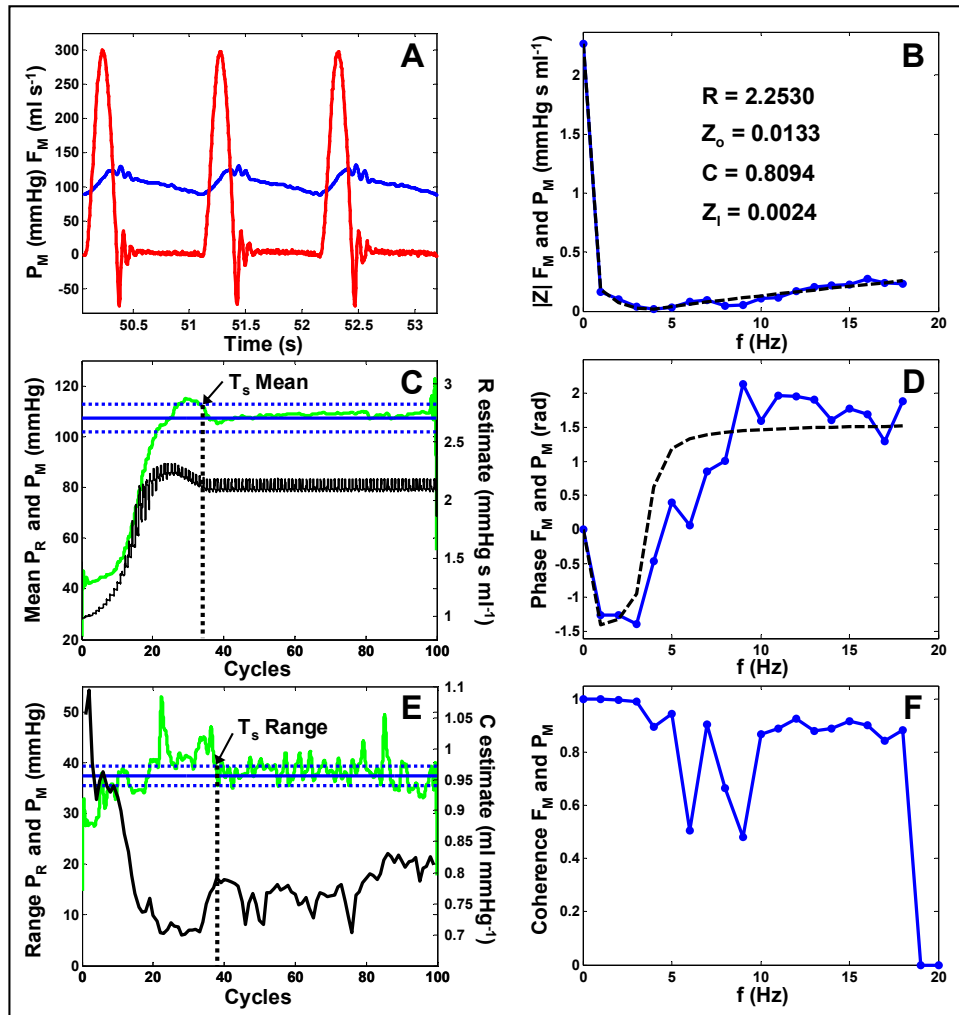
Figure 4.7 Sample Data Analysis for Type 3 P_R. Panel A shows the three cycles of P_M (blue) and F_M (red) that were analyzed. The P_R mean and range (+/- 5% blue) and the mean and range for P_M (green) are illustrated in Panels C and E respectively along with settling time (T_s) approximations. An estimate for R over the course of the simulation is provided in Panel C (black), and a similar estimate for C is provided in Panel E (black). In Panel B, the impedance modulus ($|Z|$) for F_M and P_M is shown (blue) with the estimated impedance generated for the four-element model (black dashed). Units for the parameters are R and Z_o (mmHg s ml^{-1}), C (ml mmHg^{-1}), Z_I (mmHg s^2 ml^{-1}). In Panel D, the phase for F_M and P_M (blue) is presented with the estimated phase for the four-element model (black dashed). Panel F shows the coherence for F_M and P_M.

Figure 4.8 is provided as an adjunct to the data analyses shown in Figures 4.6 and 4.7. In this figure, the P_M from the Type 1 and Type 3 P_R simulations is plotted with P_R and the pressure generated from the SAVIAv1 model (P_{MOD}) using the estimated impedance

parameters. Panels A and C correspond to the Type 1 P_R simulation, and Panels B and D correspond to the Type 3 P_R simulation. The signals shown in Panels A and B are low-pass filtered with a cutoff of 6 Hz to demonstrate the low frequency characteristics of the waveforms. Though the timing is slightly delayed for measured pressure, the mean and the range shown in Panel A are very similar for P_M and P_R. Panel C illustrates that the main characteristics of P_{MOD} overlay properly with P_M, though some of the higher frequency components are lacking in the model waveform. In Panel B, P_M demonstrates a similar range to P_R, but the mean is elevated. As seen in Table 1, the mean was overestimated for this portion of the data, but it remained within the 5 % error tolerance. The model pressure waveform in Panel D demonstrates a reasonable match to P_M, with a slight underestimation of the mean and a lack of some of the higher frequency waveform components.

Measured Pressure Comparisons to Reference and Model
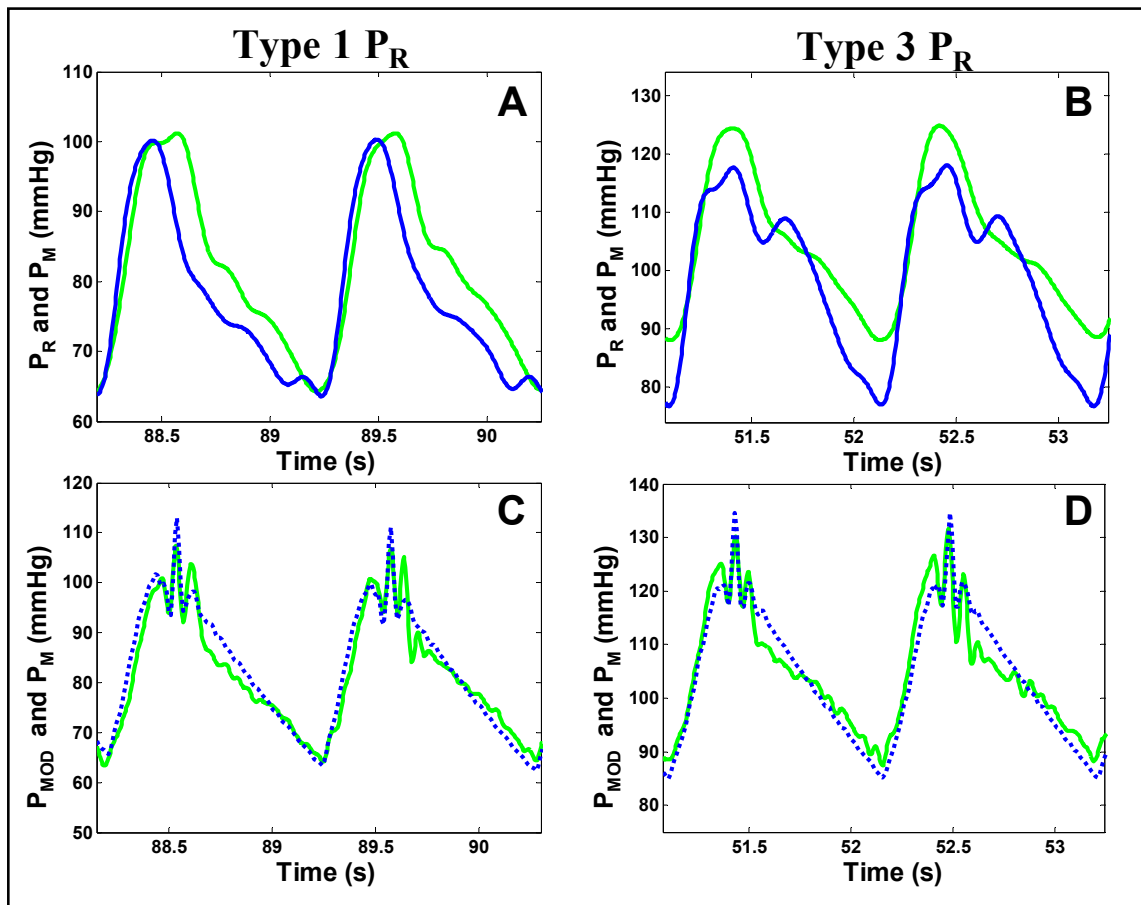
Figure 4.8 Simulation Pressure Overlaid with Reference and Model Pressures. Panel A shows low-pass filtered P_M (green) and P_R (blue) from the Type 1 P_R simulation provided in Figure 4.6. Model simulated pressure (P_{MOD} blue dashed) using the estimated impedance parameters for Type 1 P_R is shown in Panel C with P_M (green). Panel B shows low-pass filtered P_M (green) and P_R (blue) from the Type 3 P_R simulation provided in Figure 4.7. P_{MOD} (blue dashed) using the estimated impedance parameters for Type 3 P_R is shown in Panel D with P_M (green).

Table 4.1 provides simulation results from five selected types of AOP (P_R) waveforms. These simulations were performed with the following conditions: chamber volume (220 ml), latex tension (medium), pump rate (57 – 58 bpm), pump stroke volume (50 ml), air pressure (4 – 5 psi). Selection of the results was made based on waveforms with a variety of mean and range values to demonstrate our system capabilities. Reference values for the mean and

range were derived from the reference AOP waveforms. Averaged values for the measured

mean, range, SV and impedance parameters were obtained as described in *Methods*.

Table 4.1: Simulation Results from Selected Reference AOP Waveforms

	Type 1 AOP	Type 2 AOP	Type 3 AOP	Type 4 AOP	Type 5 AOP
AOP_R Mean	85.25	88.57	107.37	97.13	82.84
AOP_M Mean	85.20 ± 0.45	90.47 ± 0.29	110.88 ± 0.32	96.27 ± 0.58	84.27 ± 0.70
% Error Mean	- 0.05 ± 0.53	2.15 ± 0.33	3.27 ± 0.30	- 0.89 ± 0.59	1.72 ± 0.84
Δ Mean	34.09 ± 0.31	38.22 ± 0.16	56.70 ± 0.18	43.76 ± 0.26	32.28 ± 0.25
Ts Mean (cycles)	37.20 ± 0.49	34.00 ± 1.00	33.00 ± 1.30	28.60 ± 0.24	45.20 ± 0.20
AOP_R Range	35.66	44.70	37.38	63.87	19.94
AOP_M Range	34.85 ± 0.68	44.27 ± 1.32	37.62 ± 0.54	63.04 ± 0.56	20.61 ± 0.52
% Error Range	- 2.27 ± 1.92	- 0.95 ± 2.95	0.64 ± 1.46	- 1.29 ± 0.88	3.37 ± 2.58
Ts Range (cycles)	49.20 ± 2.96	45.60 ± 1.12	44.80 ± 1.98	39.40 ± 3.37	60.40 ± 1.75
SV_M	51.99 ± 0.12	51.10 ± 0.14	47.67 ± 0.15	46.28 ± 0.10	53.90 ± 0.13
R ± SE	1.5725 ± 0.012	1.6795 ± 0.008	2.2525 ± 0.015	1.8800 ± 0.018	1.5360 ± 0.015
Zo ± SE	0.0298 ± 0.005	0.0401 ± 0.004	0.0068 ± 0.002	0.1154 ± 0.006	0.0059 ± 0.001
C ± SE	0.9004 ± 0.023	0.7770 ± 0.019	0.7784 ± 0.014	0.5632 ± 0.013	1.6971 ± 0.090
Z_I ± SE	0.0026 ± 6E-5	0.0024 ± 1E-4	0.0026 ± 1E-4	0.0024 ± 3E-4	0.0025 ± 5E-5

Subscripts ($_R$ and $_M$) denote reference and measured values respectively.
Averaged values are provided with their standard error calculated for five simulations.
Units for pressure and range are (mmHg), and units for stroke volume are (ml).
Units for impedance parameters are R and Z_o (mmHg s ml^{-1}), C (ml mmHg^{-1}), Z_I (mmHg s^2 ml^{-1}).

The mean values for the measured waveforms given in Table 4.1 range from

approximately 84 - 111 mmHg, and the collection of range values is from approximately 20 –

63 mmHg. Accounting for all means and ranges shown, this equates to a total pressure range

of 65 – 130 mmHg (covering much of the physiologic range of pressure). Calculated percent

error is less than 5% in all cases shown, and the error for the other five reference AOP

simulations (not shown) was approximately 5% or less. P_M settled to the P_R mean value

within a range of approximately 28 – 45 cycles. The range of P_M required approximately 40

– 60 cycles to settle at the P_R range.

Trends for the measured mean, range and SV for all ten P_R types are shown in Figure 4.9.

Panel A illustrates that increasing resistance results in an increase in the mean of P_M, with an

R^2 value approaching unity. In Panel B, a trend of increasing range for P_M with increasing

impedance is evident. As the frequency increases from 1 to 4 Hz, the slope of the range data increases. The trend displayed for SV in Panel C is that increased impedance results in decreased SV. Calculated SV shows an increasingly negative slope as the frequency increases from 1 – 4 Hz.
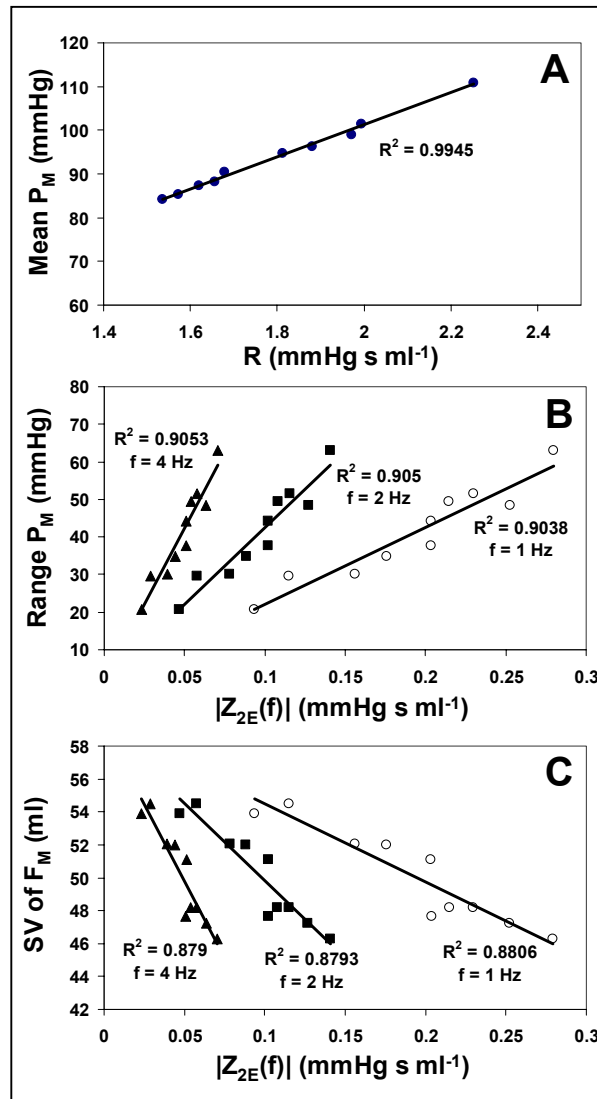
Figure 4.9 Changes in Mean Range and SV with Changes in Impedance. Panel A illustrates changes in the mean of P_M with changes in resistance. Panel B shows trends for the range of P_M with changes in the two-element impedance ($|Z_{2E}|$) at different frequencies. In Panel C, changes in SV (calculated from F_M) are shown with changes in $|Z_{2E}|$. For Panels B and C, the frequencies are f = 1 Hz (circles), f = 2 Hz (solid squares) and f = 4 Hz (solid triangles).

Discussion

Afterload Design

The design of the fluid-mechanical afterload is properly suited for ease of implementation and cost efficiency. The entire portion of the afterload pictured in Figure 4.2 can be placed on top of the Langendorff case (less than 1 ft^2), and none of the components represent an exorbitant cost.

Design Specifications and Calibrations

The volume of the chamber and the volume adjustment within each cycle are based on the rough approximation of a tapered aorta with an inner diameter of 1 – 3 cm [120] [114] and a length of 25 – 30 cm. The volume adjustment from the balloon is small, because there is typically only a small difference in diameter from diastole to systole during the cardiac cycle. [114]

Resistance and compliance values produced by the system were within a physiologic range (see *Appendix* and Figures 4.6 and 4.7). Estimates of resistance throughout the simulations demonstrated appropriate adjustments to compensate for the error in the mean pressure. The difference in range between P_M and P_R was compensated for by adjustments in the compliant end cap.

Afterload Adjustments Within Each Cycle and Between Cycles

The roller switch mounted on the respiratory pump (see *Methods*) provides a consistent starting point for each cycle. The timing and extent of the balloon inflation varies depending on the following: the location of the dicrotic notch within the P_R waveform, the number of steps within the cycle that the stepper motor undergoes, and the pressure within the chamber.

These issues are discussed further in *Limitations of the Proposed System*. Though the timing can be different over several cycles, the variation is only slight.

Changes in resistance within each cycle are apparent from the simulation results given in Figures 4.6 and 4.7. Most models hold resistance constant during the cardiac cycle as its main contributor (the peripheral vasculature) [60] is unlikely to undergo significant changes during such a brief period. However, in a fluid system where the main source of resistance is a single outlet in close proximity to the pulsatile pressure, the resistance will change slightly over the course of the cycle.

The timing of the increase in compliance during the peak pressure of each cycle was regular for all simulations. The nonlinearities associated with the compliance hardware had an effect on the stationarity of the data and the subsequent ability of our model to predict the impedance parameters. Consequences of the resistance change and compliance nonlinearities are discussed further in *Limitations of the Proposed System*.

Control System Design

Our control system was based on reducing the error in mean and range values between P_M and P_R (see Figure 4.4). Though some compliance adjustments occurred during each cycle, the data necessary for mean and range calculations could only be properly analyzed near the end of each cycle. This necessitated that major adjustments in resistance and compliance be made at the end of each cycle. Volume adjustments from the balloon were not made automatically by the code. Timing of the adjustments is based on the location of the dicrotic notch within the P_R waveform. This location does not change after the simulations start, and the timing can readily be adjusted by the user as the system settles.

From the sample simulations given in Figures 4.6 and 4.7 and Table 4.1, the afterload

adjustments enacted by the control system maintained the mean and range within the ± 5%

error limits. The settling time for each simulation varies, depending on the difference in

mean and range for which compensation must be made. As explained in *Methods*, this

settling time accounts for changes in resistance that affect changes in compliance. Thus,

some variation is to be expected with a wide variation in mean and range step values.

Overshoot for the mean and range values from the initial compensation stage was reasonable

for all simulations, and many simulations had minimal or no overshoot.

The control system, programmed in LabVIEW^{TM}, is not a real-time software application.

This imposed several restrictions on the speed and timing of adjustments in the afterload.

These restrictions are noted in *Limitations of the Proposed System*.

Data Analysis and Modeling of the System

The results shown in Figures 4.6 and 4.7 illustrate the ability of the dynamic afterload

system to drive a pulsatile pressure input generated by a basic plug-type flow to match the

mean and range of a reference pressure. Estimated values for the afterload parameters

necessary to accomplish these compensations are within the expected physiologic range.

Furthermore, the system can generally be characterized by the four-element impedance

model of Figure 4.5.

The impedance plots generated from F_M and P_M data segments are characteristic of the

impedance of a four-element electrical analog model with a series inductor. At higher

frequencies, the impedance of the parallel RC portion of the circuit will go to zero, because

the impedance of the capacitor is given by $(j\omega C)^{-1}$. The impedance of the inductor is given

by jωL, which means that the impedance of this portion of the circuit will increase with increasing frequency. Consequently, the inductor (inertance) will dominate the impedance as the frequency rises. As frequency values increase, the series inductor will also dominate the phase plot, driving the phase difference to $+ \pi/2$. The impedance of our fluid-mechanical system is dominated at higher frequencies by the inertance of the pump inflow attachment. This phenomena was discussed by Westerhof *et al.* in regard to the flow measurement attachment in their three-element mechanical afterload. [11] Unfortunately, for a fluid-mechanical system adapted for flow measurement and pulsatile pump input, this initial attachment and its resultant dominant inertance cannot be avoided. Our main concern in this system is to match the mean and range of the reference pressure, and these lower frequency waveform characteristics (as illustrated in Figure 4.8 Panels A and B) are less affected by the inertance.

For the Type 1 P_R of Figure 4.6, the step increase in mean pressure was approximately 34 mmHg (Table 4.1), and the system settled to $\pm 5\%$ of both mean and range reference values within 40 cycles (Panels C and E). A larger variation of the range value around the target range is apparent, due to the fact that the difference value representing range is greatly affected by noise present within the system. In spite of the noise, the general settling trend of the range value is evident. The impedance plots in Panels B and D of Figure 4.6 demonstrate that the four-element model of Figure 4.5 provides a reasonable estimate of the system, producing estimated parameters within the physiologic range. This estimate is reasonably accurate for frequencies < 4 Hz; however, for the middle frequencies (especially 6-9 Hz), the model underestimates the phase difference. As the frequency increases beyond 10 Hz, the measured phase tends to settle toward the model value of $\pi/2$. Noise and non-stationarities

within the measured signals (discussed subsequently) contribute to a lower coherence in these middle frequency ranges and create a reduction in the number of stationary waveforms over which the impedance spectrum can be averaged to reduce the noise. Therefore, the noise contribution to the phase is apparent in this middle frequency range and the estimate from the model is less accurate.

In Figure 4.7, the Type 3 P_R simulation reveals that the dynamic afterload system was able to settle within 40 cycles for a mean pressure step increase of approximately 57 mmHg (Table 4.1). The noisy range signal is again present (as in Figure 4.6), but the overall settling trend is apparent within the desired $\pm 5\%$ range. The impedance plot of Panel B shows a close fit of the four-element model to the actual measured impedance. All estimated parameters are within the physiologic range. A more accurate estimate of phase is achieved for this simulation (Panel D), especially at the middle frequencies, likely due to the higher coherence (Panel F) at these frequencies when compared to the same frequency range in Figure 4.6. A higher coherence would indicate that this simulation had less noise and non-stationary contributors in this frequency range than the simulation shown for the Type 1 P_R. In general, the phase is reasonably estimated at frequencies less than 4 Hz, and the phase settles to $\pi/2$ at higher frequencies.

An illustration of the actual waveforms generated from the simulations for Type 1 and Type 3 P_R is given in Figure 4.8. Low-pass filtering of P_M and P_R in Panels A and B was necessary to enable a clear view of the signals without noise. Also, removal of the higher frequency components focuses attention on the waveform characteristics that we were attempting to control (mean and range). The Type 1 simulation in Panel A shows a P_M that is well-matched in mean and range with P_R. A slightly delayed peak pressure and decay are

apparent in P_M. This timing issue is affected by the cycle timing from the respiratory pump, the output timing of the reference signal from within the LabVIEW^{TM} control code, and the characteristics of the pump itself. Since we do not have the actual heart (pump) that produced this reference waveform, and considering the fact that the other timing issues exist, the slight delay is not unexpected. Our SAVIAv1 model output (P_{MOD} in Panel C) uses the input F_M waveform from the Type 1 simulation and the four-element model estimated parameters from the same simulation. P_{MOD} in general overlays well with P_M, even predicting a good portion of the pressure spike located at peak pressure. The fact that P_{MOD} matches with the main characteristics of P_M reveals the suitability of the four-element afterload to describe our system. Though middle and higher frequency components may be lacking, the low frequency components of interest are properly captured by this model. The Type 3 simulation in Panel B shows a P_M that is well-matched in range with P_R but that has an elevated mean. Table 4.1 shows that the mean for this portion of the simulation was overestimated by about 3%; however, this is within the tolerated 5% error limits set in the control code. Output from the SAVIAv1 model (Panel D) almost completely compensates for this difference in mean, due to the higher estimated resistance value. Though the parameter estimate is not quite high enough to completely account for the necessary increase in mean pressure, the similarity of P_{MOD} mean and range does demonstrate that the model is satisfactorily describing the main characteristics of P_M mean and range.

Selected simulation results from five of the ten types of AOP (P_R) reference waveforms demonstrate the dynamic afterload's ability to drive a pressure match within physiologic limits. All mean and range values settled to well within the $\pm$ 5% error limits. That settling times varied significantly is not surprising considering the variety of mean pressure step

changes and reference range goals. In addition, the settling times were not unreasonable for

any simulation set. The impedance parameters estimated for each simulation are within a

physiologic range; however, the characteristic impedance proved to be a difficult estimate for

the model, especially for signals with lower coherence. Our physical setup has only a fixed

constrictor on the flexible tubing to regulate this impedance. This fact, when coupled with

the non-stationary pressure spikes present in the current setup (discussed subsequently)

contributes to the model's inability to consistently estimate this parameter. Other than the

characteristic impedance, the model estimates of impedance parameters were highly

consistent with trends that match with expected physical behavior (Figure 4.9).

Trends for estimated impedance parameters with changes in mean, range and SV are

illustrated in Figure 4.9. Panel A demonstrates that, as expected, the trend for increasing

resistance is an increasing mean P_M. In Panels B and C, the two-element impedance ($|Z_{2E}|$)

trends are shown. As explained in *Methods*, $|Z_{2E}|$ was used rather than simply resistance or

compliance because of the interaction of each in affecting range and SV. With higher

impedance, the range shows marked increases, and these increases have a larger slope at

higher frequencies. As the system's impedance increases, especially in terms of compliance,

the system will become stiffer and pressure will tend to rise and decay faster (higher range).

Panel C shows that, with increasing impedance, SV decreases. With higher impedance and

the same mean pressure, the pulsatile pressure input would be expected to generate less flow.

The decrease in SV is more marked as frequency values rise. For higher frequency values in

the two-element impedance model, the changes in resistance and compliance will have less

effect on the actual value of impedance because the increase in frequency is beginning to

dominate the denominator (equation 3). However, within the physical system these changes

still produce a similar increase in range or decrease in SV. Thus, the changes (slopes) increase at higher frequencies, because the same changes in range and SV occur over a narrower range of impedance values.

Results from the data analysis and selected simulations reveal that our dynamic afterload performs as anticipated, producing mean, range and estimated impedance values within physiologic limits. Considering the fact that we are attempting to shape a pressure waveform generated from a basic plug-type flow created by a crude pump, the behavior of our dynamic afterload system is certainly acceptable. When implemented with a compliant heart pump that will generate more reasonable AOP waveform characteristics, the results from our system should improve significantly.

Limitations of the Proposed System

Even though our dynamic afterload system generally performs as expected, there are several aspects of its behavior that provide limitations and leave room for improvement.

The resistance within the system is mainly provided by a single proportional valve with a larger inner diameter. As Westerhof *et al*. [11] discuss, this is not the ideal type of resistor for optimizing resistance and inertance in a fluid system. In addition, the behavior of the valve itself allows resistance to change slightly as a function of inlet and outlet pressures. Though the inertance of the main resistor may be higher than we would like, the inertance of the pump inflow attachment segment is much higher, and the inertance of this inflow segment dominates the impedance at higher frequencies. The behavior of the valve resistance with inlet and outlet pressures produces relatively minor fluctuations in resistance over a single cycle. Considering that our goal is not to match resistance, but rather to achieve a mean

135

pressure with adjustments in afterload, the changes within a cycle for resistance will have minimal effect on the overall system performance.

Compliance for the system is controlled by movement of the lab jack platform. The platform is of a standard makeup with some compressibility and oscillation likely at higher pressures due to the scissor arms and springs that extend the platform. With different extension levels for different compliance values, the compression and oscillatory effects of the jack platform differ for each simulation, and even within a simulation. The changing compressibility and oscillation of the lab jack platform are the main source of non-stationary and nonlinear effects within our system. This was evident for simulations where the lab jack platform had minimal contact with the end cap. For these simulations the coherence of the F_M and P_M waveforms was much higher in the middle frequency range. In addition to noise contributions from the lab jack platform, noise sources in our data collection system produced fluctuations in the pressure waveforms. This noise directly affects the estimation of the pressure range on which the controls are based. Thus, pressure spikes and noise spikes drive the fluctuations in the range signals seen in Figures 4.6 and 4.7 (Panel E).

Though the lab jack platform provides a level of nonlinearity and non-stationarity within our system, the compressibility of the platform arms does tend to reduce pressure wave reflections within the system. These reflections are evident as pressure spikes in the P_M waveforms shown in Figure 4.8. For those simulations where the lab jack platform had minimal contact with the end cap, the pressure wave reflections were higher. The compression of the lab jack arms and springs likely alters the timing of these reflections for simulations with lower compliance. An additional factor contributing to the pressure spikes within the system is the non-compliant pump used as input. This pump, as opposed to a heart

pump, has no give and tends to produce significant ringing of the underdamped pressure wave. In order to reduce the underdamped pressure reflections, a one-way fluid valve was inserted between the pump and the pump inflow attachment. This valve eliminated much of the ringing of the pressure wave. We anticipate that a compliant heart sack with a one-way valve will reduce these pressure wave reflections to acceptable levels.

The respiratory pump input also plays a role in the resistance and compliance values that must be realized by the system in order to produce a P_M that matches P_R. The characteristics of this pump are certainly not the same as those of a typical heart, where myocardial compliance and contractility will have a direct effect on pressure output. These factors play a role in what range of resistance and compliance are necessary within a physical system, and a lack of these factors affects the range of afterload parameter values realizable by our system. Nevertheless, even with the current pump setup, our system was able to operate acceptably at the upper end of a typical range of resistance values, while covering a somewhat wider range of compliance values. Bringing a live heart pump online with our dynamic afterload should only serve to improve the workability of the setup.

A major limitation on our system's performance is the lack of a real-time controller. Improved control over timing of the lab jack platform and the balloon inflation would reduce nonlinearities and non-stationarities for P_M. The current LabVIEW^{TM} code provides an acceptable level of control; however, there are issues with the timing of events. For example, the timing of the balloon inflation must be tied to the timing of other events in order to reduce overhead for the operation of the code and preserve the ability to reliably capture the necessary triggers. This restricts the level of accuracy in timing, and, though the timing

alterations may be only slight, they contribute to the lack of coherence seen at medium and high frequencies for our results.

It should be noted that, in using reference waveforms indicative or normal or pathophysiological states we are not attempting to model these states. There would be major and untested assumptions in asserting that we are creating a certain normal or pathophysiological condition for the heart by forcing a match in waveform parameters. In short, our goal is to match hemodynamic characteristics of reference pressure waveforms from a variety of physiological states.

Contributions of the Dynamic Afterload System

Our approach involving a fluid-mechanical dynamic afterload in order to drive a measured waveform to match reference waveform characteristics may appear unorthodox. However, there are several advantages to this system design. First, the system is loosely designed to enable afterload parameters to fluctuate as necessary in order to achieve the reference mean and range values. Thus, instead of trying to adjust to provide an impedance match for a particular P_R, our system automatically adapts the afterload as P_R changes. This approach would not be of use in studies where precise values of impedance parameters and details of the pressure waveforms are of interest, but this approach would be of use in studies where the mean and range of P_M and/or a mean flow must be maintained. For example, over time the isolated heart will weaken and reduce its output against a constant load. Our system could automatically adjust the impedance parameters to maintain a steady P_M generated from a changing source.

Another advantage of a dynamic afterload is the ability to study transients of source behavior as the afterload changes. As mentioned previously, many published studies have considered working heart behavior with a steady-state afterload. Our system would provide a convenient way to correlate changes in myocardial function with afterload changes.

One final advantage of our dynamic system is the fact that compliance is adjusted automatically to compensate for pressure range differences. To our knowledge, no one has attempted to automatically adjust compliance and resistance in a feedback loop for a working heart afterload. We believe that this option enables additional and more convenient studies in areas mentioned previously. The ability of our system to adjust compliance is limited at present, but with future iterations of the device, a more precise control would be maintained.

Considerations for Use with an Isolated Heart Apparatus

As stated in the *Introduction*, our goal is to incorporate this system with an isolated heart apparatus. With an isolated heart in place, we believe that many of the limitations of our system will be reduced or eliminated. A number of modifications must be made; however, before our dynamic afterload system is ready for implementation with an isolated heart. In an isolated working heart system, direct feedback from the afterload flow measurements to the pump supplying preload to the left atrium will be necessary. The ability to maintain the proper flow will be vital to prevent rupturing the system or creating a pressure vacuum within the system. Currently, the control code provides a measure of mean flow that is converted to a scaled voltage for driving a pulsatile preload pump. With a live heart in the fluid path, the system will need to be as free as possible from air bubbles that might affect circulation or alter compliance values. We have implemented a suction device to remove

trapped air from the top of the compliant end cap. The device is manually operated at present, but alterations could be made to provide a constant removal of trapped air.

Within the control code, the pacing trigger that begins each cycle will need to be modified to allow for a delay between electrical pacing of the atrium and the actual contraction of the ventricle. In addition, a real-time control system would be vital in order to ensure that a system crash would not produce an unstable environment during a study. Currently, our system is adaptable to a range of heart rates. However, the upper end of the pacing range (> 100 bpm) would likely provide some difficulties for certain adjustments. Again, a real-time control system would alleviate much of this concern.

In our discussion thus far, we have given little consideration to the right side of the heart. For an isolated working heart, installing a compliant balloon or other similar object into the right ventricle to account for right heart effects on left ventricular contraction may be necessary. Another possibility is to expand the system and maintain two dynamic afterloads, one for the left side of the heart and one for the right side. Each system could be maintained and controlled separately to provide a match for pulmonary and systemic P_R waveforms.

Conclusion

The dynamically adjustable afterload that we have designed performs acceptably in matching the reference waveform characteristics of mean and range for a pulsatile pressure input. This is true even for the basic non-compliant pump setup under which it was tested. The system response time for a step increase in mean pressure is also reasonable. While the four-element windkessel is not a perfect model to describe our afterload, this model captures the major traits of the system's behavior. Our dynamic afterload is suitable for future

implementation with an isolated heart apparatus and will provide the ability to expand the convenience and scope of studies involving the isolated porcine heart.

CHAPTER V

CONCLUSION

Summary of Important Findings

This work shows that the fluid-mechanical dynamically adjustable afterload provides an

automatic method for controlling the mean and range of pulsatile pressure input waves within

a reasonable physiologic range. The controls of the afterload were based on aortic pressure

(AOP) impedance interactions as revealed in the published model (SAVIAv1). [45]

Simulations with SAVIAv1 and analysis with PAASv1 (see Chapter 3) verify that the

impedance for the afterload is suitably modeled by a standard 4-Element windkessel-type

afterload. These results demonstrate that the dynamic afterload, with necessary

modifications, is appropriate for implementation with an isolated heart apparatus.

Controlled adjustments of the dynamic afterload (based on SAVIAv1) enact changes in the

pulsatile pressure input, driving this input to match reference pressure characteristics. For

reference pressures within a realizable physiological range, the system settled to $\pm 5\%$ of the

desired values for mean and range within at most 60 cycles (typical settling times were 45 –

50 cycles or less). Estimates of the system impedance (using PAASv1) and subsequent

simulations with SAVIAv1 demonstrate afterload parameters that fall into a physiological

range of values. These estimates have little variation for most simulations and the main

features of the system's impedance plots conform to the 4-Element windkessel-type afterload

model. Modeled AOP waveforms from SAVIAv1, based on measured flow and impedance

estimates, overlay well with measured pressures. In addition, trends for the measured pressure and flow exhibit expected behaviors with changes in impedance parameters. These results and the physical dimensions and adaptations that enable the dynamic afterload to interface with the Langendorff setup, ensure that the system is suitable for implementation with an isolated heart apparatus. Such an isolated, working heart with a dynamic afterload, would provide a method for studies requiring specific AOP characteristics and a method for studies where myocardial transients with afterload adjustment are of interest.

Future Improvements to the Work

The dynamic afterload possesses the desired functionality with regard to manipulation of the mean and range of the pulsatile input pressure. There are, however, several aspects of the mechanical load and the control system that warrant further work.

Improvement of the characteristic impedance of the system could be accomplished by placing a variable resistance element inline with the pump inflow attachment. A proportional valve would likely not be the best candidate, due to the change of path that the fluid would encounter and the effects this would have on wave reflection timing. A design with numerous parallel tubes and a sliding restrictor, as demonstrated by Westerfof *et al*. [11, 51] is a possible solution. Additionally, the sliding restrictor could be reformed as a constricting aperture (similar to apertures within cameras). A flexible pump inflow attachment would also contribute to more acceptable characteristic impedance. Flexible tubing would provide a much closer approximation to the aorta than the current setup, and would reduce the unwanted higher inertance that is currently present.

The system's stiffness, resulting in underdamped reflected pressure waves, is an issue that must be addressed. When a compliant heart sac is in place (see Chapter 4 Discussion), this should reduce the unwanted reflected pressure spikes; however, this may not totally eliminate the problem. It may be necessary to maintain the volume of the balloon at a level that would provide increased cushion for the pressure waves. The balloon could be adjusted in a slightly different manner than the on/off method currently used by inflation and holding of the volume with only slight air input or extraction within each cycle.

The main improvement necessary in the control code is to implement the controls in a real time system. The increased time resolution would enable advantages in adjustments of the afterload components and enhanced decision-making capabilities. Furthermore, the real time system would eliminate many of the timing issues (see Chapter 4 Discussion) currently present that produce non-stationarity of the system.

With these improvements and the necessary modifications for an isolated heart apparatus (see Chapter 4 Discussion) the fluid-mechanical dynamic afterload would be well-suited to act as a variable impedance control for AOP within an isolated working heart apparatus.

APPENDIX

Afterload Dimensions

Table A provides afterload dimensions for the upper and lower chambers and attachments.

Table A: Afterload Dimensions

Main Chamber UC = Upper Chamber LC = Lower Chamber	
UC length	6.05 cm
UC length unthreaded	1.30 cm
UC length threaded	4.75 cm
UC ID unthreaded	5.38 cm
LC length	9.70 cm
LC length untapered	2.90 cm
LC length tapered	6.80 cm
LC ID untapered	2.52 cm
LC ID tapered	4.30 cm
LC OD unthreaded	5.71 cm
LC angle of taper	7.5°
Pump Inflow Attachment (PIA) **Inline Flow Sensor (IFS)** **Characteristic Impedance (Zo segment)**	
PIA length (without inline flow sensor)	3.81 cm
PIA ID	1.25 cm
IFS length	3.40 cm
IFS ID	1.27 cm
Zo segment length	1.00 cm
Zo segment ID	0.43 cm
Fluid Outflow Attachment (FOA) and Proportional Valve (PV) **Parallel Line from FOA to Reservoir (PL)**	
FOA length	14.00 cm
FOA ID	1.10 cm
PV input	3/8" NPT
PV output	1/2" NPT
PL connector length	2.80 cm
PL connector ID	0.21 cm
PL tube length	50.00 cm
PL tube ID	0.51 cm
Air Inflow/Outflow Attachment (AA) and Balloon	
AA ID	0.33 cm
Balloon volume (unstretched)	3.00 ml

ID = Inner Diameter   OD = Outer Diameter

145

Calibration of Proportional Valve Resistance and End Cap Compliance

An inline proportional valve (dimensions and valve details provided in *Methods* and previously in the *Appendix*) is the main source of resistance within the system. This valve is controlled by a dc voltage input in the 2.5 – 9.5 V range, where < 2.5 V is closed and 9.5 V is completely open. A Millar pressure transducer (see *Methods*) was inserted near the inflow of the proportional valve. A parallel, constant flow line between the fluid outflow attachment and the reservoir was necessary in order to achieve the desired range of resistance values. A pressure head was produced by elevating a water reservoir. As the water flowed through the valve, the water level (and subsequently the pressure) was maintained by constant refilling of the reservoir. A volume flow was measured by collecting the valve outflow for a certain period of time. The ratio of this pressure to flow provided the resistance in units of mmHg s ml^{-1}. The goal was to relate resistance to the pressure and the voltage input of the proportional valve. Thus, several measurements were taken at varying pressures for each voltage level. Our results are shown in Figure A (left). These resistance values were obtained for a parallel flow tube of approximately 0.5 m length. Major adjustments in the resistance range can be made by altering the length of the parallel flow tube to the reservoir. A polynomial fit was made to the data for these pressures, and these formulas were used to calculate a weighted average of resistance as described in *Methods*.

The calibration of the latex end cap compliance was carried out as follows. A 0.025 inch thick latex sheet was draped over the end of the main chamber and secured with o-rings and an adjustable tie. The air inflow/outflow attachment was sealed, and the fluid outflow attachment was connected to a closed proportional valve. A Millar pressure transducer (see *Methods*) was inserted into the fluid outflow attachment, and the pump inflow attachment

146

was inserted into the lower chamber. A rubber stopper with tube insert was used to seal the

pump inflow attachment, and this tube was used to introduce water to the chamber. The

chamber was inverted to enable measurement of the fluid level in the inserted tube. As fluid

was introduced to the chamber, the latex sheet bulged out, and the fluid level in the tube rose

from its starting level. When the desired pressure was reached, the addition of water to the

system was stopped. The added fluid was then drained to the starting level by opening the

proportional valve and collecting the outflow. A measure of the initial and final pressures

and the volume added provided the compliance of the latex sheet by use of equation A.

$$C\left(ml\ mmHg^{-1}\right) = \frac{V_{added}\left(ml\right)}{P_{final} - P_{init}\left(mmHg\right)} \qquad\qquad \text{A}$$

The end cap was placed directly over the lab jack platform. The measurement of

compliance was performed for a minimum of three different pressures for each height of the

lab jack platform. The height of the lab jack platform was set at varying distances from the

top of the chamber, and this enabled the sheet to extend only a certain amount (the closer the

platform, the less extension). Distances of 3, 6, 10 and > 20mm from the top of the chamber

were used to determine how the latex sheet's compliance would vary with platform height.

Results from the calibrations are shown in Figure A (right).

Calibration of Afterload Elements
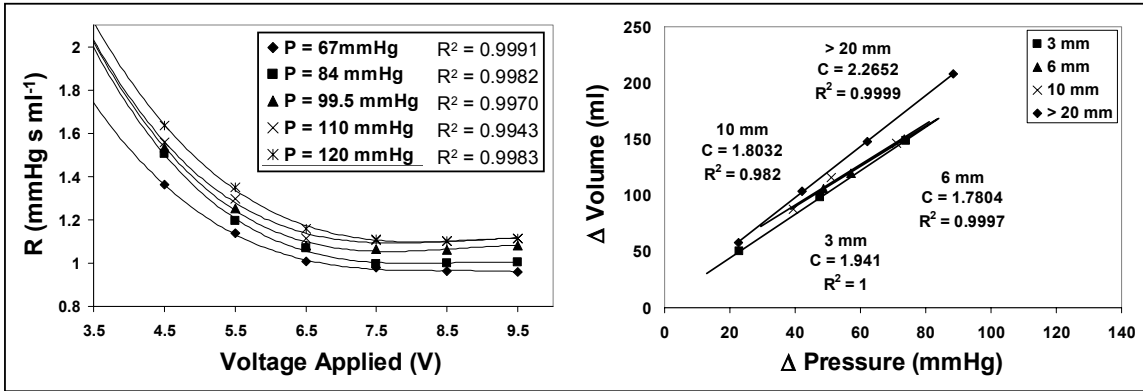
Figure A Resistance and Compliance Calibration Plots. Resistance as a function of voltage applied to the proportional valve (left) is plotted for different pressures. R^2 values are supplied for the third order polynomial fit. Change in volume vs. the change in pressure is plotted for different heights of the lab jack (right), and the slope of the best-fit line is the compliance value.

REFERENCES

1.   Palladino, J. L. and A. Noordergraaf. The changing view of the heart through the centuries. *Studies in Health Technology & Informatics* 71:3-11, 2000.

2.   Timmons, W. D. Cardiovascular Models and Control. In: J. D. Bronzino, ed. *The Biomedical Engineering Handbook.* Boca Raton, FL: CRC Press, Inc. and IEEE Press; 1995:2386-2403.

3.   Nichols, W. W., M. F. O'Rourke and C. Hartley. *McDonald's blood flow in arteries: theoretical, experimental and clinical principles*. 4th ed. London: Arnold; 1998.

4.   Taegtmeyer, H. One hundred years ago: Oscar Langendorff and the birth of cardiac metabolism. *Can. J. Cardiol.* 11(11):1030-1035, 1995.

5.   Zimmer, H.-G. The isolated perfused heart and its pioneers. *News Physiol. Sci.* 13:203-210, 1998.

6.   Langendorff, O. Untersuchungen am uberlebenden Saugethierherzen. *Pflugers Arch.* 61(6):291-332, 1895.

7.   Schreiber, S. S., M. Oratz and M. A. Rothschild. Effect of ouabain on potassium exchange in the mammalian heart. *Am. J. Physiol.* 200(5):1055-1062, 1961.

8.   Neely, J. R., H. Liebermeister, E. J. Battersby and H. E. Morgan. Effect of pressure development on oxygen consumption by isolated rat heart. *Am. J. Physiol.* 212(4):804-814, 1967.

9.   Noordergraaf, A. *Circulatory System Dynamics*. New York: Academic Press, Inc.; 1978.

10. Rideout, V. C. and D. E. Dick. Difference-differential equations for fluid flow in distensible tubes. *IEEE Transactions on Biomedical Engineering* BME-14(3):171-77, 1967.

11. Westerhof, N., G. Elzinga and S. Pieter. An artificial system for pumping hearts. *J. Appl. Physiol.* 31(5):776-781, 1971.

12. Sagawa, K. The ventricular pressure-volume diagram revisited. *Circ. Res.* 43(5):677-687, 1978.

13. Sagawa, K., L. Maughan, H. Suga and K. Sunagawa. *Cardiac Contraction and the Pressure-Volume Relationship*. New York: Oxford University Press Inc.; 1988.

14. Suga, H. and K. Sagawa. Instantaneous pressure-volume relationships and their ratio in the excised, supported canine left ventricle. *Circ. Res.* 35(1):117-126, 1974.

15. Sunagawa, K., W. L. Maughan, G. Friesinger, P. Guzman, M.-S. Chang and K. Sagawa. Effects of coronary arterial pressure on left ventricular end-systolic pressure-volume relation of isolated canine heart. *Circ. Res.* 50(5):727-734, 1982.

16. Westerhof, N., P. Sipkema, G. Elzinga, J. P. Murgo and J. P. Giolma. Arterial Impedance. In: N. H. C. Hwang, D. R. Gross and D. J. Patel, ed(s). *Quantitative cardiovascular studies: clinical and research applications of engineering principles.* Baltimore: University Park Press; 1979:111-150.

17. Rideout, V. C. *Mathematical and Computer Modeling of Physiological Systems.* Madison, WI: Medical Physics Publishing; 1991.

18. Lucas, C. L. Fluid Mechanics of the Pulmonary Circulation. *CRC Critical Reviews in Biomedical Engineering* 10(4):317-392, 1984.

19. Ursino, M., M. Antonucci and E. Belardinelli. Role of active changes in venous capacity by the carotid baroreflex: analysis with a mathematical model. *Am. J. Physiol.* 267(*Heart Circ. Physiol.* 36):H2531-H2546, 1994.

20. Ursino, M. Interaction between carotid baroregulation and the pulsating heart: a mathematical model. *Am. J. Physiol.* 275(*Heart Circ. Physiol.* 44):H1733-H1747, 1998.

21. Olansen, J. B., J. W. Clark, D. Khoury, F. Ghorbel and A. Bidani. A closed-loop model of the canine cardiovascular system that includes ventricular interaction. *Comput. Biomed. Res.* 33:260-295, 2000.

22. Chung, D. C., S. C. Niranjan, J. W. Clark, Jr., A. Bidani, W. E. Johnston, J. B. Zwischenberger and D. L. Traber. A dynamic model of ventricular interaction and pericardial influence. *Am. J. Physiol.* 272(*Heart Circ. Physiol.* 41):H2942-H2962, 1997.

23. Davis, M. J. and R. W. Gore. Determinants of cardiac function: simulation of a dynamic cardiac pump for physiology instruction. *Adv Physiol Educ* 25(1):13-35, 2001.

24. Holdsworth, D. W., D. W. Rickey, M. Drangova, D. J. M. Miller and A. Fenster. Computer-controlled positive displacement pump for physiological flow simulation. *Med. Biol. Eng. Comput.* 29:565-570, 1991.

25. Pantalos, G. M., J. Hayes, P. Khanwilkar, G. Bearnson and D. Olsen. Left ventricular simulator for cardiovascular device testing. *ASAIO J.* 42(2):46, 1996.

26. Pantalos, G. M., S. C. Koenig, K. J. Gillars, G. A. Giridharan and D. L. Ewert. Characterization of an adult mock circulation for testing cardiac support devices. *ASAIO J.* 50:37-46, 2004.

27. Wu, Z. J., B. Z. Gao and N. H. C. Hwang. Transient pressure at closing of a monoleaflet mechanical heart valve prosthesis: Mounting compliance effect. *J. Heart Valve Dis.* 4(5):553-567, 1995.

28. Woodard, J. C., S. M. Rock and P. M. Portner. A sophisticated electromechanical ventricular simulator for ventricular assist system testing. *ASAIO Trans.* 37:M210-M211, 1991.

29. Lieber, B. B., V. Livescu, L. N. Hopkins and A. K. Wakhloo. Particle image velocimetry assessment of stent design influence on intra-aneurysmal flow. *Ann. Biomed. Eng.* 30:768-777, 2002.

30. Liu, Y., P. Allaire, H. Wood and D. Olsen. Design and initial testing of a mock human circulatory loop for left ventricular assist device performance testing. *Artif. Organs* 29(4):341, 2005.

31. Gao, B. Z., N. Hosein and N. H. C. Hwang. Hydrodynamics of a long-body bileaflet mechanical heart valve. *ASAIO J.* 43:M396-M401, 1997.

32. Gao, B. Z., S. Pandya, C. Arana and N. H. C. Hwang. Bioprosthetic heart valve leaflet deformation monitored by double-pulse stero photogrammetry. *Ann. Biomed. Eng.* 30:11-18, 2002.

33. Chinchoy, E., L. C. Soule, A. J. Houlton, W. J. Gallagher, M. A. Hjelle, T. G. Laske, J. Morissette and P. A. Iaizzo. Isolated four-chamber working swine heart model. *Ann. Thorac. Surg.* 70:1607-1614, 2000.

34. Fisher, A., R. E. Challis and P. Swann. A controllable artificial afterload for isolated heart studies. *J. Biomed. Eng.* 6:305-310, 1984.

35. Elzinga, G. and N. Westerhof. Pressure and flow generated by the left ventricle against different impedances. *Circ. Res.* 32(2):178-186, 1973.

36. Milnor, W. R. Arterial impedance as ventricular afterload. *Circ. Res.* 36(5):565-570, 1975.

37. Sunagawa, K., K. Sagawa and W. L. Maughan. Ventricular interaction with the loading system. *Ann. Biomed. Eng.* 12(2):163-189, 1984.

38. Maughan, W. L., K. Sunagawa, D. Burkhoff and K. Sagawa. Effect of arterial impedance changes on end-systolic pressure-volume relation. *Circ. Res.* 54(5):595-602, 1984.

39. Maughan, W. L., K. Sunagawa, D. Burkhoff, W. L. J. Graves, W. C. Hunter and K. Sagawa. Effect of heart rate on the canine end-systolic pressure-volume relationship. *Circulation* 72(3):654-659, 1985.

40. Murgo, J. P., N. Westerhof, J. P. Giolma and S. A. Altobelli. Aortic input impedance in normal man: Relationship to pressure wave forms. *Circulation* 62(1):105-116, 1980.

41. Nichols, W. W., C. R. Conti, W. E. Walker and W. R. Milnor. Input impedance of the systemic circulation in man. *Circ. Res.* 40(5):451-458, 1977.

42. Laskey, W. K. and W. G. Kussmaul. Arterial wave reflection in heart failure. *Circulation* 75(4):711-722, 1987.

43. O'Rourke, M. F. *Arterial function in health and disease*. Edinburgh, NY: Churchill Livingstone; 1982.

44. Murgo, J. P., N. Westerhof, J. P. Giolma and S. A. Altobelli. Effects of exercise on aortic input impedance and pressure wave forms in normal humans. *Circ. Res.* 48(3):334-343, 1981.

45. Cole, R. T., C. L. Lucas, W. E. Cascio and T. A. Johnson. A LabVIEW(TM) model incorporating an open-loop arterial impedance and a closed-loop circulatory system. *Ann. Biomed. Eng.* 33(11):1555-1573, 2005.

46. Chen, C.-W., Y.-W. R. Shau and C.-P. Wu. Analog transmission line model for simulation of systemic circulation. *IEEE Transactions on Biomedical Engineering* 44(1):90-94, 1997.

47. Liu, Z., F. Shen and F. C. P. Yin. Impedance of arterial system simulated by viscoelastic t tubes terminated in windkessels. *Am. J. Physiol.* 256(4 Pt 2):H1087-H1099, 1989.

48. Palladino, J. L., G. M. Drzewiecki and A. Noordergraaf. Modeling Strategies in Physiology. In: J. D. Bronzino, ed. *The Biomedical Engineering Handbook*. Boca Raton, FL: CRC Press, Inc. and IEEE Press; 1995:2367-2374.

49. Noble, M. I. Left ventricular load, arterial impedance and their interrelationship. *Cardiovasc. Res.* 13(4):183-198, 1979.

50. Zamir, M. *The Physics of Pulsatile Flow*. New York: Springer-Verlag; 2000.

51. Westerhof, N. Arterial Haemodynamics. In: J. Strackee and N. Westerhof, ed(s). *The Physics of heart and circulation*. Philadelphia: Institute of Physics Pub.; 1993:355-381.

52. Danielsen, M., J. L. Palladino and A. Noordergraaf. The left ventricular ejection effect. In: J. T. Ottesen and M. Danielsen, ed(s). *Mathematical Modeling in Medicine*. Netherlands: IOS Press; 2000:13-28.

53. Danielsen, M. and J. T. Ottesen. Describing the pumping heart as a pressure source. *J. Theor. Biol.* 212:71-81, 2001.

54. Guyton, A. C. and J. E. Hall. *Textbook of Medical Physiology*. 10th ed. Philadelphia: W.B. Saunders Company; 2000.

55. Ferrari, G., M. Kozarski, C. De Lazzari, F. Clemente, M. Merolli, G. Tosti, M. Guaragno, R. Mimmo, D. Ambrosi and J. Glapinski. A hybrid (numerical-physical) model of the left ventricle. *Int. J. Artif. Organs* 24(7):456-462, 2001.

56. Palladino, J. L., L. C. Ribeiro and A. Noordergraaf. Human circulatory system model based on Frank's mechanism. In: J. T. Ottesen and M. Danielsen, ed(s). *Mathematical Modeling in Medicine.* Netherlands: IOS Press; 2000:29-40.

57. Palladino, J. L., J. P. Mulier and A. Noordergraaf. Closed-loop circulation model based on the Frank mechanism. *Surveys on Mathematics for Industry* 7:177-186, 1997.

58. Ottesen, J. T. and M. Danielsen. Modeling ventricular contraction with heart rate changes. *J. Theor. Biol.* 222:337-346, 2003.

59. Mulier, J. P. *Ventricular pressure as a function of volume and flow* [Ph.D. Dissertation]. University of Leuven, Belgium; 1994.

60. Stergiopulos, N., B. E. Westerhof and N. Westerhof. Total arterial inertance as the fourth element of the windkessel model. *Am. J. Physiol.* 276(1 Pt 2):H81-8, 1999.

61. Dankelman, J., H. G. Stassen and J. A. E. Spaan. Coronary Circulation Mechanics. In: F. Kajiya, G. A. Klassen, J. A. E. Spaan and J. I. E. Hoffman, ed(s). *Coronary Circulation: Basic Mechanism and Clinical Relevance.* New York: Springer-Verlag; 1990:75-87.

62. Tsujioka, K., M. Goto, O. Hiramatsu, Y. Wada, Y. Ogasawara and F. Kajiya. Functional Characteristics of Intramyocardial Capacitance Vessels and Their Effects on Coronary Arterial Inflow and Venous Outflow. In: F. Kajiya, G. A. Klassen, J. A. E. Spaan and J. I. E. Hoffman, ed(s). *Coronary Circulation: Basic Mechanisms and Clinical Relevance.* New York: Springer-Verlag; 1990:89-97.

63. Mantero, S., R. Pietrabissa and R. Fumero. The coronary bed and its role in the cardiovascular system: a review and an introductory single-branch model. *J. Biomed. Eng.* 14:109-116, 1992.

64. Pietrabissa, R., S. Mantero, T. Marotta and L. Menicanti. A lumped parameter model to evaluate the fluid dynamics of different coronary bypasses. *Med. Eng. Phys.* 18:477-484, 1996.

65. Hoffman, J. I. E. Pressure-Flow Relationships of the Coronary Arteries. In: F. Kajiya, G. A. Klassen, J. A. E. Spaan and J. I. E. Hoffman, ed(s). *Coronary Circulation: Basic Mechanisms and Clinical Relevance.* New York: Springer-Verlag; 1990:109-125.

66. Nishioka, O., Y. Maruyama, K. Ashikawa, S. Isoyama, S. Satoh, J. Watanabe, Y. Shimizu and T. Takishima. Load dependency of end-systolic pressure-volume relations in isolated, ejecting canine hearts. *Jpn. Heart J.* 29(5):709-722, 1988.

67. Paulus, W. J., V. A. Claes and D. L. Brutsaert. End-systolic pressure-volume relation estimated from physiologically loaded cat papillary muscle contractions. *Circ. Res.* 47(1):20-26, 1980.

68. Westerhof, N. and G. Elzinga. Normalized input impedance and arterial decay time over heart period are independent of animal size. *Am. J. Physiol.* 261(1 pt.2):R126-R133, 1991.

69. Finkelstein, S. M., J. N. Cohn, V. R. Collins, P. F. Carlyle and W. J. Shelley. Vascular hemodynamic impedance in congestive heart failure. *Am. J. Cardiol.* 55:423-427, 1985.

70. Pepine, C. J., W. W. Nichols and C. R. Conti. Aortic input impedance in heart failure. *Circulation* 58(3):460-465, 1978.

71. Watt, T. B. and C. S. Burrus. Arterial pressure contour analysis for estimating human vascular properties. *J. Appl. Physiol.* 40(2):171-176, 1976.

72. Arnold, J. M. O., G. E. Marchiori, J. R. Imrie, G. L. Burton, P. W. Pflugfelder and W. J. Kostuk. Large artery function in patients with chronic heart failure. *Circulation* 84:2418-2425, 1991.

73. Kleinbaum, D. G. and L. L. Kupper. *Applied Regression Analysis and Other Multivariable Methods.* North Scituate, Mass.: Duxbury Press, division of Wadsworth Publ. Comp. Inc.; 1978.

74. Watanabe, I., T. A. Johnson, C. L. Engle, C. Graebner, M. G. Jenkins and L. S. Gettes. Effects of Verapamil and Propranolol on changes in extracellular K^+, pH, and local activation during graded coronary flow in the pig. *Circulation* 79(4):939-947, 1989.

75. Maughan, W. L. and K. Sunagawa. Factors affecting the end-systolic pressure-volume relationship. *Federation Proceedings* 43(9):2408-2410, 1984.

76. Alexander, J., K. Sunagawa, N. Chang and K. Sagawa. Instantaneous pressure-volume relation of the ejecting canine left atrium. *Circ. Res.* 61(2):209-219, 1987.

77. Rose, W. C. and A. A. Shoukas. Two-port analysis of systemic venous and arterial impedances. *Am. J. Physiol.* 265(*Heart Circ. Physiol.* 34):H1577-H1587, 1993.

78. Palladino, J. L., J. P. Mulier, F. Wu, M. Moser, T. Kenner, R. M. Baevsky and A. Noordergraaf. Assessing the state of the circulatory system via parameters vs. variables. *Journal of Cardiovascular Diagnosis and Procedures* 13(2):131-139, 1996.

79. Grossman, W., E. Braunwald and T. Mann. Contractile state of the left ventricle in man as evaluated from end-systolic pressure-volume relations. *Circulation* 56(5):845-852, 1977.

80. Sagawa, K. The end-systolic pressure-volume relation of the ventricle: definition, modifications and clinical use. *Circulation* 63(6):1223-1227, 1981.

81. Maruyama, Y. and T. Takishima. Effect of Ventricular and Extraventricular Pressure on the Coronary Artery Pressure-Flow Relationship. In: F. Kajiya, G. A. Klassen, J. A. E. Spaan and J. I. E. Hoffman, ed(s). *Coronary Circulation: Basic Mechanisms and Clinical Relevance.* New York: Springer-Verlag; 1990:127-138.

82. Ottesen, J. T., M. S. Olufsen and J. K. Larsen. *Applied Mathematical Models in Human Physiology*. Philadelphia: SIAM; 2004.

83. Tsitlik, J. E., H. R. Halperin, A. S. Popel, A. A. Shoukas, F. C. P. Yin and N. Westerhof. Modeling the circulation with three-terminal electrical networks containing special non-linear capacitors. *Ann. Biomed. Eng.* 20:595-616, 1992.

84. Danielsen, M. *Modeling of Feedback Mechanisms which Control the Heart Function in a View to an Implementation in Cardiovascular Models (2nd ed.)* [Ph.D.]. Roskilde: Mathematics, Roskilde University; 1998.

85. Ottesen, J. T. Modelling of the baroreflex-feedback mechanism with time-delay. *J. Math. Biol.* 36:41-63, 1997.

86. Ottesen, J. T. Nonlinearity of baroreceptor nerves. *Surveys on Mathematics for Industry* 7:187-201, 1997.

87. Ottesen, J. T. Modelling the dynamical baroreflex-feedback control. *Math. Comp. Model.* 31:167-173, 2000.

88. Lu, K., J. W. Clark, Jr., F. H. Ghorbel, C. S. Robertson, D. L. Ware, J. B. Zwischenberger and A. Bidani. Cerebral autoregulation and gas exchange studied using a human cardiopulmonary model. *Am. J. Physiol.* 286(*Heart Circ. Physiol.*):H584-H601, 2003.

89. Goerke, J. Jon Goerke's Arterial Simulation. *http://hemodynamics.ucdavis.edu/* [webpage]. 2003. Accessed, 2003.

90.   Burkhoff, D., D. Kass, W. L. Maughan and A. Kolandaivelu. CVSIM v1.5.
        http://oac.med.jhmi.edu/cvsim/ [webpage]. Accessed, 2004.

91.   Barton, C. W., W. E. Cascio, N. D. Batson, C. L. Engle and T. A. Johnson. The
        effects of rates of perfusion on dominant frequency and defibrillation energy in the
        isolated heart. *Pacing Clin. Electrophysiol.* 23(1):504-511, 2000.

92.   Bendat, J. S. and A. G. Piersol. *Random Data: Analysis and Measurement
        Procedures*. 2nd ed. New York: John Wiley & Sons; 1986.

93.   Bendat, J. S. and A. G. Piersol. *Engineering Applications of Correlation and Spectral
        Analysis*. 2nd ed. New York: John Wiley & Sons, Inc.; 1993.

94.   Proakis, J. G. and D. G. Manolakis. *Digital Signal Processing Principles, Algorithms,
        and Applications*. 2nd ed. New York: Macmillan Publishing Company; 1992.

95.   Maki, B. E. Interpretation of the Coherence Function When Using Pseudorandom
        Inputs to Identify Nonlinear Systems. *IEEE Trans. Biomed. Eng.* BME-33(8):775-
        779, 1986.

96.   Davis, J. C. *Statistics and data analysis in geology*. 3rd ed. New York: Wiley; 2002.

97.   PCQNG (TM). *ComScire* [Software Package]. Available at:
        http://comscire.com/Home/. Accessed, 2006.

98.   random.org (True Random Number Service). *Trinity College* [Data Files]. Available
        at: http://www.random.org/. Accessed, 2006.

99.   Quint, S. R. and R. N. Johnson. Directional facilitation of evoked response activity in
        the ventrolateral thalamus of the cat. *Brain Res.* 144:159-163, 1978.

100.   Quint, S. R., J. F. Howard and L. Antoni. On-line analysis of neuromuscular
        bioelectric potentials. *Comput. Programs Biomed.* 16:3-12, 1983.

101.   Quint, S. R., R. S. Greenwood, J. F. Howard and J. V. Gomez. A generalized
        methodology for on-line analysis and off-line processing of neurally evoked
        potentials. *Comput. Programs Biomed.* 20:35-44, 1985.

102.   Quint, S. R., D. F. Michaels, G. W. Hilliard and J. A. Messenheimer. A real-time
        system for the spectral analysis of the EEG. *Comput. Methods Programs Biomed.*
        28:11-22, 1989.

103.   Marmarelis, V. *Analysis of Physiological Systems: The White-Noise Approach*. New
        York: Springer; 1978.

104. Suki, B. and K. R. Lutchen. Pseudorandom Signals to Estimate Apparent Transfer and Coherence Functions of Nonlinear Systems: Applications to Respiratory Mechanics. *IEEE Trans. Biomed. Eng.* 39(11):1142-1151, 1992.

105. Victor, J. and R. Shapley. A method of nonlinear analysis in the frequency domain. *Biophys. J.* 29:459-484, 1980.

106. Cerutti, S., M. Alberti, G. Baselli, O. Rimoldi, A. Malliani, M. Merri and M. Pagani. Automatic assessment of the interaction between respiration and heart rate variability signal. *Med. Prog. Technol.* 14(1):7-19, 1988.

107. Milestones in Cardiology. *MedNets*. Available at: http://www.mednets.com/index.cfm/fuseaction/articles_milestone_cardiology_milestonescardiology. Accessed, 2006.

108. Kozarski, M., G. Ferrari, F. Clemente, K. Gorczynska, C. De Lazzari, M. Darowski, R. Mimmo, G. Tosti and M. Guaragno. A hybrid mock circulatory system: Development and testing of an electro-hydraulic impedance simulator. *Int. J. Artif. Organs* 26(1):53-63, 2003.

109. Colacino, F. M., M. Arabia, G. A. Danieli, F. Moscato, S. Nicosia, F. Piedimonte, P. Valigi and S. Pagnottelli. Hybrid test bench for evaluation of any device related to mechanical cardiac assistance. *Int. J. Artif. Organs* 28(8):817-826, 2005.

110. Murgo, J. P., N. Westerhof, J. P. Giolma and S. A. Altobelli. Manipulation of ascending aortic pressure and flow wave reflections with the Valsalva maneuver: Relationship to input impedance. *Circulation* 63(1):122-132, 1981.

111. Fogliardi, R., M. Di Donfrancesco and R. Burattini. Comparison of linear and nonlinear formulations of the three-element windkessel model. *Am. J. Physiol.* 271(6 Pt 2):H2661-H2668, 1996.

112. Li, J. K.-J., T. Cui and G. M. Drzewiecki. A nonlinear model of the arterial system incorporating a pressure-dependent compliance. *IEEE Transactions on Biomedical Engineering* 37(7):673-678, 1990.

113. Li, J. K.-J. and Y. Zhu. Arterial compliance and its pressure dependence in hypertension and vasodilation. *Angiology* 45(2):113-117, 1994.

114. Stefanadis, C., C. Stratos, C. Vlachopoulos, S. Marakas, H. Boudoulas, I. Kallikazaros, E. Tsiamis, K. Toutouzas, L. Sioros and P. Toutouzas. Pressure-diameter relation of the human aorta. *Circulation* 92:2210-2219, 1995.

115. Toorop, G. P., N. Westerhof and G. Elzinga. Beat-to-beat estimation of peripheral resistance and arterial compliance during pressure transients. *Am. J. Physiol.* 252(Heart Circ. Physiol. 21):H1275-H1283, 1987.

116. Shim, Y., A. Pasipoularides, C. A. Straley, T. G. Hampton, P. F. Soto, C. H. Owen, J. W. Davis and D. D. Glower. Arterial windkessel parameter estimation: A new time-domain method. *Ann. Biomed. Eng.* 22:66-77, 1994.

117. Segers, P., S. Brimioulle, N. Stergiopulos, N. Westerhof, R. Naeije, M. Maggiorini and P. Verdonck. Pulmonary arterial compliance in dogs and pigs: the three-element windkessel model revisited. *Am. J. Physiol.* Heart Circ Physiol 277:725-731, 1999.

118. Oppenheim, A. V., A. S. Willsky and S. H. Nawab. *Signals & Systems*. 2nd ed. Upper Saddle River, New Jersey: Prentice Hall; 1997.

119. Callaghan, F. J., L. A. Geddes, C. F. Babbs and J. D. Bourland. Relationship between pulse-wave velocity and arterial elasticity. *Med. Biol. Eng. Comput.* 24:248-254, 1986.

120. Stergiopulos, N., S. Vulliemoz, A. Rachev, J.-J. Meister and S. E. Greenwald. Assessing the homogeneity of the elastic properties and composition of the pig aortic media. *J. Vasc. Res.* 38:237-246, 2001.